An All-In-One, Low-Cost Photogrammetry Rig for 3D Plant Modelling and Phenotyping

Joe Hrzich

A thesis/proposal submitted to the Faculty of Graduate Studies of

The University of Winnipeg

In partial fulfillment of the requirements of the degree of

MASTERS OF SCIENCE

Department of Applied Computer Science

The University of Winnipeg

Winnipeg, Manitoba, Canada

Abstract

Photogrammetry, the science of generating 3D models of objects from photographs, offers a comprehensive method for acquiring, studying, and analyzing detailed information about the structure of objects. Utilizing the cost-effective Structure from Motion (SfM) technique, it is possible to generate 3D models from numerous 2D images taken from various angles. Point clouds represent a standard format for 3D data generated by depth sensors such as LIDARs and RGB-D cameras. Despite their utility, high-quality 3D scanners, costing upwards of $70,000, remain relatively expensive for many researchers and practitioners within the agricultural sector. In response, we have developed a low-cost, close-range photogrammetry rig, priced at $2,600, to support agronomists, plant scientists, and breeders. This work outlines the development of our device, which integrates a multi-camera system featuring the Arducam 64MP Autofocus Quad-Camera Kit, a rotary table from Ortery, and a Raspberry Pi for comprehensive control and processing. Our scanner efficiently captures detailed plant 3D data, offering a valuable tool for non-destructive, automatic, and robust 3D phenotyping. It is possible to use our device across various applications, including growth monitoring and the extraction of plant traits. Specifically, we have leveraged the device to measure the canopy volume of different wheat genotypes by computing the convex hull from the 3D data. Furthermore, through our photogrammetry rig, we have developed a high-throughput, quantitative trait index for wheat to identify distinct planophile and erectophile canopy architectures.

Acknowledgments

First and foremost, my deepest appreciation goes to my co-supervisors, Dr. Christopher Bidinosti and Dr. Michael Beck, for their exceptional mentorship, support, expertise and guidance throughout my master's journey and thesis work. Their vast knowledge and insightful feedback were instrumental in both the successful completion of this work.

Besides my advisors, I am most grateful to Dr. Christopher Henry and Dr. Edward Cloutis for reading my thesis and providing valuable comments.

Special thanks are extended to Dr. Karen Tanino, and Kalhari Manawasinghe for their contributions and collaborative efforts.

My sincere gratitude also goes to Mitacs, EMILI, and The Faculty of Graduate Studies for their financial support, which was crucial in allowing me to fully commit to my research.

Lastly, I cannot thank my parents and friends enough for their unwavering support and love, which have been my constant source of strength and motivation.

Contents

List of Tables

List of Figures

1. Introduction

Climate change and population growth present imminent threats to food security. By 2050, the world population will reach 9 billion [1]. Alongside the increasing population, the demand for food is intensifying. To improve crop production and plant breeding effectively, the United Nations Food and Agriculture Organization (FAO) estimates that global crop production will need to increase by 60% to meet the demands of the world's population by 2050 [2]. Researchers must find more effective ways to assess crops and extract novel plant traits to address the urgent need for improved crop yields and enhanced food security. In recent decades, crop yields have significantly improved, mainly attributed to progress in breeding and genetics [3,4]. Accurate measurement and analysis of a plant's architecture is a critical and challenging task, but it is essential for developing new crop varieties. Using imaging tools and analysis with artificial intelligence (AI) and computer vision can potentially revolutionize food production in the agricultural industry [5]. These tools are essential to help create crop plants optimized for higher yields, excellent nutritional value, and greater resilience to environmental stressors.

However, traditional methods of plant analysis have limitations. These methods can be time-consuming, labor-intensive, and prone to errors, resulting in inaccurate data that may hinder plant research [6–8]. Furthermore, traditional methods can limit our ability to quantitatively understand genetic traits that govern plant development, particularly over the entire life cycle of the plant. Non-invasive and non-contact methods for plant analysis have become increasingly popular as these methods enable a more thorough and accurate analysis of plant growth and development without damaging the plant itself. Data can be collected throughout the lifetime of the plant, providing a more comprehensive understanding of its traits and response to environmental factors.

Phenotyping measures and analyzes the physical and physiological characteristics of plants,

including their growth, development, and response to environmental factors. Various parameters are measured, such as plant height, width, length, plant canopy volume, and projected leaf area [9]. Plant phenotyping is about understanding the relationship between the genes governing plant development and the physical and physiological traits these genes manifest in plants. Researchers can understand how different genetic variations interact with the environment to produce specific phenotype outcomes by measuring and analyzing a wide range of plant traits. This information can then be used to develop more effective plant breeding and genetics strategies and improve our understanding of plant physiology. Phenotyping builds this relationship between genotype and phenotype of plants by systematically measuring and analyzing physical and biochemical traits of plants, allowing researchers to understand better how genetic factors contribute to the observable characteristics of plants. The field of plant phenomics underpins this process and is an area of research that is rapidly gaining popularity in the plant sciences [10]. Measuring plant traits in a phenomic study is a critical step in the plant breeding process, as it provides a way to evaluate the performance of different plant varieties and identify the most promising candidates for further development.

Recent technological advances have paved the way for the integration of intelligent sensors, big data, machine learning, and non-invasive technologies, which enable real-time data analysis on an unprecedented scale [8, 11, 12]. Adopting these modern imaging techniques for plant breeding, cultivation, and management of crops will assist in sustainably improving plant production [13,14]. Automated solutions for data acquisition have led to the development of platforms that combine vehicles, robotics, imaging systems, and sensors to efficiently and accurately measure plants [15]. These platforms can cover large areas of field crops in a short amount of time, collecting vast amounts of data. One key ingredient towards developing more efficient breeding strategies for improving crop yields and quality is plant phenotyping [16, 17].

Incorporating imaging tools into phenotyping enhances the comprehensiveness and accuracy of plant trait assessments. Two-dimensional (2D) imaging techniques effectively measure the structural traits of plants, enabling quantitative measurements of various traits, including plant surface

area, leaf shape, leaf color, and leaf count [18, 19]. These techniques, encompassing visible light and infrared imaging, are valuable for their simplicity and efficiency. However, 2D imaging can lead to inaccuracies in complex or more extensive plants due to overlapping image features and lack of depth-information [20]. Three-dimensional (3D) imaging techniques have been increasingly employed to overcome these limitations. These techniques enable a more detailed capture of the structure of plants, avoiding issues like self-occlusion of plant tissues. Additionally, 3D imaging offers a more accurate measurement of plant traits by capturing information about plant structures that are challenging to quantify with 2D images [21]. For instance, 3D imaging can reveal the internal architecture of plants, such as leaf distribution within the canopy or the overall plant architecture, providing deeper insights into plant growth and development.

Several 3D imaging techniques are commonly used in plant phenotyping, including Light Detection and Ranging (LiDAR), stereoscopic imaging, Time of Flight Cameras (ToF), and 3D reconstruction from multiple 2D images such as photogrammetry. Understanding the strengths and weaknesses of each can help researchers choose the most appropriate method for their specific phenotyping needs. For example, LiDAR provides high-resolution and accurate 3D point clouds of plant structures but can be expensive and challenging to implement in field conditions [22]. Photogrammetry offers a cost-effective alternative offering a balance between cost and accuracy that leverages computational techniques to generate 3D models; however, it may be less accurate and more sensitive to environmental conditions, such as lighting variations [23].

Integrating various imaging techniques provides comprehensive and accurate assessments of plant traits, reducing the time and labor involved in manual measurements. Two-dimensional imaging techniques offer valuable insights into structural plant traits, while three-dimensional imaging techniques address the limitations of 2D imaging, such as occlusion issues, and provide more detailed information about plant structures. Photogrammetry balances cost and accuracy, making it an attractive option for researchers to study plant growth, development, and response to environmental factors. A typical schematic of a close-range photogrammetry rig is shown in Figure 1.1 and includes cameras, a rotary table for precise object positioning, a specialized lighting setup,

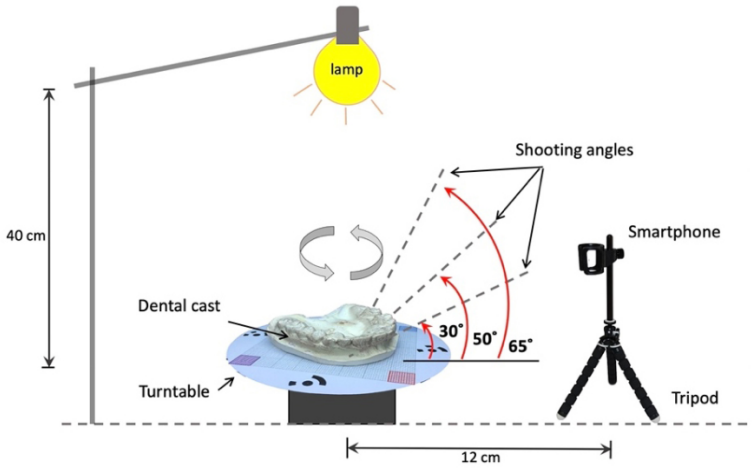

Figure 1.1: Schematic of a close-range photogrammetry rig showing key components such as cameras, a rotary table, and lighting. It demonstrates how the rig captures multiple 2D images from various directions and angles to develop a digital 3D model. In this example, researchers developed a digital 3D dental cast model with their photogrammetry system. (Image adapted from Ref. [24].)

and the option for a backdrop. A photogrammetry rig, comprised of low-cost hardware, can offer high-precision data of plant architectures, which is essential for conducting detailed morphological studies. As our understanding of these imaging techniques advances, it will pave the way for more efficient plant breeding strategies and sustainable agricultural practices, ultimately contributing to global food security in the face of a growing population and climate change.

1.1 Problem Statement – Low-Cost Photogrammetry for Crop Phenotyping

While valuable, traditional techniques for analyzing plant growth for phenotyping come with several limitations that can impact the accuracy of results. A significant concern is the potential damage or alteration to the plant during data collection, leading to skewed data. Besides being labor-intensive, manual data collection is prone to errors, compromising result accuracy. Additionally, 2D imaging techniques commonly used in plant growth analysis are not able to capture

the full complexity of plant morphology. For example, these techniques can only partially capture the 3D structure of plants, often resulting in incomplete data representation.

Photogrammetry is a technique that involves capturing a series of photographs from different angles and using them to create precise 3D models of objects. This method is particularly beneficial in plant phenotyping because it enables detailed and accurate representations of plant structures without physical contact or harm to the plant. By utilizing photogrammetry in plant phenotyping, researchers can obtain comprehensive data about plant growth, morphology, and response to environmental factors. Photogrammetry enables the generation of 3D models from plant images, providing a more detailed analysis of plant structure and growth. Ensuring the accuracy and reproducibility of 3D models generated from plant images is challenging and requires careful calibration of imaging systems and sophisticated software tools. Therefore, there is a need to develop robust protocols and tools to enable reliable measurement of 3D plant growth.

1.2 Thesis Contribution

The main focus of this thesis is to demonstrate and provide an overview of using a low-cost, close-range photogrammetry rig in advancing plant phenotyping and developing new techniques and methodologies for plant growth analysis, leading to more efficient and effective plant breeding and crop management practices. The photogrammetry rig is designed to be user-friendly and functional, offering researchers, plant scientists, and breeders an accessible and accurate 3D scanning solution for analyzing their crop growth and improving their breeding techniques. In this work, we have demonstrated the capabilities of the photogrammetry rig and developed a high-throughput, quantitative trait analysis for wheat, capable of distinguishing between planophile and erectophile canopy structures. The integration of this technology is a step forward in advancing the field, highlighting the value of cost-effective photogrammetry techniques in the agricultural sciences.

1.3 Thesis Outline

Chapter 2 reviews research on plant phenotyping, highlighting the significant techniques and methods used for analyzing plant growth and development. This chapter provides insights into the various systems for capturing plant phenotypic data.

Chapter 3 delves into the details of photogrammetry and 3D reconstruction of objects, presenting a discussion of the underlying principles and concepts behind the photogrammetry process as well as describing the photogrammetry algorithm, Structure from Motion (SfM) used for 3D reconstruction. In this chapter, we cover the development process of the photogrammetry rig and show some initial results that were achieved.

Chapter 4 details the software implementation for controlling the photogrammetry rig and post-processing the point cloud data. This chapter thoroughly discusses the semi-automated process of acquiring plant image data to generate 3D plant models with the rig.

Chapter 5 gives an overview of the methodology, data preparation, image acquisition, and experiment done for wheat phenotyping with the photogrammetry rig.

In Chapter 6, we conclude our work and discuss future research directions. We summarize our research's essential findings and contributions and reflect on the broader implications of our work in plant phenotyping.

2. Review of Plant Phenotyping

2.1 Definition and Importance of Plant Phenotyping

2.1.1 Introduction to Plant Phenotyping

Phenotyping is a fundamental process in plant research that involves a set of methodologies and protocols used to measure plant growth, architecture, and composition with accuracy and precision at different scales of organization, from organs to canopies [9]. The term "phenotype" was first introduced by Danish botanist Wilhelm Johannsen in the early 20th century. He defined phenotype as an organism's observable properties produced by the interaction of the genotype and the environment [25]. Its ultimate objective is to describe the distinct correlation between the genetic makeup of the organism, or genotype, and its observable traits, otherwise known as its phenotype. This correlation is crucial in fields such as crop improvement, where identifying and propagating beneficial traits can substantially bolster productivity and sustainability [17].

Phenotyping has a profound history in plant research and agriculture, with origins intertwined with the inception of crop cultivation. Farmers unknowingly utilized phenotyping principles in the earliest stages of agriculture by selectively choosing to propagate the most fruitful, robust, or flavorful plants [26]. This practice guided the evolution of crop species over generations and shaped the agricultural landscape [27]. During these initial stages, phenotyping was primarily observational, heavily relying on easily discernible traits like plant size, fruit yield, seed quantity, and disease resistance. This early form of phenotyping was fundamental for domesticating wild species and creating the vast array of crop varieties that have sustained human civilizations for millennia.

As agriculture evolved into a more systematic and science-driven practice, phenotyping became more refined and integral to plant breeding strategies. Phenotyping moved beyond merely selecting high-yield plants; it now encompassed understanding the genetic underpinnings of these advantageous traits and manipulating them for crop improvement. This shift was a landmark in phenotyping history, paving the way for more targeted and effective breeding strategies. As plant breeding science advanced, phenotyping became more systematic, including morphological traits and physiological and biochemical characteristics.

The Green Revolution of the 20th century amplified the significance of systematic phenotyping, which was crucial in developing high-yielding, disease-resistant crop varieties [28]. However, the paradigm of plant research underwent a dramatic shift with the advent of the genomic revolution in the late 20th and early 21st centuries. The innovation in genomic sequencing technologies catalyzed an unprecedented surge in genotypic data. The resulting overflow of genetic information highlighted the urgent necessity for High-throughput Phenotyping (HTP) technologies, capable of matching the pace of genotypic data generation [16, 29]. A shift towards HTP is necessary to bridge the widening gap between our understanding of the genotype and phenotype, a challenge that traditional phenotyping methods need to be equipped to address. In this genomic era, the ability to rapidly and accurately phenotype many plants has become increasingly critical. This capability is essential to fully exploit the wealth of genotypic data and advance the understanding of plant biology and breeding [10].

Figure 2.1 shows the phenotyping process, encompassing a sequence of interconnected steps crucial to understanding and improving plant traits [8, 30, 31]. Beginning with the emergence of the plant, environmental data is monitored and integrated with the selection of plant germplasm and tailored experimental designs. The phenotyping workflows then systematically combine genomic data with quantitative measurements and specific phenotypic parameters, utilizing proximal sensing and imaging techniques. The methodologies, for example, are captured in the Genotype x Environment (GxE) analyses given by Ref. [8]. The entire process culminates in the extraction and understanding of specific plant traits. The phenotyping flowchart provides a complete view

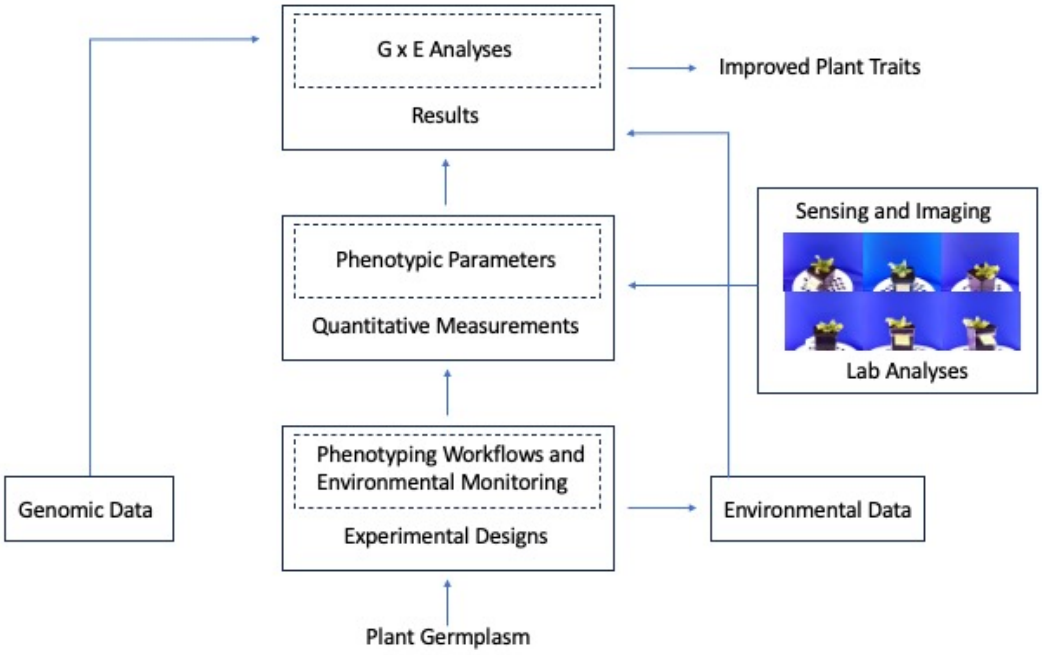

Figure 2.1: A scheme illustrating the systematic process of plant phenotyping. The chart shows the integral relationship between genomic data, environmental monitoring, proximal sensing, and quantitative measurements. The interaction of these elements guides the Genotype x Environment (GxE) analyses, which ultimately contributes to the targeted improvement of plant traits. (Image adapted from Ref. [8] with modification.)

of the dynamic interaction between genetic and environmental variables, highlighting the essential components and stages in the plant phenotyping process.

Despite its immense importance, phenotyping often poses a bottleneck to plant research and breeding programs. This hurdle becomes particularly pronounced with the rapid advancements in genotyping technologies, causing an overflow of genetic information. As emphasized in Ref. [16], this disparity underscores the need for robust, HTP methods to match the pace set by genotyping. One promising solution lies in the integration of imaging technologies into phenotyping. Innovative imaging techniques, such as hyperspectral, thermal, red, green, blue (RGB), and 3D imaging, can capture detailed, multilayered phenotypic data on a large scale, significantly accelerating data acquisition [32]. Coupled with sophisticated image analysis algorithms, these methods can extract valuable insights from raw image data, translating them into actionable phenotypic information.

Figure 2.2 shows the array of HTP technologies used in plant phenotyping, showing the diverse range of imaging and sensing methods utilized. HTP technologies are a crucial advancement in the agricultural and food industries, encompassing various applications that extend from estimating crop yields to assessing food quality after harvest. RGB imaging offers detailed visual assessments of crops and food products, while near-infrared (NIR) technology delves into the chemical composition of materials, which is essential for understanding nutrient content and detecting diseases. Fluorescence imaging provides insights into photosynthetic activity and plant health. Thermal imaging is instrumental in identifying water stress and disease presence in crops by detecting temperature variations. Multi- and hyperspectral imaging captures a broad light spectrum, revealing the physiological state and health information of plants. Lastly, 3D imaging technologies offer comprehensive spatial representations of plant structures, enabling precise volume and growth measurements [33].

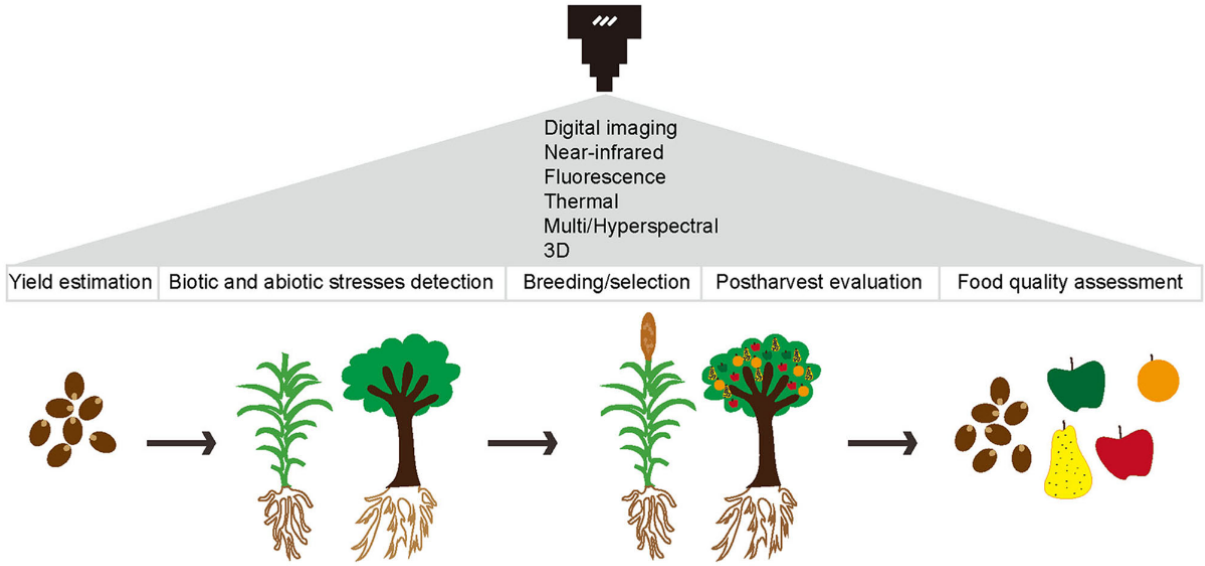

Figure 2.2: Diverse range of HTP technologies utilized in agriculture and food science, including digital, near-infrared, fluorescence, thermal, multi/hyperspectral, and 3D imaging. These technologies are important for applications ranging from crop yield predictions to post-harvest food quality assessments, revolutionizing the efficiency and sustainability of the food production systems. (Image adapted from Ref. [33].)

As a practice, plant phenotyping has been a cornerstone of plant breeding since the inception

of agriculture and has evolved significantly with advancements in technology. It is at the forefront of translating abundant genotypic data into meaningful, actionable information for plant biology and breeding. Despite challenges such as the phenotyping bottleneck, the rapid development of imaging technologies and robust data analysis tools offer promising solutions. Integrating these technologies into phenotyping practices will improve crop breeding and drive future agricultural innovation.

Genotyping and phenotyping should function together in an optimal setting, enriching and informing the other. This relationship is especially evident when specific phenotypes, such as stress resistance, are observed. Upon detection of these attributes, scientists can investigate the genome of the plant to pinpoint the specific genes accountable for such beneficial traits, an approach referred to as forward genetics [34]. For example, researchers in the study by Atwell and colleagues Ref. [35] found that by combining genome-wide association studies (GWAS) with HTP in a set of Arabidopsis thaliana inbred lines, they could link 107 phenotypic traits to specific loci in the genome of the plant. This work highlights the symbiotic relationship between genotyping and phenotyping, as they mutually enrich and inform each other.

2.1.2 Current Importance and Applications of Plant Phenotyping

Plant phenotyping is crucial across various areas such as agriculture, plant genetics, plant physiology, and bioengineering. It forms the basis for assessing reactions of plants to environmental stresses, essential in developing resilient crop varieties capable of withstanding harsh conditions, thereby contributing to sustainable agriculture. For instance, researchers applied HTP techniques to examine the physiological response of wheat to high temperatures and drought stress, enabling a deeper understanding of plant resilience under these adverse conditions Ref. [36]. Similarly, researchers demonstrated image-based phenotyping as a non-destructive screening method to assess different salinity tolerance traits in rice Ref. [37].

The shift towards predictive models in phenotyping holds potential for the future of plant

research and agricultural production. By combining machine learning and artificial intelligence with HTP, researchers can predict plant responses to various environmental conditions before they occur [11]. When integrated with the voluminous data generated by HTP, these computational methodologies act as catalysts for significant advancements in the field [38]. More specifically, they equip researchers with the sophisticated tools needed to construct predictive models, thereby ushering in a transformative era in phenotypic analysis. These models can simulate plant growth patterns and performance across diverse environmental conditions with an accuracy that was previously unattainable. Integrating machine learning and artificial intelligence applied to phenotypic data opens up novel avenues for plant science research. Figure 2.3 shows the relationship between various imaging technologies and their plant phenotyping and trait analysis capabilities. This figure presents an overview of how specific regions of the electromagnetic spectrum align with different imaging systems, each tailored to capture distinct types of phenotypic data. The imaging systems, categorized as I through V, encompass various techniques, including RGB, fluorescence, thermal, multi/hyperspectral, and 3D imaging.

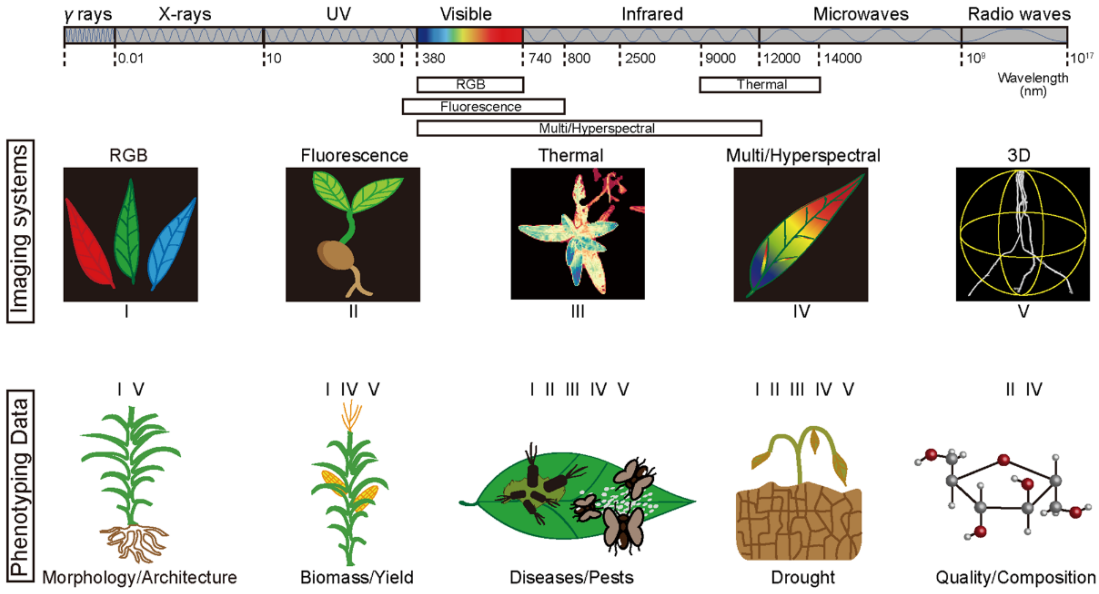

Figure 2.3: The alignment of specific regions of the electromagnetic spectrum with corresponding imaging systems plays a role in determining the types of phenotyping data that these systems can capture. The imaging systems, categorized as I, II, III, IV, and V, correspond to RGB, fluorescence, thermal, multi/hyperspectral, and 3D imaging, respectively. (Image adapted from Ref. [33].)

In one study, convolutional neural networks (CNN) were used to estimate wheat yield by analyzing wheat spikes, a critical metric in grain production Ref. [39]. Also, researchers improved maize yield predictions by integrating environmental data into genomic prediction models, identifying temperature at the flowering stage, water intake during vegetative, grain filling stage, and soil organic matter content as crucial yield predictors Ref. [40]. A further study utilized machine learning algorithms to predict soybean seed yields from hyperspectral reflectance data collected from 250 genotypes, indicating that certain growth stages and reflectance bands are optimal Ref. [41].

Precision agriculture has emerged as a vital practice, leveraging advanced phenotyping technologies for real-time crop monitoring and management. For instance, Baggio's work on distributed wireless sensor networks has made strides in intelligent irrigation systems, enabling farmers to make data-driven decisions about watering and fertilizing Ref. [42]. In a related study, researchers worked on remote sensing approaches to predict wheat yield at the field scale with high-resolution satellite imagery and crop stress-related indices, underscoring the role of spaceborne platforms in crop assessment Ref. [43]. These developments are part of an ongoing trend toward technology-driven agriculture, where real-time insights and predictive analytics merge to enhance crop productivity and sustainability.

Plant phenotyping also has a role in understanding climate change effects on crops, aiding in identifying traits and genes that help plants survive in harsh conditions. In Ref. [36], researchers developed machine learning models to predict wheat biomass and identified adaptive traits for coping with high temperatures and water deficit, such as transpiration efficiency and changes in carbohydrate and antioxidant metabolism. Another proposed a methodology for breeding wheat varieties with deeper root systems to better use deep stored water in water-limited environments Ref. [44]. This research can be seen as a response to climate change, where unpredictable rainfall and water scarcity are expected to challenge traditional agricultural practices, requiring the development of more water-efficient crop varieties. These findings can support breeding programs in enhancing wheat resilience to climate change. This data can be used to breed crops designed explicitly for a shifting climate, underscoring the significance of plant phenotyping in plant science

advancement and food security in the face of rapid climate change.

In agronomy, plant phenotyping is crucial in studying cultivation practices and their impact on crop performance, including planting density, irrigation, fertilizer application, and pest management. Phenotyping and imaging technologies overcome the limitations of traditional methods, enabling detailed, large-scale analyses of crop traits under various conditions, thereby enhancing understanding of crop responses to diverse farming practices and environmental factors, refining agricultural methodologies, and boosting productivity [45]. Through interdisciplinary collaborations and the adoption of automation, remote sensing, and data integration, these cutting-edge technologies facilitate a precise mapping of genetic factors tied to phenotypic variation [17], underlining the significant impact of phenotyping in agronomy.

Building on these developments in agronomy, the integration of high-throughput and next-generation phenotyping technologies opens a new chapter for this field. These advanced tools allow an understanding of genotypes, phenotypes, and environmental factors, illuminating the multifaceted mechanisms that govern crop resilience and productivity. These strategies range from selective breeding of resistant varieties to cutting-edge genomic selection and gene editing techniques. With the growing challenge of feeding a burgeoning global population amid climate change, the critical role of phenotyping technologies in promoting sustainable, resilient, and productive agricultural systems becomes increasingly apparent.

Plant height, a phenomic trait, is an essential morphological and developmental characteristic that often correlates with overall plant growth and can indicate potential grain yield and biomass. Researchers evaluated the performance of five different sensing technologies for field-based HTP of sorghum height Ref. [46]. The technologies evaluated included an ultrasonic sensor, a LIDAR-Lite v2 sensor, a Kinect v2 camera, an imaging array of four high-resolution cameras mounted on a ground vehicle platform, and a digital camera mounted on an unmanned aerial vehicle platform. The research confirmed the ability of these technologies to measure this trait precisely, facilitating improved agronomic practices and more efficient crop management.

2.2 Plant Phenotyping Techniques

2.2.1 Traditional Plant Phenotyping Techniques

Historically, phenotyping has been performed using traditional methods, which have relied on manual, visual observations and assessments [16]. For instance, a researcher might measure the height of a plant using a ruler or weigh a sample of seeds using a scale. These methods can be time-consuming and labor-intensive as each plant must be individually measured and the data manually recorded [10]. Traditional techniques often require physical contact with the plant. This interaction can cause damage or stress, subsequently affecting the growth and development of the plant. Despite these challenges, traditional phenotyping techniques have provided foundational knowledge about plant traits, serving as the basis for much of our current understanding of plant genetics and biology.

In addition to direct measurements, traditional phenotyping techniques often involve visual assessments of plant characteristics, such as color, shape, or disease symptoms [17]. These assessments are typically based on established scales or grading systems, which attempt to standardize the subjective nature of visual observation. For example, in grading a quantitative trait index designed to distinguish between erectophile and planophile leaf orientations, researchers rely on subjective visual relative scales from 1 to 10. In this approach, a maximum score of 10 indicates that all leaves at the top of the canopy are floppy, a median score of 5 denotes that half of the plants are erect, and a minimum score of 1 is assigned when all leaves are in an erect position [47]. While these visual assessments can provide helpful information, they are inherently subjective and vary based on the judgment and experience of the observer. Visual assessments, like direct measurement methods, can be demanding regarding time and labor, limiting their suitability for large-scale studies or tracking changes over time.

The execution of traditional phenotyping techniques can become even more challenging when

dealing with the assembly of necessary genetic resources. Screening a population for a valuable agricultural trait demands conducting replicated trials across multiple environments over various seasons [45]. This process often requires destructive harvests at specified times or particular phenological stages, which adds to the complexity and expense. Testing a promising candidate gene for allelic variation in a mapping population also calls for precise phenotyping work. Due to the intensive nature of traditional field phenotyping, many crop breeding programs have resorted to taking a single measurement of final yield for replicated plots in contrasting environments across multiple seasons. As technology advances, it opens doors to methods that build upon the foundational knowledge provided by traditional techniques, offering more precise, scalable, and less labor-intensive ways to study plant traits.

2.2.2 2D Imaging Plant Phenotyping Techniques

Emerging 2D image-based phenotyping technologies have revolutionized plant phenomics, addressing the limitations of traditional phenotyping methods. These innovative techniques have significantly improved the efficiency, precision, and range of plant trait observation. With high-resolution capabilities, contemporary 2D imaging methods facilitate the collection of multi-dimensional, multi-parametric data, yielding unprecedented detail. Furthermore, the versatility of these imaging systems, deployable in various settings from controlled environments like growth chambers and greenhouses to open field conditions, significantly broadens the scope and context of phenotyping studies [8]. The incorporation of time-lapse photography enables the exploration of dynamic traits that evolve, such as plant growth rates or circadian rhythms [32]. These techniques allow continuous monitoring of plant traits over time, enabling researchers to observe the growth progression and stress impacts on individual plants in real-time.

Digital RGB cameras are integral to these advancements, which provide a wealth of invaluable information despite their simplicity. They capture 2D snapshots of plants that can be analyzed for an array of morphological traits. Depending on the application, images may be captured from vari-

ous perspectives—overhead, lateral, or multiple angles—generating a comprehensive visual profile of the plant. A notable advantage of 2D digital imaging is its relatively low cost and high-speed operation, which makes it particularly suitable for HTP [8]. The automation of image acquisition can phenotype hundreds or even thousands of plants within a day, significantly increasing the productivity of large-scale breeding programs or genetic studies. Coupled with recent advancements in image analysis software, the extraction of traits from these images has been streamlined, reducing the need for manual intervention and the associated subjectivity.

Direct measurements from image data can shed light on several key traits. Biomass measurement can indicate the health and productivity of the plant [48, 49]. Leaf characteristics often influence the photosynthetic efficiency of the plant and can reflect adaptations to specific environmental conditions [50, 51]. Yield-related traits directly affect agricultural productivity, with significant implications for food security [52]. Lastly, the response of plants to biotic and abiotic stress can significantly impact its survival and reproductive success, with potential consequences for crop yield and resilience in the face of environmental changes [53].

Adopting 2D imaging in plant phenotyping thus represents a significant leap forward in plant science. Its capacity to yield quantitative, time-sequenced data has made it an essential tool for precisely characterizing plant phenotypes, offering insights into the fundamental processes that govern plant growth, development, and responses to environmental stressors. These image-based measurements enable a deeper understanding of plant biology, making it possible to link genetic variations with plant performance traits.

2.2.3 3D Imaging Plant Phenotyping Techniques

Plant phenotyping research covers a range from broad plant canopies to individual organs and benefits significantly from 3D imaging. By capturing both external and internal characteristics, 3D imaging offers a more detailed and holistic approach than 2D imaging [54]. Here, non-destructive 3D imaging is invaluable as it allows continuous monitoring over time, discerning between genuine

growth and simple plant movement at multiple scales [55]. This dynamic understanding of plant development uncovers subtle changes over time that may be imperceptible to the human eye. As the field integrates genomics, plant function, and agricultural traits, it greatly relies on the detailed geometry and growth measurements of 3D imaging. This tool can assist researchers in dissecting plant phenome complexity and associating genetic variations with phenotypic expressions.

Advances in 3D imaging and processing techniques significantly impact the agricultural sector through increased automation and robotics. Autonomous systems are now being deployed for selective harvesting, precise weeding, and targeted spraying operations [56]. In agricultural biotechnology, an ongoing effort is to enhance crop traits such as yield, drought resistance, pest, and herbicide resistance by correlating genotypes with phenotypes [57]. These developments necessitate advanced vision systems, where applications across domains like phenotyping, inspection, process control, and robot guidance increasingly favor 3D methods over traditional 2D approaches.

Compared to 2D imaging, 3D offers a combined perspective of plant structures, gathering data from the surface to the internal segments [19]. The ability to amalgamate data from various viewing angles offers insights that might be challenging to achieve with a 2D model alone. One such insight could involve resolving occlusions, which are areas in the structure of the plant hidden from view [7]. By reconstructing the plant distance, orientation, and illumination, these methods could help deal with the crossings of plant structures, where different plant parts overlap or intertwine. The 3D models of reconstructed plants could be utilized to estimate the biomass of the plant [7, 58], prediction of yield parameters [59], identification of disease symptoms [60], quantification of architectural traits such as for the leaf area, stem height, and canopy volume [7,61], and exploration of plant responses to various stress factors [62].

LiDAR uses a pulsed laser to measure distances, providing detailed 3D data that includes internal plant structures such as branching architecture and leaf density [55]. A research initiative, for instance, used a high-resolution portable scanning LiDAR to estimate wheat vertical plant area density profiles at different growth stages Ref. [63]. In another study, researchers developed a

method for rapidly mapping the Leaf Area Index (LAI) using ground-based laser rangefinders—a LiDAR-based method—mounted on a vehicle Ref. [64]. The LAI, representing the ratio of leaf area to a given unit of land area, is vital in assessing plant productivity and informing agricultural management decisions. However, the high costs associated with LiDAR can limit its application.

Other 3D imaging sensor technologies offer valuable capabilities, including stereo vision and structured light. Researchers used structured light approaches for trait analysis such as the number of leaves, plant height, leaf size, and internode distances Ref. [65]. Researchers in the study Ref. [66] utilized a high-precision laser scanning system to non-invasively capture the 3D architecture of barley plants, focusing on traits such as leaf area, stem height, and overall plant volume, thereby significantly advancing the capabilities of plant phenotyping and growth monitoring in cereal crops. Stereo vision employs multiple cameras to capture different perspectives, providing detailed surface information at a lower cost. However, it can struggle with complex overlapping structures. Structured light sensors project a pattern onto the plant, and combined with photogrammetry, generate high-resolution 3D models. They excel at capturing fine details of plant morphology but are limited by their shorter working distances [54, 55] and may impact the natural physiological state of the plant and alter its original texture and color [67].

Advancements in 3D imaging technologies have profoundly impacted plant phenotyping, offering more comprehensive and detailed insights into plant structure and behavior than ever before. These technologies, ranging from LiDAR to stereo vision and structured light sensors, have broadened the scope of phenotypic analysis, allowing for more accurate assessments of plant health, growth, and productivity. The next section will focus specifically on photogrammetry, another 3D imaging technique that has shown significant promise in bridging the gap between detailed phenotypic data acquisition and practical application in diverse agricultural and research settings.

2.3 3D Plant Phenotyping with Photogrammetry

Structure from Motion (SfM) is an efficient photogrammetry technique that leverages sequential overlapping images to construct detailed 3D models. The cost-effectiveness and simplicity in sensors and hardware, and straightforward application make SfM highly suitable for a wide range of phenotyping tasks. This technique, which synthesizes high-resolution 3D models, has become increasingly prominent due to its accuracy, cost-effectiveness, and versatility. SfM is a non-invasive method that offers a comprehensive insight into plant morphology, which is crucial for understanding various growth patterns and responses to environmental stimuli.

Despite its computational demands and challenges with complex, self-occluding plant structures, the affordability and the detail SfM offers in plant models have led to its wide adoption in research. This utility of SfM is highlighted in several studies. For instance, researchers have utilized SfM for the 3D analysis of cotton plants, allowing for precise measurements of stem height, leaf width, and leaf length Ref. [68]. Similarly, another study estimated biomass in eggplant, tomato, and cabbage crops using SfM, based on a 3D point cloud analysis of images collected by unmanned aerial vehicles (UAVs) Ref. [69]. Researchers used SfM in growth analysis studies in open field settings, particularly in measuring plant height and canopy in crops like maize and sorghum Ref. [70].

In the context of specific plant trait analysis, SfM has been employed to study the shapes of calyxes and achenes in strawberries [71]. In multi-plot research settings, SfM has been valuable in quantitative trait locus (QTL) analysis for crops like pepper, assessing traits such as plant height and leaf angle [72], understanding the drought response in soybeans, a significant aspect in the study of plant stress tolerance [73]. In experimental field studies, the technique has been effectively used for trait analysis in crops like maize and sorghum, focusing on the LAI, and in grapevines for leaf area assessments [74, 75].

Open-source 3D plant phenotyping and photogrammetry techniques transform how researchers

approach plant modeling, reconstruction, and analysis. By leveraging a combination of low-cost hardware, such as programmable turntables and cameras, and open-source software, researchers can create detailed 3D scans of individual plants with complex architectures. Furthermore, the open-source nature of these techniques encourages collaboration and innovation within the scientific community, making them accessible to researchers with various budget constraints. For instance, researchers have developed a low-cost, open-source 3D scanning system and data processing pipeline for accurately assessing the 3D architecture of chickpea plants, species with complex branching patterns and small leaves Ref. [7]. Using photogrammetry techniques, they demonstrated the capability of the system to measure vital architectural traits such as canopy volume and growth rate with high accuracy ($R^2 > 0.99$, mean absolute percentage error < 10%), offering a promising tool for enhancing phenotyping in crop research. Figure 2.4 shows an example of a close-range photogrammetry rig where researchers have created 3D plant models to study and test optimum shooting angle. The photogrammetry rig consists of 10 cameras, a stable structure for the cameras, two fluorescent lamps, a rotary table, and a black backdrop.

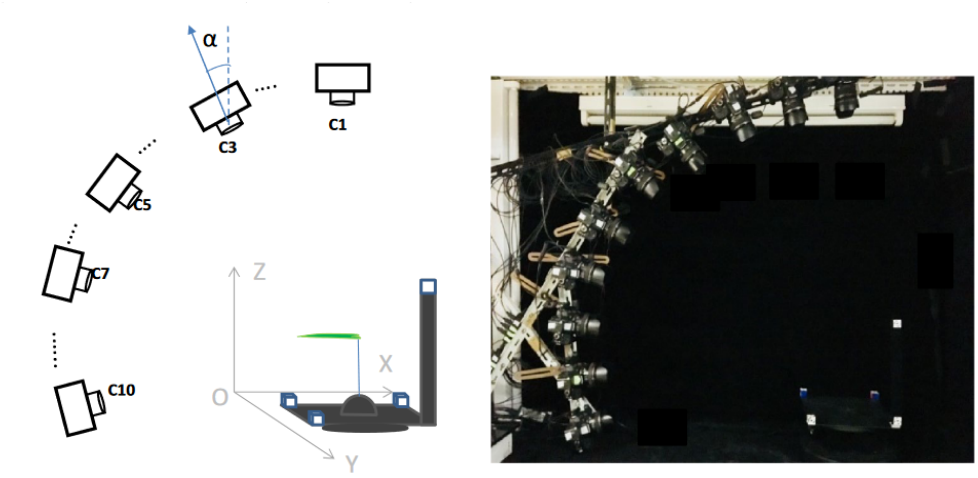

(a) Simple schematic of the close-range photogrammetry rig

(b) The multi-camera photogrammetry imaging system

Figure 2.4: Researchers developed an imaging system that uses photogrammetry to reconstruct a digital 3D model of plants to test the optimal shooting angle. (a) The schematic of their system showcases the layout and operational design. (b) A photograph of the actual system, which consists of 10 cameras, two fluorescent lamps, a black backdrop, and a rotary table. (Image adapted from Ref. [67].)

Considering the cost, resolution, and operational flexibility balance, SfM is the superior choice for 3D modeling in plant phenotyping. Unlike other methods, SfM strikes an optimal balance between detailed data capture and cost-effectiveness, making it suitable for various phenotyping tasks. Its use of standard cameras and the ability to process images into detailed 3D models aligns well with the requirements of plant phenotyping, especially in projects constrained by budget and resource availability. Therefore, SfM meets the technical demands of plant phenotyping and addresses the practical considerations of cost and ease of use.

This work will focus on integrating and applying these open-source 3D phenotyping and SfM-photogrammetry techniques to advance plant phenotyping within the fields of plant biology and agriculture. However, we aim to demonstrate a system that is semi-autonomous and affordable for researchers, plant scientists, and breeders. The goal is to streamline the image capture process and expedite the production of 3D phenomic data. This approach not only makes the field of phenotyping accessible to a broader range of researchers but also enhances the precision of the data collected. This thesis will encompass the entire workflow, from the hardware setup to the intricacies of the software processing and the capabilities of the system to extract novel plant traits. We see the photogrammetry rig as an invaluable resource for researchers, offering a multifaceted tool for their research.

3. Design and Implementation of the Photogrammetry Rig

This chapter provides an in-depth examination of the hardware development and utilization of the photogrammetry rig. Section 3.1 gives an overview of the basic principles and hardware requirements of photogrammetry and describes the SfM algorithm. In Section 3.2, we briefly summarize the design of the photogrammetry rig. Section 3.3 gives a complete system overview of the photogrammetry rig, describing the hardware components in more detail and the price points of the imaging system. Following that, in Section 3.4, we discuss initial results achieved with the photogrammetry rig.

3.1 Basic Principles and Hardware Requirements of Photogrammetry

Photogrammetry is a multidisciplinary field that merges the techniques of photography, optics, and surveying to extract detailed information about physical objects and environments from photographic imagery. Traditional photogrammetry methods draw a parallel to human binocular vision, where depth perception is achieved from two known relative points. However, depth, volume, or 3D features can also be discerned from a single observation point if there is movement between the observer or the object [76, 77]. The fundamental principle underpinning photogrammetry is triangulation. By capturing photographs from at least two locations, "lines of sight" are formed from each camera to specific points on the object. These lines of sight, often called rays due to their optical nature, are mathematically intersected to calculate the three-dimensional coordinates of the

points of interest. Figure 3.1 shows a stereo camera pair used in stereoscopic photogrammetry which enables the creation of 3D models and maps from 2D images. The accuracy of these models depends on various factors, including the quality of the photographs, the precision in camera placement, and the sophistication of the software used for processing the images.

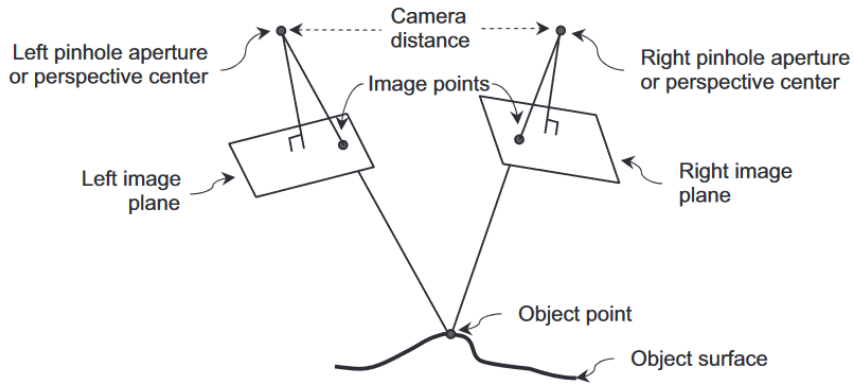

Figure 3.1: This diagram illustrates the components of a stereo camera system, including the left and right cameras with their respective image planes, pinhole apertures, and image points. The figure also highlights the camera distance, the object point derived from triangulation, and the object surface being imaged. (Image adapted from Ref. [78].)

Structure from Motion, or SfM, is based on computer vision and allows photogrammetric reconstruction from images alone, providing a more flexible approach than traditional methods. In contrast to traditional stereophotogrammetry, which depends on predetermined camera positions and orientations, SfM can compute 3D information from overlapping images without requiring prior knowledge of the camera or reference points in the scene [79]. This adaptability permits using more affordable imaging platforms for aerial and terrestrial applications. The strengths of SfM include automatic identification and alignment of features within images, irrespective of scale, viewing angles, or orientations—beneficial in scenarios with small or unstable platforms. Moreover, SfM algorithms can operate without preset camera positions or ground control points, simplifying or automating camera calibration. This reduces the need for strict uniformity in image overlap, camera positioning, and calibration. While SfM-photogrammetry often describes the entire reconstruction workflow, from image capture to dense point cloud creation, it specifically

refers to a process that yields camera parameters and a sparse point cloud, which are fundamental to the broader photogrammetric process.

Recent studies have focused on innovative applications and frameworks within the field. Notably, Ref. [80] presents a cost-effective, open-source SfM framework specially developed for creating high-fidelity 3D models of arthropods and small-scale objects. Photogrammetry is applicable across a broad spectrum of industries and scientific disciplines. Empirical studies and interdisciplinary projects have increasingly adopted photogrammetric techniques, contributing to their respective domains. Substantial advancements have been achieved in the domain of cultural heritage conservation, particularly in the digitization of museum specimens and artifacts. These improvements are evidenced by the efficient and cost-effective 3D photogrammetry techniques and pipelines, as highlighted in studies such as Refs. [81–85]. The scope of photogrammetry extends to documenting archaeological sites, landscapes, features, and materials, enhancing its application in historical and environmental research [86–89]. SfM-photogrammetry has also been used in more technical fields, such as the aerospace industry [90], 3D shape measurement [91], and civil engineering with a focus on bridge inspection [92].

Figure 3.2 demonstrates the 3D reconstruction of a Moses statue, showcasing the integration of a camera network. It highlights the process of transforming 2D images captured from various angles around the statue into a sparse point cloud, serving as a foundational step towards achieving a detailed 3D model which facilitate the preservation and study of cultural heritage artifacts. In all these studies, a common thread is the emphasis on essential equipment and techniques, such as a high-quality camera, a stable tripod, attention to lighting and background, photogrammetry software, the use of appropriate lenses for minimal distortion, control points for accurate alignment, and powerful computing hardware for processing, and adequate data storage solutions. We have chosen the SfM approach for our photogrammetry rig due to its flexibility in image capture and ability to generate highly detailed models. Details of the SfM algorithm will be further elaborated in the next section.

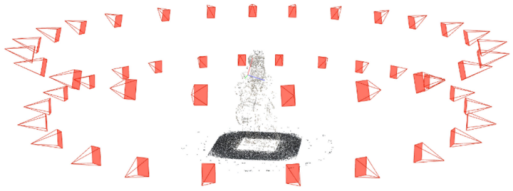

(a) Sparse point cloud for the 3D reconstruction of the Moses statue.

(b) Fully reconstructed Moses statue.

Figure 3.2: The setup for the 3D reconstruction of a Moses statue. (a) Illustrates the integration of the camera network and the generation of the sparse point cloud from 2D images taken around the subject. (b) Shows the fully reconstructed Moses statue after removing noise and outlier points. (Image adapted from Ref. [83].)

3.1.1 Structure from Motion

SfM is a photogrammetric technique for estimating 3D structures from sequences of 2D images. It identifies common points or features across these images, utilizing perspective differences to triangulate their 3D positions. The typical output of SfM includes a sparse 3D point cloud accompanied by camera parameters such as position and orientation for each image. The process follows an incremental approach, with an initial phase of correspondence search between images leading to a second phase of iterative, incremental reconstruction. Hartley and Zisserman's work [93] provides an in-depth explanation of the SfM algorithm, which will be briefly summarized in this section. Figure 3.3 outlines the pipeline of the SfM algorithm, starting from the initial image input. The process is organized into several interconnected stages that begin with correspondence search, feature extraction, and image matching, followed by geometric verification to affirm the accuracy of matches. The pipeline then progresses into the incremental reconstruction phase, including image registration, triangulation, and bundle adjustment. This thesis will utilize COLMAP, a versatile and open-source photogrammetry platform photogrammetric software featuring a SfM and Multi-View Stereo (MVS) pipeline, with both graphical and command-line interfaces, capable of reconstructing ordered and unordered image collections [94].

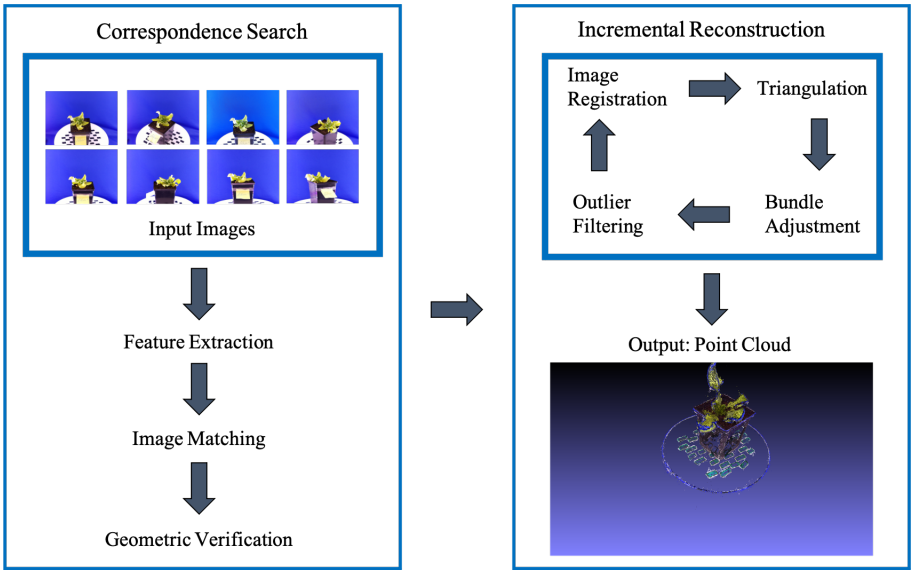

Figure 3.3: Full pipeline of the SfM algorithm. This process involves two stages, beginning with correspondence search, which includes feature extraction, image matching, and geometric verification. The pipeline then progresses to the next stage, called incremental reconstruction. This stage encompasses image registration, triangulation, and bundle adjustment with outlier filtering, generating a point cloud. (Image adapted from Ref. [94] with modifications.)

The initial stage of SfM, the correspondence search, involves identifying scene overlaps in the input images given by

$$I = \{\, I_i \mid i = 1 \ldots N_I \,\}, \tag{3.1}$$

where I is a collection of images, each image in the set is denoted by I_i. The index i is used to differentiate each image in the set, and it ranges from 1 to N_I, with N_I being the total count of images in the set.

Each input image I_i is processed for feature extraction to generate a collection of local features that describe the points of interest (key points) within it. The Scale-Invariant Feature Transform (SIFT [95]) is a widely used method for feature extraction in SfM applications. SIFT identifies sets of local features at specific locations within each image as shown in Figure 3.4. A requirement for these features is their identifiability across multiple images, achievable only if they are invariant to

geometric and radiometric transformations [94]. The feature extraction results in a set of critical points and features for each image is given by

$$F_i = \left\{ \left(\mathbf{x}_j, \mathbf{f}_j\right) \mid j = 1 \ldots N_F \right\}, \tag{3.2}$$

where F_i denotes the set of features in the i-th image, with $\mathbf{x}_j$ representing the location of the j-th key-point and $\mathbf{f}_j$ its descriptor.

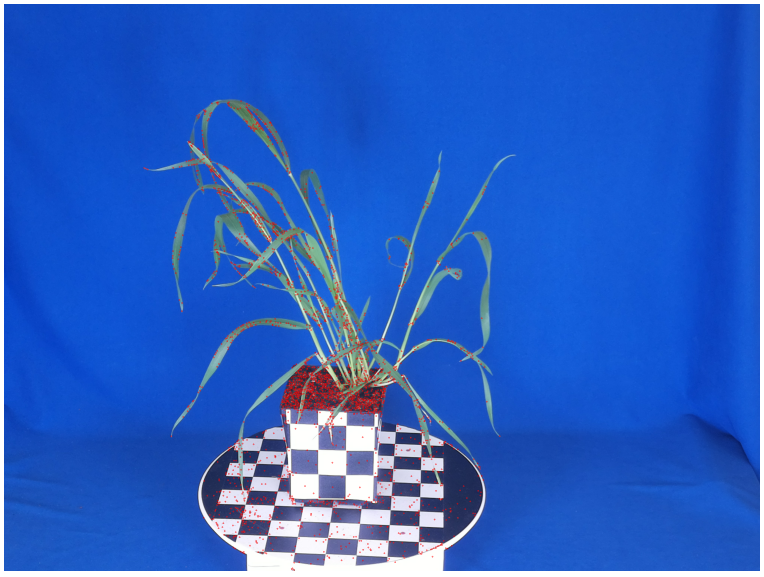

Figure 3.4: Image capture of wheat from the photogrammetry rig. This image shows the key points extracted by COLMAP, highlighting areas for 3D model construction. Features, highlighted as red dots, are essential for matching different images in the dataset, enabling COLMAP to reconstruct the spatial geometry of the scene accurately. The extraction and identification of these points are fundamental, allowing for the precise alignment and stitching of images to generate a cohesive 3D model.

Once feature extraction is completed, the next step is to match these feature points across different images to establish correspondences. In the feature matching stage, the goal is to identify commonalities between images, which indicate overlapping parts of the scene. A match is established when two points in different images share the same descriptor, implying they represent the same point in the scene. SfM achieves this by utilizing the appearance descriptors of the images, which encapsulate the features within them. This matching process involves evaluating

each pair of images for scene overlaps; if such an overlap is detected, corresponding features between the images can be identified. The output is a set of potentially overlapping image pairs $C = \{\{I_a, I_b\} \mid I_a, I_b \in I, a < b\}$ and their associated feature correspondences $M_{ab} \in F_a \times F_b$ [94]. Figure 3.5 illustrates the process of matching two images through COLMAP, green lines idicate that a feature from image A is matched with the same feature on image B.

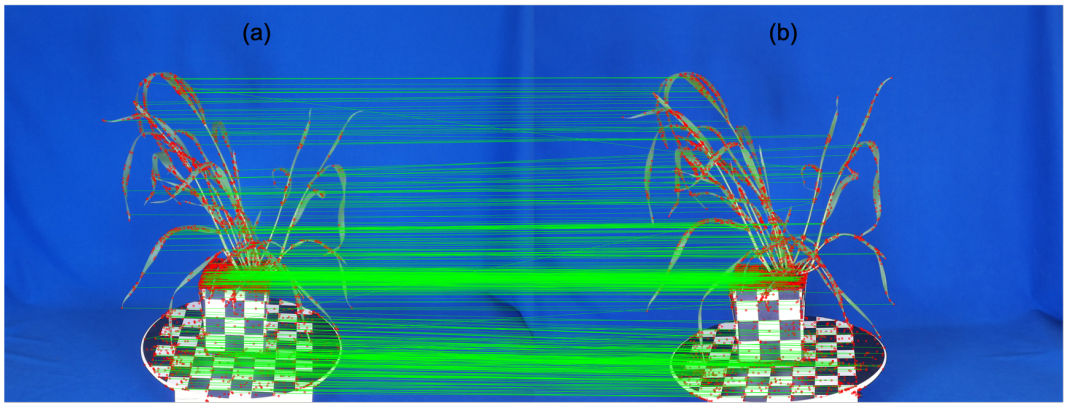

Figure 3.5: Two different angles on the vertical axis were capture with the photogrammetry rig where (a) is from camera A and (b) is from camera B. Here the green lines indicate the identical features found between the two different images. This step is essential for integrating numerous images by pinpointing shared points of interest. By successfully matching these features across various images, COLMAP can infer the spatial relationships and geometric configurations of the scene.

The next stage involves geometric verification, which identifies a transformation that accurately maps corresponding points between two images. Successful mapping leads to the geometric verification of the image pair, signifying that the matched points correspond to the geometry of the scene. These methods are contingent upon whether the intrinsic calibration parameters of the cameras are known. Due to the presence of outliers in the correspondences established during the matching phase, the application of robust estimation methods, such as RANSAC (Random Sample Consensus [96]), becomes essential in the geometry verification process. A transformation is deemed geometrically verified if it successfully maps an adequate number of features between the images. The output is a Scene Graph, whose nodes represent images and edges join the pairs of images that are considered geometrically verified [97].

The next phase is incremental reconstruction, which is necessary, as a poor start can significantly compromise the accuracy of the 3D model. Optimal initialization typically begins in densely populated areas of the scene graph, utilizing correspondence redundancy to establish a solid foundation. Starting in areas with sparse image data can impede the bundle adjustment, leading to error accumulation and compromised results. This phase involves selecting images that have been geometrically verified and feature the most matches to anchor the reconstruction. It also includes setting the initial points and determining the poses of the first two cameras. Subsequent steps of image registration, triangulation, and bundle adjustment iteratively refine the model by adding new points. Each new image requires calculating the pose of the camera by correlating it with established 3D points. This involves solving the Perspective-n-Point (PnP) problem, often using RANSAC or similar methods to account for outliers, thereby laying the groundwork for the continuous enrichment of the model through triangulation [97].

The initial phase of the triangulation process identifies new images that share common points with the reconstructed 3D point cloud. This process is crucial for adding new points to the reconstruction, thereby increasing the density of the point cloud. It relies on pairs of registered images, and the estimation of camera poses to compute the 3D coordinates of shared points. Central to this phase is the application of the epipolar constraint, a geometric principle that restricts the search for corresponding points between image pairs to the epipolar lines, thereby facilitating the accurate determination of new point positions. This constraint is particularly vital in counteracting potential inaccuracies introduced in earlier stages of the pipeline, notably the reprojection error. Reprojection error refers to the discrepancy between the observed image points and the projected points derived from the 3D model, which can result from factors like camera calibration errors or inaccuracies in estimated camera poses. To mitigate the impact of these inaccuracies and ensure precise triangulation, specialized algorithms that apply the epipolar constraint and minimize reprojection error are used [97].

Following triangulation, bundle adjustment is used to refine the reconstruction by minimizing camera error, pose estimation, and point triangulation. The purpose of bundle adjustment is to

prevent inaccuracies in estimating the camera pose that propagates in the triangulation of points [98]. This phase, which uses the Levenberg-Marquardt (LM) algorithm for non-linear least squares optimization, aims to produce optimal values for the 3D coordinates of scene points and camera calibration parameters. Bundle adjustment, which can be computationally intensive, is performed locally and globally to manage processing time effectively, ensuring that errors do not accumulate and adversely affect the reconstruction quality. Figure 3.6 shows a view of the model generated in the graphical interface of COLMAP. It depicts spatial positioning of each camera and orientation for the sparse model as shown in Figure 3.6(a) and the final dense point cloud as shown in Figure 3.6(b).

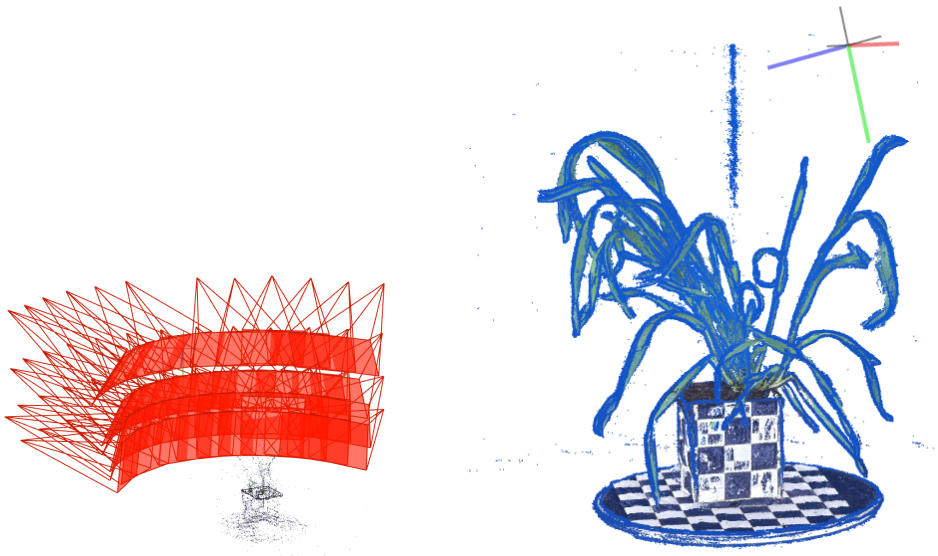

(a) Sparse point cloud (b) Dense point cloud

Figure 3.6: This figure shows two stages in 3D reconstruction using COLMAP: (a) illustrates the sparse model generated, highlighting the camera viewpoints that contribute to its construction, and (b) illustrates the dense point cloud, which represents a more detailed reconstruction derived from the initial sparse model.

The goal is to concurrently refine the 3D coordinates of scene points $\{P_j\}_{j=1}^{p} \subseteq \mathbb{R}$ and the calibration parameters of each of the n cameras. This refinement aims to reduce the difference between the actual image measurements and their expected projections based on the model. Specifically, for pairwise point correspondences between images, we represent the unknown positions of scene

points as $\{P_j\}_{j=1}^{p}$ within the three-dimensional space, and the 3×4 camera projection matrices as $\{C_i\}_{i=1}^{n}$. Each matrix C_i incorporates the positional, orientation, and internal calibration details of camera i. Moreover, the coordinates $(x_{ij}, y_{ij}) \in \mathbb{R}$ correspond to the observed projections of point P_j on the image plane of camera C_i.

The bundle adjustment problem aims to minimize a least squares cost function defined as

$$\underset{\{\mathbf{P}_j\},\{C_i\}}{\text{minimize}} \sum_{i \sim j} \left(x_{ij} - \frac{C_{i1}^T \mathbf{P}_j}{C_{i3}^T \mathbf{P}_j} \right)^2 + \left(y_{ij} - \frac{C_{i2}^T \mathbf{P}_j}{C_{i3}^T \mathbf{P}_j} \right)^2. \tag{3.3}$$

Here, $C_{ik} \in \mathbb{R}$ signifies the kth row of C_i for $1 \leq k \leq 3$. The notation $i \sim j$ denotes that the scene point j is observable by camera i. P_j is expressed in homogeneous coordinates as $[P_j, 1] \in \mathbb{R}$, allowing for a unified representation of both translation and rotation in the projection calculations [99]. The camera poses and parameters obtained from SfM are then applied to generate a densified point cloud using an MVS algorithm [79].

3.2 General Design and Implementation of the Photogrammetry Rig

The development of the photogrammetry rig involves numerous factors, including the arrangement and number of cameras, lighting conditions, and attributes of the objects to be imaged. The goal is to construct a uniform environment for capturing images of plants, enabling consistent image capturing. Each design element enhances data capture efficiency, paving the way for effective 3D reconstruction. A typical photogrammetry rig incorporates a stationary or movable platform with well-positioned cameras surrounding the subject. For the photogrammetry rig, we will consider a movable platform, such as a rotary table, to obtain different viewpoints.

The subject and the desired resolution of the resulting 3D model influence the number and layout of cameras within the rig. Camera arrangements may vary, ranging from simple circular

patterns to more multi-row configurations tailored to the specific requirements of the subject being imaged. This planning ensures sufficient overlap between images, crucial for accurate point alignment during reconstruction. This work will focus on four stationary cameras positioned at different angles on the vertical plane, mounted on a fixed structure, to provide stability and consistency in capturing the necessary viewpoints.

Lighting conditions are also important, requiring careful planning to distribute light uniformly, reducing shadows and reflections that might compromise image quality. Various tools, such as diffusers and reflectors, may achieve this balance. Additionally, it is essential to consider specific characteristics of the subject, including size, shape, color, and reflectivity. These elements influence the camera and lighting arrangements, ensuring the rig is customized to highlight the primary attributes of the subject. This customization facilitates accurate and reliable 3D modeling. Two LED lights facing the subject with a featureless blue backdrop for the background would be sufficient for the photogrammetry rig.

3.3 Full System Overview

Figure 3.7 shows two distinct views of the photogrammetry rig. As shown in Figure 3.7(a), the back view illustrates the structural framework, revealing how the various components are arranged and integrated. The positioning of the electronic components, including the Raspberry Pi and the camera kit, is visible, demonstrating the placement of the main components of the rig. Here, one can see the arrangement of the LED lights, positioned to provide uniform illumination. The motorized turntable is central to the functionality of the rig, visible in the back view. The turntable allows for a complete 360-degree rotation of the object being imaged, essential for capturing multi-angled views. The main structure uses aluminum extrusion mounted on a plywood base, designed to bear the weight of the entire setup and provide stability during image capture. Once the base is firmly in place, attention is given to its leveling, ensuring it is perfectly horizontal. Next, the turntable is placed onto the plywood base and interfaces with the Raspberry Pi and the stepper

motor. Figure 3.7(b) complements this perspective by showing the operational setup of the rig and the subject being imaged. The matte blue backdrop, serving as a featureless background, enhances the clarity of the captured images by eliminating reflections.

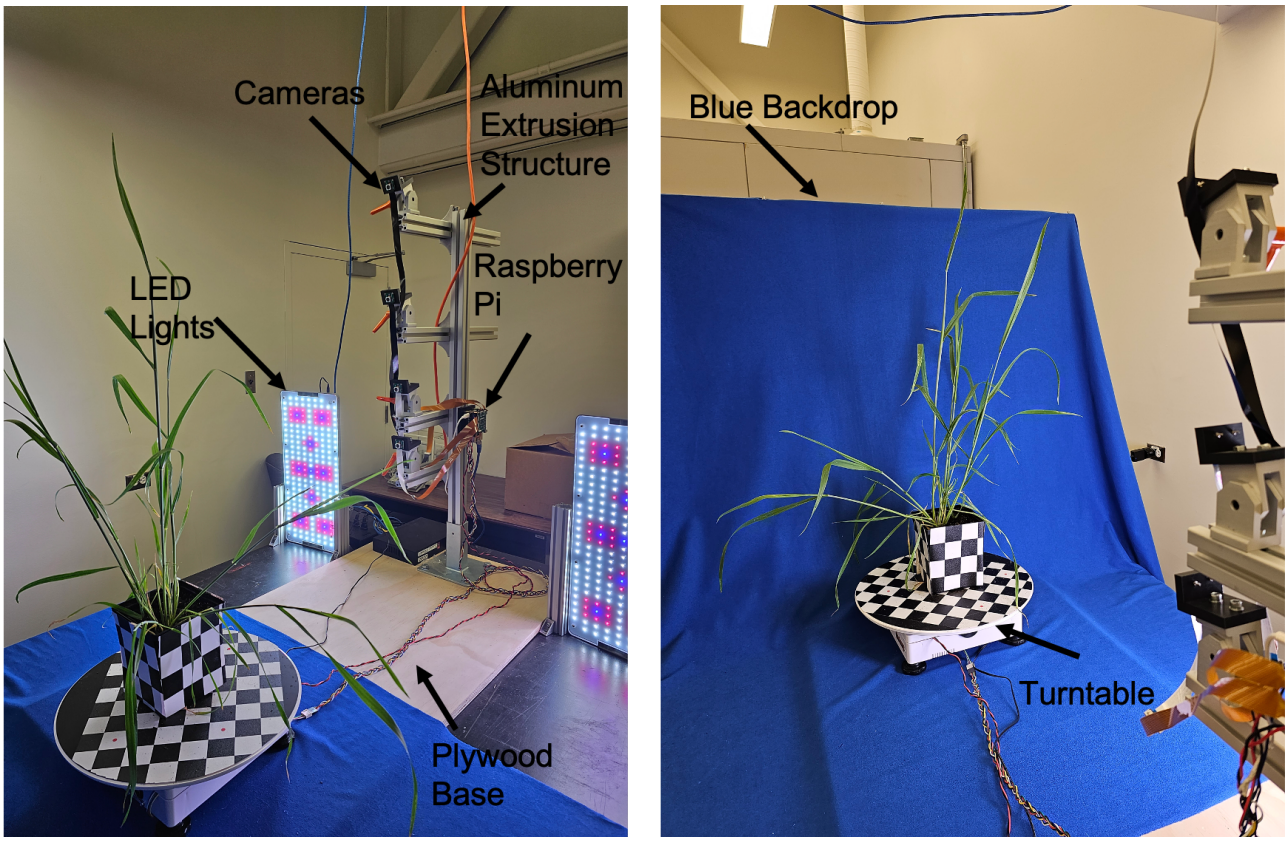

(a) Back view (b) Front view

Figure 3.7: A view of the fully assembled photogrammetry rig, illustrating both the front and back perspectives. Key components include two LED lights placed to ensure uniform illumination across the subject. A matte blue backdrop is used to provide a neutral, reflection-free background, enhancing image clarity. Central to the rig is the Raspberry Pi and camera kit, mounted for high-quality image capture. Completing the setup is a motorized turntable, enabling a 360-degree rotation of the object, which is crucial for capturing images from all angles.

At the core of the rig is the Raspberry Pi 4 4GB single-board computer, coupled with the 64MP Autofocus Synchronized Quad-Camera Kit, which can capture detailed images with an autofocus feature. The Ortery PhotoCapture 360M, a motorized turntable controlled by a user-programmable software, provides a rotationally stable platform for imaging objects. Additional components include the Adafruit DC and Stepper Motor HAT, a 32GB microSD card for primary

data storage, a 5V 3A USB-C power supply for consistent operation, and an 18mm x 24-inch x 48-inch plywood base for structural foundation. A featureless blue background of matte fabric ensures a backdrop, highlighting the subject and enhancing the quality of the captured images. Table 3.1 details the costs of the main components necessary for assembling the photogrammetry rig, encompassing each part from the featureless background and lighting setup to the aluminum extrusion structure, the turntable, Raspberry Pi and camera kit. The total cost for assembling the rig, as outlined, amounts to approximately $2,642.14, which could be further reduced by selecting a more affordable turntable option.

Part	**Brand**	**Model**	**Price**	**Specs**	**Description**
Embedded system	Raspberry Pi	Raspberry Pi 4 Model B	$249.99	Quad-core Cortex-A72, 4GB RAM, 40 pin GPIO header, 2-lane MIPI CSI camera port	Compact, low-cost computer board ideal for embedded applications
4 RGB Cameras	Arducam	64MP Autofocus Quad-Camera Kit	$199	WiFi/Bluetooth, Res: 4056 x 3040 px, FOV diagonal: 84 °	High-resolution, auto-focus RGB cameras for detailed image capture
Featureless Background	Rose Brand	62" Poly Pro	$15.20 /yard	Fabric, Chroma Key Blue	Wrinkle-resistant fabric providing a uniform backdrop for imaging
Stepper Motor	Adafruit	Stepper Motor HAT - mini kit	$27.95	TB6612 chipset, 4.5VDC to 13.5VDC, unipolar or bipolar	Motor HAT (Hardware Attached on Top) designed for precise motion control with the Raspberry Pi
Turntable	Ortery	PhotoCapture 360M	$1,200	28.956 and 39.878 cm diameter platforms,	Software-controlled rotary table for consistent image capture angles
Aluminum Extrusion	Misumi		$950	aluminum alloy, Square shape, 40mm main frame and arms size, four side slots	Sturdy frame with stationary mounts, angle brackets, nuts and screws

Table 3.1: Breakdown of the main components and associated costs for the photogrammetry rig setup.

It is essential to position the turntable at the end of the base and ensure it rotates smoothly without any wobbles. The Raspberry Pi is mounted on the aluminum extrusion structure of the rig in a location that allows easy access for necessary adjustments or connections. The camera kit, which consists of 4 cameras, is positioned on different viewpoints on aluminum extrusion arms attached to the main structure of the rig. Each camera is aligned, ensuring an unobstructed view of the subject. Special brackets hold the cameras in place, and their positioning is adjusted to capture the subject from different angles, maximizing image coverage. The layout is designed to maximize space utilization and functionality while prioritizing user-friendliness. This section has outlined the construction of the rig and critical attributes. Subsequent sections will delve into the specific hardware components of the photogrammetry rig.

3.3.1 Raspberry Pi and Camera Kit

The Raspberry Pi was selected as the primary control and data acquisition system due to its cost-effectiveness and modularity [100]. While compact in design, the Raspberry Pi's computational power is remarkably robust, making it suitable for handling imaging datasets. Its quad-core ARM Cortex-A72 processor ensures efficient image capture and device control, while the added 4GB LPDDR4 RAM handles tasks like managing extensive datasets. Beyond its raw processing capabilities, the Raspberry Pi offers a user-friendly interface and a vast community of developers and enthusiasts. The general-purpose input/output (GPIO) pins on the Raspberry Pi, which are programmatically controlled through coding scripts, serve as a versatile hub for hardware interaction and control, acting as digital signal pins on the integrated circuit that can function as inputs, outputs, or both, controllable by software. They provide a direct interface with the System on Chip (SoC), facilitating communication with various peripherals, from sensors and motors to specialized add-ons. Configurable as inputs or outputs, these pins allow the Raspberry Pi to read sensors, control motors, actuate relays, and communicate with other systems. They also support communication protocols like I2C, SPI, and UART for intricate hardware interactions. The Raspberry Pi also includes built-in Wi-Fi, Ethernet, and USB capabilities, allowing reliable connectivity and streamlining data transfer significantly when offloading captured images to a server for further processing.

The initial prototype of the photogrammetry rig utilized the Raspberry Pi High-Quality Camera for image data capture, chosen for its high resolution and compatibility with the Raspberry Pi system. The Raspberry Pi High-Quality Camera features a 12.3-megapixel Sony IMX477 sensor, capable of delivering sharp images. Its adjustable focus lens and support for interchangeable lenses offered versatility in capturing images under various conditions. Figure 3.8(a) illustrates the components of the early prototype of our photogrammetry rig, showing the integration of the Raspberry Pi High-Quality Camera with the Arducam multi-camera adapter [101] and the Raspberry Pi. Figure 3.8(b) shows the Arducam multi-camera adapter, enabling up to four cameras to

a single Raspberry Pi for simultaneous image capture. Details on the experimental results and the conceptual validation achieved with this early prototype of the rig are shown in Section 3.4.

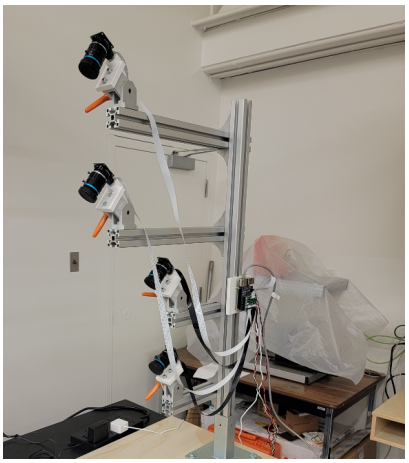

(a) The Raspberry Pi High-Quality Camera connected to the Arducam multi-camera adapter and the photogrammetry rig.

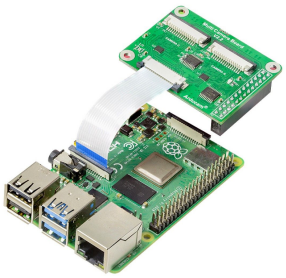

(b) Arducam multi-camera adapter supporting four camera connections.

Figure 3.8: (a) View of the hardware components of the initial photogrammetry rig prototype with the Raspberry Pi High-Quality Camera. (b) View the Arducam multi-camera adapter which allows for the integration of multiple cameras into the Raspberry Pi system.

However, to further enhance the imaging capabilities of our rig, we decided to use the Arducam 64MP Autofocus Quad-Camera Kit HAT, as shown in Figure 3.9. This upgrade improved the capacity of the system to capture high-resolution, detailed images. The Arducam kit includes four 64MP cameras, each equipped with autofocus functionality, dramatically expanding the imaging potential of the rig as illustrated in Figure 3.9(a). The autofocus feature, in particular, adds a layer of convenience and precision by automatically adjusting focus to ensure sharp images across various distances and conditions. The integration of the camera kit and mounts with the Raspberry Pi, as depicted in Figure 3.9(b), shows how these components connect to the aluminum extrusion structure. The Camarray technology facilitates communication with the CSI port via a 15-22-pin camera cable, maintaining the modularity of the rig and ease of use. Each camera module is mounted on adjustable angle brackets, allowing for the precise positioning of the cameras at various angles. This feature, combined with the 10x digital zoom, wide field of vision, and the F1.8 aperture, significantly enhances the capability of the rig to images from multiple perspectives.

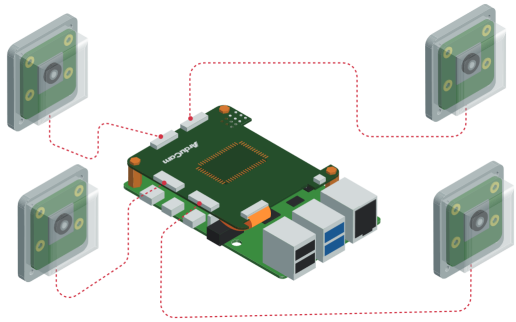

(a) Arducam 64MP Autofocus Quad-Camera kits including four cameras. (Image taken from Ref. [102].)

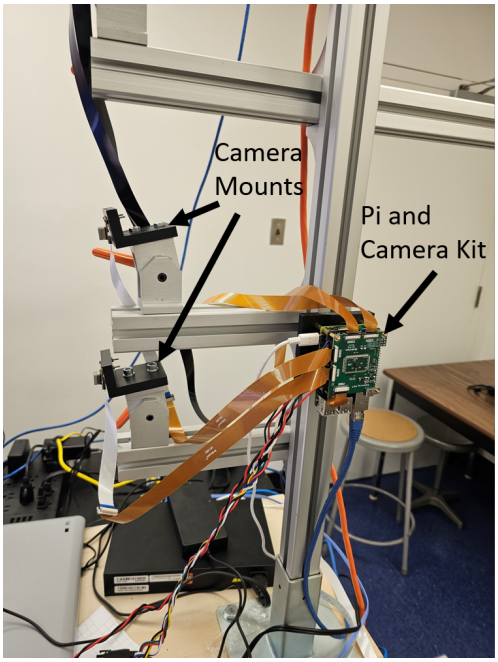

(b) View of the camera kit connected to the Raspberry Pi, along with the camera mounts.

Figure 3.9: (a) Hardware components of the Arducam 64MP Autofocus Quad-Camera Kit, along with the Raspberry Pi, where all four cameras connect to the kit. (b) Close-up view of the assembled Raspberry Pi, camera kit, and camera mounts, attached to the aluminum extrusion structure of the photogrammetry rig.

3.3.2 Turntable

The imaging system uses the PhotoCapture 360 turntable, a commercial rotary table designed to capture multi-angled images from various viewpoints [103]. With dimensions of 15.7 x 15.7 x 4.1 inches and platforms of 11.4" and 15.7" diameters, this turntable can accommodate various object sizes and can bear loads up to 25 lbs. The motorized rotation and advanced control mechanisms of the turntable allow accurate rotational settings to achieve consistent 360-degree imaging. The turntable has a rotational precision of ± 1 degree, ensuring precise positioning for capturing images from specific viewpoints.

Figure 3.10 shows the turntable used in the imaging setup, which features a black and white checkered pattern placed on the surface. The checkerboard design enhances the visual alignment

during image capture and aids in the 3D reconstruction. The contrasting squares of the pattern provide reference points that allow for a more precise calculation of the spatial distance and depth in the images. This pattern is especially beneficial for SfM, as it facilitates accurate feature detection and matching across multiple images, leading to more accurate and detailed 3D point clouds.

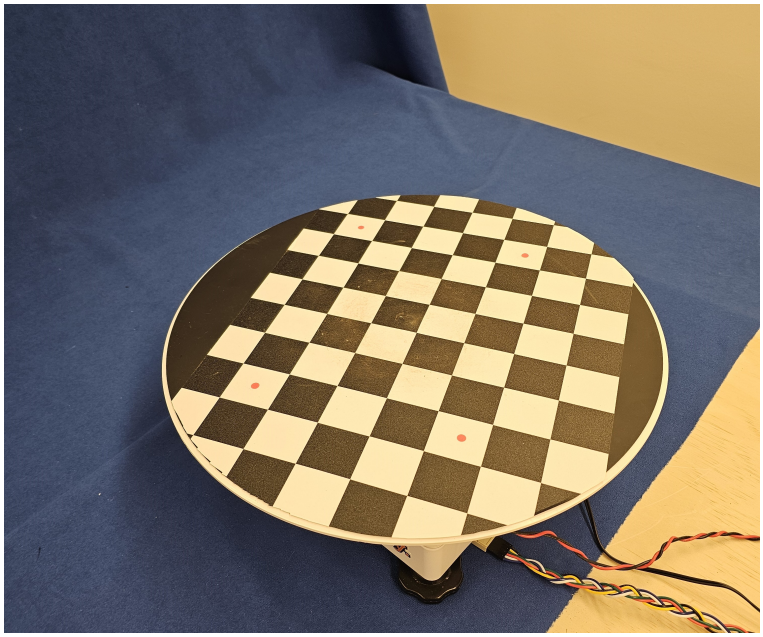

Figure 3.10: The turntable in our imaging setup, is attached with a checkered pattern on its surface, designed to improve both visual alignment during image capture and the efficacy of the 3D reconstruction. This pattern provides reference points for accurate spatial measurement and depth perception, aiding the SfM algorithm in feature detection and matching.

The PhotoCapture 360 Turntable is designed with a flat, horizontal platform anchored centrally, enabling 360-degree rotations. The motorized feature of the turntable is central to its operation, offering precise control over rotation dynamics. This control is managed through software, ensuring uniform movement and precise image alignment. An essential part of the turntable is its capacity to support substantial weight, maintaining a uniform and stable rotation throughout the imaging sequence. The turntable includes peripheral rollers that evenly distribute the load, mitigating any oscillation and ensuring the stability of the subject. Considering that the primary subjects being imaged are plants, known for their susceptibility to movement, the stability of the turntable was essential. The slightest imbalance could manifest as movement, rendering the imaging less effective. The selection of this turntable was driven by the necessity to establish a stable imaging

environment, ensuring consistency and precision in capturing images from various angles. For the project, we modified the PhotoCapture 360 Turntable to interface with a Raspberry Pi, as shown in Figure 3.11, by re-configuring its internal wiring and utilizing the Adafruit DC and Stepper Motor HAT [104].

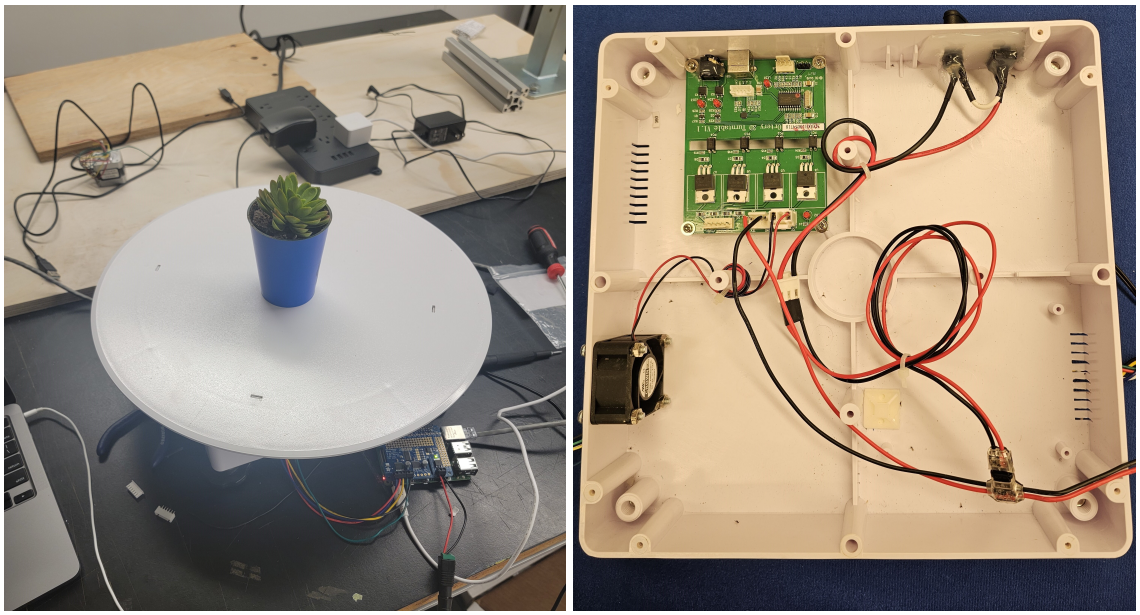

(a) Interfacing with the Raspberry Pi and the turntable.

(b) Internal components of the turntable.

Figure 3.11: The modified turntable shows the rewired internal components for direct interfacing with the Raspberry Pi. The Adafruit DC and Stepper Motor HAT is used to interface with the stepper motor inside the turntable and the Raspberry Pi. This image illustrates the technical customization undertaken to adapt the functionality of the turntable, allowing control through an open-source stepper motor library.

The Adafruit DC and Stepper Motor HAT is adept at controlling up to four DC or two stepper motors, utilizing pulse-width modulation (PWM) for fine-tuning motor speeds. Its compatibility with the standardized 2x20 connection port of Raspberry Pi models allows the HAT to overcome the limited PWM output issue. This is achieved by using a dedicated PWM driver chip that utilizes I2C communication. The efficient design of the chip requires only two GPIO pins (SDA and SCL) to manage multiple motors, thus conserving valuable resources and enhancing the overall system efficiency. Stackable connectors are provided in scenarios where the system complexity calls for multiple HATs to enable a consolidated and efficient setup. This modularity and expandability

proved instrumental for stacking the Arducam 64MP Autofocus Quad-Camera Kit on top of the Adafruit DC and Stepper Motor HAT. Figure 3.12 illustrates the configuration of the imaging system with the Arducam 64MP Autofocus Quad-Camera Kit stacked on top of the Adafruit DC and Stepper Motor HAT, which is mounted directly on the Raspberry Pi. The entire setup is secured on a 3D-printed mount attached to the aluminum extrusion frame.

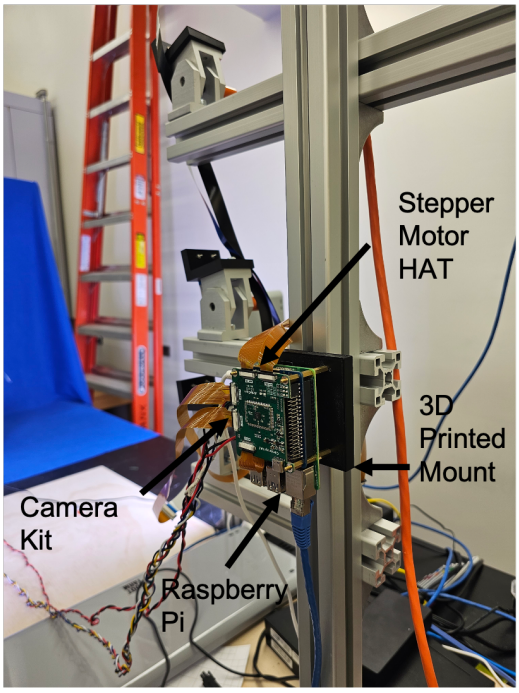

Figure 3.12: The imaging system configuration showing the Arducam 64MP Autofocus Quad-Camera Kit stacked on top of the Adafruit DC and Stepper Motor HAT, which is mounted on the Raspberry Pi. The assembly is secured on a 3D-printed bracket affixed to the aluminum extrusion frame of the photogrammetry rig.

The HAT powers the motors using TB6612 MOSFET drivers, which provide a stable 1.2A current per channel and support peak currents up to 3A for short periods. Such robust power handling is essential for consistent motor performance across various demands. Protective elements, such as built-in flyback diodes, are crucial for safeguarding the system against voltage irregularities and prolonging its service life. A polarity protection FET on the power pins also mitigates risks associated with electrical misconnections. Delivered fully assembled and pre-tested, the HAT arrives with all essential components, such as pre-soldered terminal blocks and a 2x20 pin lifter header, facilitating quick integration with the Raspberry Pi. The Raspberry Pi powers and controls the

stepper motor via the connected HAT. A Python script runs on the Pi, orchestrating the movements of the stepper motor with high precision. This script enables the Raspberry Pi to dictate the speed, direction, and number of steps the motor takes, allowing for control over the mechanical aspects of the rig.

3.3.3 Aluminum Extrusion Structure

Figure 3.13(a) shows the T-slot aluminum extrusion structure central to the imaging system. This schematic highlights the design, facilitating straightforward assembly and disassembly. It features each movable mount with its corresponding lever aligned along the T-slot arms. This design details underscore the integration of user-friendly operation and portability with the rig, ensuring precise camera adjustments within a robust and dependable framework. Figure 3.13(b) shows the model of our imaging system, capturing its early development. This phase of the project was characterized by a focus on establishing a foundational design that would effectively meet the basic requirements of the imaging process.

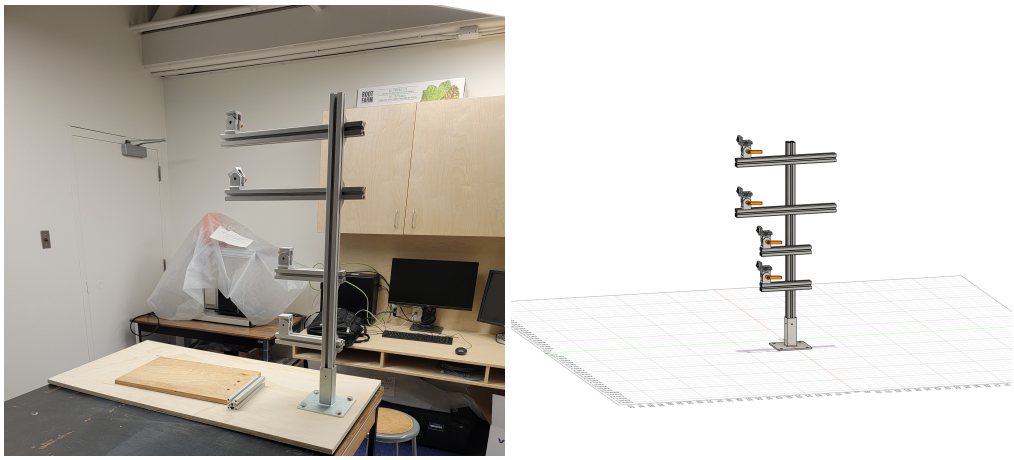

(a) View of the T-slot aluminum extrusion structure

(b) The general design of the imaging system

Figure 3.13: Diagram of the T-slot aluminum extrusion structure of the 3D imaging system, showing the modular design that simplifies assembly and disassembly. Key features include adjustable camera mounts with levers for precise alignment.

The framework of the imaging system is constructed from T-slot aluminum extrusions chosen

for their modularity, lightweight properties, and superior strength-to-weight ratio. These extrusions are precisely cut and assembled to form a sturdy frame that securely supports four cameras. The adaptability of the camera mounts, facilitated by brackets and fasteners that move smoothly within the T-slot channels, allows for easy and dynamic repositioning. Adjustments are made by simply loosening and tightening these fasteners, enabling the camera mounts to slide along the arms of the structure to the required positions. The main structural frame, extending 1 meter in length, is designed with four arms dedicated to holding a camera. The arms, measuring 500 cm and 250 cm in length, are configured to support two cameras at the upper and lower positions respectively. This arrangement places the cameras in an arc, enabling them to capture a hemispherical view of the subject in a single rotation.

The modularity of the T-slot design is key to the customizable and scalable features of the imaging system. It allows straightforward modifications, such as adding cameras or adjusting mounts to suit different subjects, enhancing the versatility of the system. The central placement of the Raspberry Pi and camera kit further demonstrates the ease of integration. Ergonomically designed levers on the mounts enable manual repositioning of cameras for precise alignment, as shown in Figure 3.14. Using aluminum contributes to the stability and vibration damping of the imaging system, akin to a tripod, thus improving image clarity.

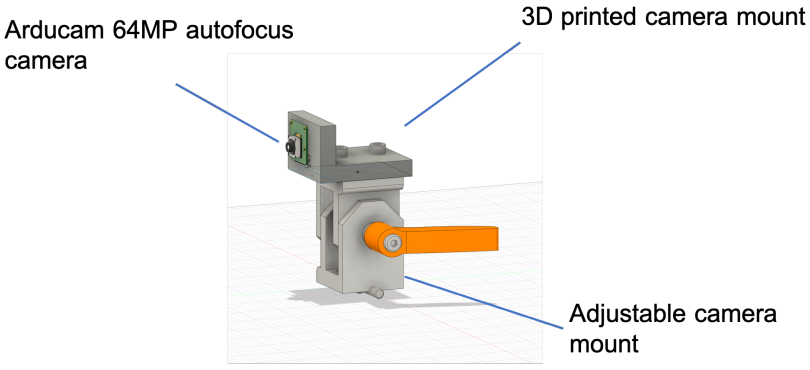

Figure 3.14: View of the camera mount system integrated into the aluminum extrusion structure, showing the camera affixed to the 3D printed mount, which is screwed onto the adaptable brackets. These mounts, characterized by their sliding brackets and fasteners, facilitate movement within the T-slot, allowing quick adjustments. Levers enhance the flexibility of the system, positioning the camera at the ideal shooting angle.

3.3.4 Featureless Background and Lighting Setup

The background in a photogrammetry setup is critical to the success of the imaging process. A featureless and neutral backdrop is essential for eliminating visual noise, ensuring that the focus of the camera and the algorithms are concentrated on the subject. This singular focus is crucial for accurately identifying points, a core aspect of 3D modeling. Patterns or distinct colors in the background can lead to misinterpretations of the subject, introducing inaccuracies into the 3D reconstruction. For our system, we chose a blue matte fabric from Poly Pro, valued for its uniformity and wrinkle-resistant qualities, ensuring a consistently smooth and distraction-free surface for imaging. The chosen material should be non-reflective and matte, commonly in neutral tones, to prevent interference with the imaging process. It must be large enough to surround the subject, with its alignment parallel to the imaging plane, which is essential for avoiding perspective distortions and simplifying the post-processing workflow.

Creating a custom lighting setup, often incorporating multiple diffused lighting sources, is a critical aspect of photogrammetry. This is designed to effectively illuminate the object without casting unwanted shadows or highlights on the backdrop, maintaining the featureless nature of the background and ensuring that it complements the imaging of the object without introducing any distortions or artifacts. Lighting is fundamental in photogrammetry and instrumental in determining the quality of the final model. Good lighting conditions are critical in accurately capturing the texture and geometry of the model and minimizing potential errors during scanning. Adequate lighting ensures that the subtle nuances of the object are clearly defined.

Using portable lights can ensure uniformity and prevent issues like tiling and blurring. This consistency helps avoid the creation of unintended artifacts, and the flexibility to correct light temperature post-processing allows for greater control over the final image quality, ensuring optimal conditions for photogrammetry. Effectively managing shadows, refraction, and reflections is essential in photogrammetry. Balanced lighting minimizes distortions in the 3D model, with strategic placement and intensity of lights being vital for capturing the actual features of the object. Achiev-

ing a balance in lighting is, therefore, crucial for accurately capturing the features of the object and preventing any distortions or inaccuracies in the final model. Two LED lights were used and pointed towards the plant subjects. This setup ensures the subject is well-illuminated from multiple angles and minimizes shadows that could obscure details or introduce inaccuracies. As shown in Figure 3.15 featuring the blue Poly Pro matte fabric backdrop alongside the LED lighting to ensure uniform illumination of the subject, a combination for minimizing visual noise and optimizing focus for accurate 3D modeling.

Figure 3.15: The choice of a blue, non-reflective, and uniform backdrop ensures minimal visual noise and optimal focus on the subject. The use of two LED lights, positioned to illuminate the plant subjects, ensures uniform lighting across the subject, minimizing shadows and enhancing the accuracy of images.

3.4 Initial Results and Proof of Concept of the Photogrammetry Rig

This section provides an overview of the initial findings and validation of the photogrammetry rig designed for plant imaging and analysis. In Section 3.4.1, we explain the methodologies for creating the datasets and implementing the photogrammetry rig for imaging. Following this, Section 3.4.2 describes the specifics of the point cloud data preprocessing. Section 3.4.3 shows the results from imaging with the photogrammetry rig, including the validation of 3D reconstruction for plant height measurements of soybean using linear regression analysis and error calculations, as well as the assessment of canopy volume measurements with the convex hull method for both plant species.

3.4.1 Experimental Setup and Methodology

This experiment aims to demonstrate the effectiveness of the photogrammetry rig, presenting initial results and validating its capabilities in capturing and analyzing plant height and canopy volume through comprehensive methodologies, data preprocessing, and analysis of imaging results. The experimental setup involved growing one pot of each lettuce and soybean under controlled conditions to ensure consistency in data collection. Over five weeks, the plants were subjected to uniform environmental factors, including lighting, temperature, and watering schedules, to minimize external variability in growth patterns. Watering was carefully regulated, with each plant receiving water every second day. This consistent hydration schedule was crucial for maintaining plant health and uniform growth. The plants were grown in a growth chamber developed by Conviron at the University of Winnipeg, where the temperature was controlled, with daytime temperatures set to 25 °C and nighttime temperatures to 18 °C. The relative humidity was maintained at 60%, creating an optimal growing environment.

Imaging of the plants was conducted once a week throughout the five weeks. This regular imaging schedule was essential for capturing the dynamic growth process and allowed for analyzing developmental changes over time. Images were taken with the photogrammetry rig and processed for 3D reconstruction separately. The plants were taken out of the growth chamber, as shown in Figure 3.16(a), imaged for an estimated 25 minutes and returned to the chamber after imaging. Figure 3.16(b) shows the first prototype of our photogrammetry rig, showing the initial setup used for capturing plant growth data with the high-quality camera module for the Raspberry Pi. Manual adjustments were made to the cameras to fine-tune focus and position, ensuring the images are high quality and accurate in the image capture.

(a) Various plants growning in the growth chamber

(b) First prototype of the photogrammetry rig

Figure 3.16: For this experiment, plants are cultivated in the growth chamber, placed on the turntable, and imaged by the photogrammetry rig. For the purposes of this experiment, only one pot of lettuce and soybean are imaged.

Table 3.2 outlines the configuration of the photogrammetry rig utilized in this experiment and details the settings essential for capturing high-quality images. These settings include the turntable angle, set at 10 degrees to ensure a decent overlap between images, and the total number of images 148, indicating the depth of data collection. The camera resolution is specified as 4084 x 3051. Additionally, camera settings include the focal length at 16 mm, aperture setting at f/5.6, and ISO setting at ISO-143. The distance between the plant and rig was 1-2 meters to ensure the plant was entirely in the shot and the background remained consistent. The total imaging time for each plant

was recorded as 25 minutes, which is the time needed to get a full 360-degree view of the plant.

Setting	Value
Turntable Angle	10°
Total Images	148
Camera Resolution	4084 x 3051
Focal Length	16 mm
Aperture Setting	f/5.6
ISO Setting	ISO-143
Distance to Subject	1-2 m
Total Imaging Time	25 Minutes
Total Size on Disk	297 MB
Image Capture Delay	6 seconds

Table 3.2: This table details the specific settings and configurations of the photogrammetry rig used. It includes parameters such as the turntable angle, camera resolution, focal length, aperture setting, ISO setting, and distance to subject.

We utilized the default reconstruction settings of COLMAP but later in the project, Python scripts were developed to interface with COLMAP, significantly streamlining the transition from 2D imaging to 3D reconstruction, thereby enhancing the ease and automation of the entire process (more details in section 4.3). A desktop computer was utilized for the 3D point cloud reconstructions, equipped with a 12-core/24-thread 3.5 GHz CPU, 32 GB of 3200 MHz RAM, and an NVIDIA GeForce RTX 3060 GPU. The complete reconstruction of a dense point cloud for each plant took approximately 120 minutes.

3.4.2 Dataset Preprocessing

Point clouds captured from the soybean and lettuce plants were subjected to a series of processing steps to refine and prepare them for assessment. The initial step in this reprocessing involved opening the point cloud data in MeshLab [105], an open-source software known for its effectiveness in handling 3D data. Point clouds were scaled (using the diameter of the turntable), denoised based on color (removing all but the green/brown points), aligned to the positive z-axis, and translated to the origin such that the "ground" of the point cloud is parallel to the X–Y plane, and any

remaining non-plant points removed manually in Meshlab.

Figure 3.17 shows the 3D point cloud pre-processing stages, using a soybean plant as an example. The process commences with the initial raw point cloud, captured by the photogrammetry rig and depicted in 3.17(a), which includes the plant, the pot, the turntable, and some noise. Following this, as shown in 3.17(b), is a calibration step where the diameter of the turntable is measured and scaled with the actual diameter of the turntable. This measurement is essential for establishing an accurate scale reference within the point cloud data. Subsequent processing stages involve adjustments to the data, as seen in 3.17(c), where the point cloud is translated and rotated to align correctly with the origin and the positive z-axis. Figure 3.17(d) shows a cleaned and refined final point cloud of the soybean plant.

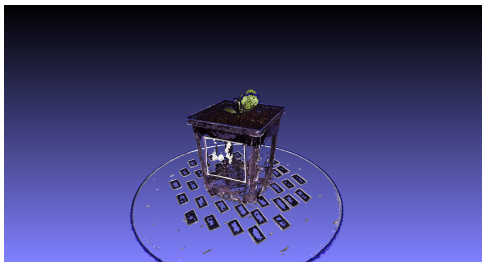

(a) Initial 3D point cloud data of a soybean plant, showing the structure of the plant before any processing.

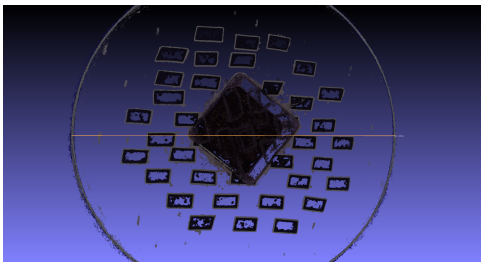

(b) Calibration stage showing the measurement of the turntable diameter, crucial for accurate scale setting in the point cloud data.

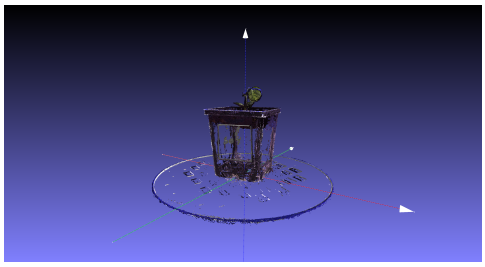

(c) Processed 3D point cloud showing translation and rotation to the origin, illustrating the alignment of the normal vector to the positive z-axis.

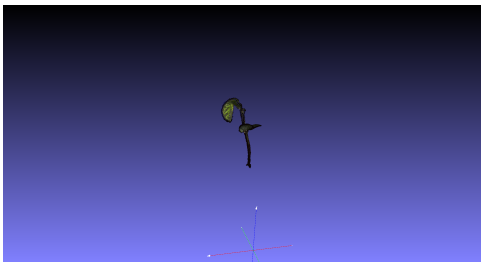

(d) Final cleaned 3D point cloud of the soybean plant.

Figure 3.17: Example of the pre-processing workflow for the 3D point cloud data using soybean scans. The process begins with translating the point cloud to the origin, removing points associated with the turntable and plant pot, and aligning it along the positive z-axis. The point clouds are on the positive z-axis and positioned at the origin of the coordinate system.

3.4.3 Results and Discussion

Soybean Plant Height

Plant height measurements were only done with soybean because lettuce grows more flat and outward, making it challenging to manually measure plant height accurately. The measured plant height of soybean from the reconstructed point cloud model was validated with the actual measured values using linear regression analysis to prove the system's accuracy. The Root Mean Squared Error (RMSE) and Mean Absolute Percentage Error (MAPE) were used to quantify the model's predictive accuracy. The RMSE measures the average magnitude of the errors, giving higher weight to more significant errors. MAPE expresses the average absolute error as a percentage of actual values, offering a scale-independent accuracy measure. These calculations were performed using the statistical functions available in the SciPy library [106]. Researchers note that the acceptable range for measured morphological traits in phenotyping is 5–10%. This range is deemed acceptable as it aligns with the error magnitude typically found in manual measurements. It is sufficiently low to differentiate variations in relevant traits across imaging dates during development [68]. Equation 3.4 defines the RMSE for plant height as

$$\text{RMSE}_{\text{plant height}} = \sqrt{\frac{1}{n}\sum_{i=1}^{n}(\hat{h}_i - h_i)^2}, \tag{3.4}$$

where $\hat{h}_i$ is the measured plant height derived from the 3D point cloud generated by the photogrammetry rig, h_i is the actual plant height, and n is the number of plants or measurements taken. Equation 3.5 defines the MAPE for plant height as

$$\text{MAPE} = \frac{1}{n}\sum_{i=1}^{n}\left|\frac{\hat{h}_i - h_i}{h_i}\right| \times 100\%, \tag{3.5}$$

where $\hat{h}_i$ represents the predicted or measured plant height from the photogrammetry data, h_i is the

actual, observed plant height obtained through direct measurement, and n is the number of plants or measurements.

In this study, plant height was a primary metric of interest. Plant height was quantified by measuring from the base of the stem to the apex of the canopy. This measurement was computed using the photogrammetric data by calculating the difference between the maximum (Z_{max}) and minimum (Z_{min}) Z-axis values in the 3D point cloud, as demonstrated in Equation 3.6

$$H = Z_{max} - Z_{min}, \tag{3.6}$$

this is visually shown in Figure 3.18, which illustrates the method for calculating plant height, highlighting the importance of Z_{max} and Z_{min} in the process.

Figure 3.18: Diagram illustrating the method of measuring plant height, with Z_{max} representing the topmost point and Z_{min} indicating the base. This aids in visualizing the procedure outlined in Equation 3.6 for calculating plant height.

Figure 3.19(a) shows a linear regression analysis that illustrates the relationship between the 3D point cloud measurements and the manually measured plant heights, demonstrating the reliability of the photogrammetry rig. The analysis shows that height measurements from 3D reconstructions were modestly lower, by about 4%, than those from manual validation measurements. The analysis confirmed a correlation between the two sets of measurements given by $R^2 = 0.99$, indicating that the linear model with manual measurements can account for 99% of the variance in point cloud measurements. An RMSE of 0.81 and a MAPE of 10.63% further quantify the precision

and the average percentage error, respectively, illustrating a high level of accuracy in capturing plant growth despite the inherent measurement errors. Figure 3.19(b) shows the soybean plant growth over time, mapping out their development trajectory. The growth trajectory depicted a swift increase in plant height, with a height of 17 mm observed within the first week after germination. The growth rate then slowed, leading to a gradual rise in height to 242 mm by the end of the fifth-week post-germination. These figures, obtained from RMSE and MAPE analyses, measure the accuracy of the photogrammetry rig, showing its capability to track the growth dynamics of plants precisely.

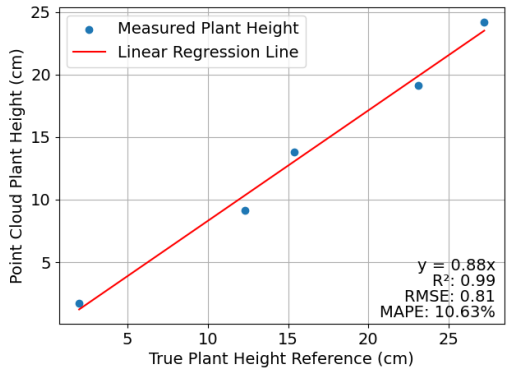

(a) Linear regression analysis of soybean plant height, illustrating the correlation between measured and predicted heights.

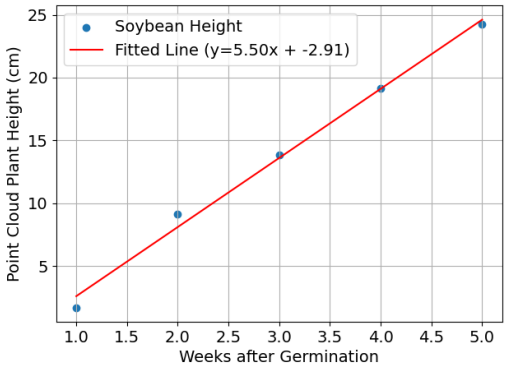

(b) Graphical representation of soybean plant height over time, shows the growth trajectory of the plants.

Figure 3.19: (a) A linear regression analysis was performed on soybean plants to validate the correlation between 3D point cloud measurements and manually measured plant heights, effectively quantifying the accuracy and reliability of 3D measurements. (b) Additionally, tracking growth trajectory of soybean over time sheds light on the dynamic patterns of plant development and shows a linear relationship, offering insights into its growth rates.

Canopy Volume of Soybean and Lettuce

The canopy volume of soybean and lettuce was determined by analyzing the convex hull derived from the 3D point cloud data. Let $P = \{p_1, p_2, \ldots, p_n\}$ be a set of points in $\mathbb{R}$. The convex hull of P, denoted as $\text{Conv}(P)$, is the smallest convex set that contains all points in P. A set C is convex if, for any two points $a, b \in C$, the line segment connecting a and b is entirely contained within C.

The convex hull $\text{Conv}(P)$ can be represented as the intersection of all convex sets containing P or as the set of all convex combinations of points in P [107, 108].

The convex hull of a set of points in $3D$ space forms a convex polyhedron. To compute the volume of this polyhedron, an effective method involves summing up the triangular pyramid (or a tetrahedron) formed by an arbitrary fixed point within the hull, O, and the triangular faces on the surface of the hull. A convenient choice for O is the centroid of the hull vertices, providing a point well within the polyhedron. The volume of each tetrahedron, created by O and a triangular face defined by points P_1, P_2, and P_3 on the hull, can be determined by

$$V_{\text{total}} = \sum_{i=1}^{m} V_{\text{tetrahedron}_i},$$

where m is the total number of triangular faces on the convex hull, and $V_{\text{tetrahedron}_i}$ is the volume of the tetrahedron formed by the i-th triangular face and the point O. The volume of each tetrahedron $V_{\text{tetrahedron}_i}$ can be calculated as

$$V_{\text{tetrahedron}_i} = \frac{1}{3} \times \text{Area}(f_i) \times \text{Height}_i.$$

Here, $\text{Area}(f_i)$ is the area of the i-th triangular face, and Height_i is the perpendicular distance from O to the plane containing the i-th triangular face. This sum calculates the total volume of the convex hull by summing the volumes of all tetrahedron. These calculations were performed using the convex hull package in the SciPy library [106].

The dynamic growth stages of lettuce plants over three weeks are illustrated in Figure 3.20. In the top row, Figures 3.20(a), 3.20(b), and 3.20(c) show the cleaned point clouds of the lettuce plants at weeks 3, 4, and 5, respectively. These images show the structural development of the plants, highlighting the progressive growth in size and architectural complexity. In the bottom row, Figures 3.20(d), 3.20(e), and 3.20(f) illustrate the convex hull calculations at weeks 3, 4, and 5, respectively.

(a) Week 3 (b) Week 4 (c) Week 5

(d) Canopy Volume Week 3 (e) Canopy Volume Week 4 (f) Canopy Volume Week 5

Figure 3.20: The top row shows the cleaned point clouds for weeks 3, 4, and 5, illustrating the structural development of the plants. The bottom row illustrates the same point clouds with convex hull calculations, highlighting the changes in canopy volume over time. These visual representations help to quantify the growth patterns of the lettuce, demonstrating the effectiveness of 3D modeling in tracking and analyzing temporal changes in plant morphology.

The dynamic growth and development of the soybean plants over three weeks are shown in Figure 3.21. In the top row, Figure 3.21(a), 3.21(b), and 3.21(c), display the cleaned point clouds of the soybean plants at weeks 3, 4, and 5 respectively. These images provide a detailed view of the structural development and architecture of the plant, highlighting the gradual increase in size and complexity. This visualization not only aids in understanding the phenotypic changes over time but also underscores the precision of the photogrammetry rig in capturing intricate details. In the bottom row, Figures 3.21(d), 3.21(e), and 3.21(f) illustrate the convex hull calculations for these corresponding growth periods, offering quantitative insights into the volumetric expansion of the canopy as the plants mature.

Figure 3.22(a) illustrates the canopy volume of the soybean plant, highlighting an exponential growth pattern indicative of the rapid growth of the plants. The canopy volume increases from 0.97 cm^3 one week post-germination to 1007.1 cm^3 after five weeks. Similarly, Figure 3.22(b) shows the growth trajectory of lettuce, with the exponential trend emphasizing the increase in canopy volume. The lettuce canopy volume increased from 0.54 cm^3 one week post-germination to 1307 cm^3 by the fifth week. An exponential growth curve was fitted to both data sets, illustrating the

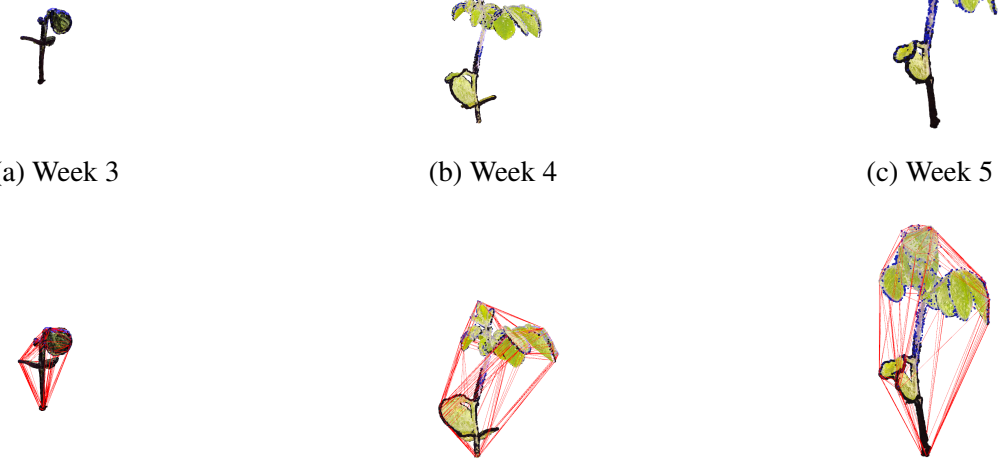

(a) Week 3 (b) Week 4 (c) Week 5

(d) Canopy Volume Week 3 (e) Canopy Volume Week 4 (f) Canopy Volume Week 5

Figure 3.21: The top row shows the cleaned point clouds for weeks 3, 4, and 5, illustrating the structural development of the plants. The bottom row presents the same point clouds with convex hull calculations, highlighting the changes in canopy volume over time.

rapid expansion in canopy volume for soybean and lettuce plants within the initial five weeks post-germination. These observations provide quantitative results of the exponential growth curves characteristic of these developmental stages of the plant. This study aimed to demonstrate the effectiveness of the photogrammetry rig in capturing and analyzing the canopy volume of lettuce and soybean plants, emphasizing its potential to measure plant growth and development.

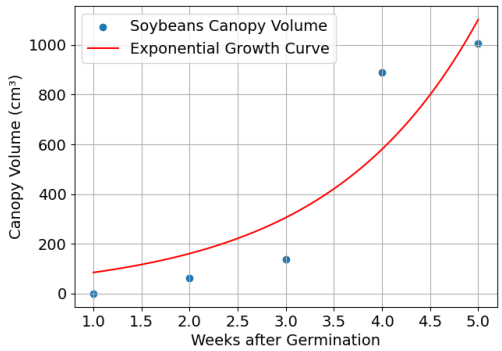

(a) Graph depicting the canopy volume growth of a soybean plant over time. The plot illustrates an exponential increase in canopy volume.

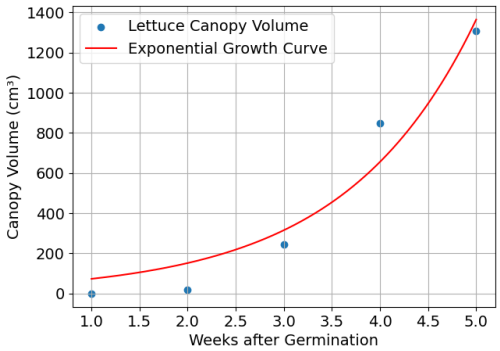

(b) The canopy volume growth of a lettuce plant. The exponential trend observed signifies the growth of the plant.

Figure 3.22: Canopy volume growth in lettuce and soybean, as captured by a photogrammetry rig. Each figure visually represents the exponential growth pattern in canopy volume, reflecting the dynamic nature of lettuce and soybean development.

4. Software Implementation of the Photogrammetry Rig

This chapter outlines the technical framework and operational processes involved in the software deployment of the photogrammetry rig. Section 4.1 outlines the software framework developed to operate the photogrammetry rig. In Section 4.2, we discuss the structured approach and methodologies adopted for capturing images and generating datasets for 3D reconstruction. Section 4.3 outlines the process of integrating COLMAP, leveraging its capabilities to facilitate 3D reconstruction within the imaging pipeline. Section 4.4 details the software implementation on the 3D point clouds, focusing on pre-processing the 3D data and preparing the data for 3D plant phenotyping.

4.1 Photogrammetry Rig Control Script

The control software for the rig is developed to specifically address the requirements of the imaging system. A Python script executes on the client side, utilizing a Graphical User Interface (GUI) application to control the photogrammetry rig through the Tkinter library. This GUI allows users to configure settings, initiate the image capture process, and inspect images. Integrated with SSH (Secure Shell) and SFTP (SSH File Transfer Protocol), the GUI ensures secure and efficient communication with the Raspberry Pi. Figure 4.1 shows the GUI application, highlighting its role in facilitating the user management of the imaging process including camera options, turntable adjustments, plant labeling, reviewing captured images and initiating the imaging sequence. The script uses the Python package Paramiko and the socket library for managing remote commu-

nications over the local network. It initializes SSH and SFTP clients, securely connects to the Raspberry Pi using its IP, username, and password by adding its host key.

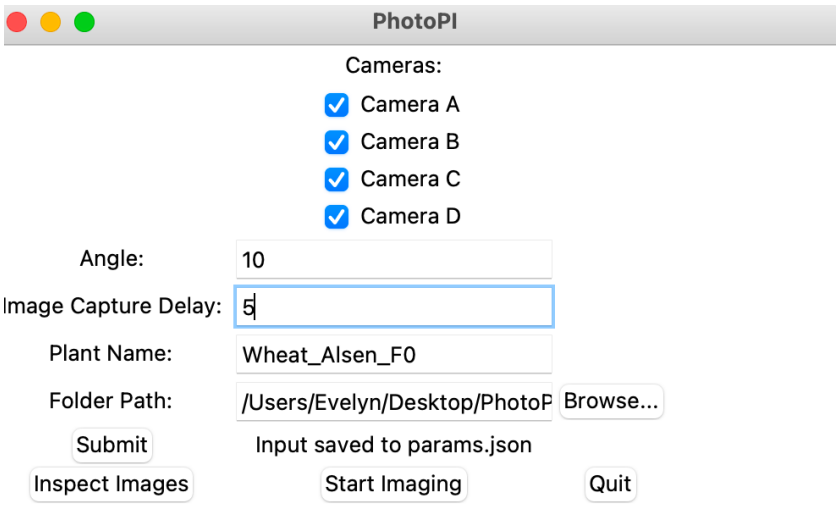

Figure 4.1: The GUI of the photogrammetry rig, created using the python package Tkinter, allows users to manage and control various aspects of the imaging process, such as camera and turntable settings, plant labeling, and image capture. It also provides functionalities for inspecting captured images and commencing the full imaging sequence.

The Photogrammetry Rig Control script, shown in Algorithm 1, outlines the pseudo-code for controlling the photogrammetry rig via a software interface. The script initiates by defining the **get_ip_address()** function, designed to ascertain the local IP address of the user on the client side. This is achieved by establishing a socket connection to Google's public DNS server at 8.8.8.8 using port 80, a method used to determine the external-facing IP address within its local network of the machine. Furthermore, the script retrieves the hostname of the user by executing the shell command 'id -un' through a subprocess, storing the result. It determines the IP address of the Raspberry Pi, which is recognized by the hostname. To facilitate image management, the script sets up several directories, with variables such as **mask_folder**, **images_folder**, and **inspect_folder** pointing to specific paths designated for various image storage types.

Within the script, the InputGUI class is defined, which establishes the framework for the user interface. This class contains several functions, including **browse_folder()**, **submit()**, **inspect()**, and **start_imaging()**. Central to the script's functionality are the inspect and image capture, which

Algorithm 1 Photogrammetry Rig Control

```
function GET_IP_ADDRESS
    Create a socket
    Connect to a public DNS server
    return the local IP address
end function
Retrieve main_hostname and main_ip_address
Define folder paths: mask_folder, images_folder, inspect_folder
Set Raspberry Pi hostname (pi_hostname) and user (user)
Resolve pi_hostname to IP (pi_ip_address)
SSH and SFTP Client Setup
    Connect to the remote device using SSH
    Create a new SFTP client
Class InputGUI
    function BROWSE_FOLDER
        Handle folder browsing
    end function
    function SUBMIT
        Handle form submission
    end function
    function INSPECT
        Handle image inspection
    end function
    function START_IMAGING
        Start the imaging process
    end function
Main Execution
    Start GUI
    Handle closing connections
```

handle capturing images using the connected cameras. The script uses libcamera, an open source camera stack and framework for Linux, to capture images on the Raspberry Pi and i2cset to switch between cameras. Following the image capture process, the script also translates the specified angle parameter into steps, directing the Raspberry Pi to rotate the stepper motor accordingly. This rotation facilitates the movement of the turntable, ensuring the subject is appropriately positioned for each set of images. The script transfers all captured images to a local machine for inspection and storage. At the end of the script, the SFTP and SSH connections to the Raspberry Pi are closed, ensuring that the network resources are correctly released. Finally, the script enters the

main loop of the Tkinter application, which keeps the GUI active and enables users to engage with the application, configure their settings, and initiate the imaging process for the next subsequent set.

The script interacts with a JSON file, to read and write configuration data, which includes the hostnames, IP addresses, and camera settings. Table 4.1 provides an overview of the parameters for the control script, highlighting the functionalities of each parameter within the system. It includes boolean variables for enabling or disabling individual cameras, specifies the rotational angle for the turntable, the time delay between image captures, and the labeling of the plants being imaged. The GUI is designed for ease of use, featuring checkboxes for camera selection, entry fields for setting angles, and buttons for essential actions like browsing folders, submitting data, and initiating the imaging process. The table lists variables holding the directory path for saving images, and network configurations. This ensures persistent storage of settings and parameters which is essential for maintaining consistency between sessions and facilitating the reuse of configurations for repetitive tasks.

Parameter	**Description**
camera_a, camera_b, camera_c, camera_d	Boolean variables to enable/disable corresponding cameras
angle	Rotation angle of the turntable in degrees
capture_delay	Time delay before taking another set of images
plant_name	Name of the plant being imaged
folder_path	Path to the folder for saving images
main_hostname, main_ip_address, pi_hostname, pi_ip_address	Network configurations for SSH and SFTP connections
SSH and SFTP Clients	Components for remote connections and file transfers
User Interface Functions	Functions for GUI interactions such as folder browsing, form submission, inspect images, image capture

Table 4.1: Key parameters for the imaging system store on the JSON file, detailing their respective functionalities. Parameters include camera controls, turntable rotation angle, delay timing, plant naming, and image storage paths. Additionally, it covers essential network configurations for SSH and SFTP connections, facilitating secure and remote system operations. These functions are crucial for the GUI, emphasizing the approach of the script in managing the operations of photogrammetry rig.

Figure 4.2 shows the whole pipeline for image capture using the photogrammetry control script. The plant of interest is placed on the turntable to begin image capture, and the user establishes a remote connection to the Raspberry Pi. In either case, one can retrieve each image directly after it has been captured or in bulk after the turntable goes through each of its positions. After completing a full rotation, the system automatically stops the turntable and the camera. The user then has the option to review the captured images on the graphical interface. If necessary, the user can repeat the image capture process after making any required adjustments. Once the user is satisfied with the image quality, the data transfer process begins. The images are automatically transferred from the Raspberry Pi to a connected computer or remote server for storage. Following the transfer, the images are ready for the next phase of the pipeline

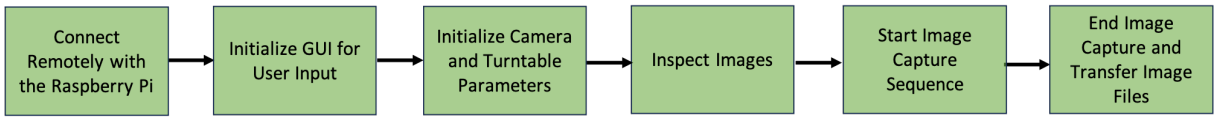

Figure 4.2: Flowchart of the photogrammetry imaging process, illustrating the steps from initial setup to the final image transfer. This includes positioning the plant on the turntable, establishing a remote connection to the Raspberry Pi, utilizing the graphical interface for image capture, and options for image retrieval.

4.2 Image Acquisition

During image capture, the system creates three distinct folders to streamline data handling and improve the workflow from the initial capture to 3D reconstruction. The first folder stores the raw images as the cameras capture them. The second, labeled ‘mask images’, contains processed images used for segmentation to separate the subject from its background. The third folder, labeled ‘inspect images’, comprises images for quality and completeness checks before imaging. These images are taken and inspected by the user to ensure the subject is position correctly. This procedure enhances data management efficiency and allows for the early detection and correction of issues like blurring or improper exposure, ensuring that only high-quality images are utilized for

3D reconstruction.

Figure 4.3 illustrates the imaging pipeline of the photogrammetry rig, detailing the process from multi-angle image capture facilitated by the Raspberry Pi, camera kit, and the turntable to the 3D reconstruction performed on a remote server. To ensure integration of this process with the data management, the system employs a naming convention for the captured images in the form of PlantType_CameraID_CaptureDate_SequenceNumber. This structured format includes the type of plant being imaged, the specific camera used for the capture (e.g., Camera A, B, C, D), the date of capture in a YYYYMMDD format, and a sequential number indicating the order in which the image was taken. For example, a file named Wheat_CameraB_20230718_001 would represent the first image of a wheat plant, captured by Camera B on July 18, 2023. This naming convention facilitates easy identification and organization of the images, aiding in efficient data retrieval and management.

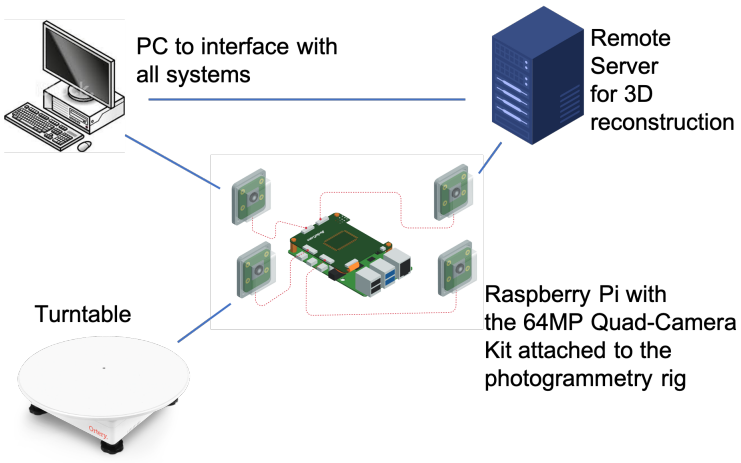

Figure 4.3: Schematic of the imaging pipeline for the photogrammetry rig, showing the integrated process from the multi-angle image capture with the Raspberry Pi and the camera kit. The setup, connected to a rotary turntable, ensures precise positioning for optimal image collection. Following image capture, images are processed and prepared by the Raspberry Pi before being sent to a remote server for 3D reconstruction.

Figure 4.4 shows an image captured by Camera D of the photogrammetry rig. This image, a close-up of a wheat plant, demonstrates the capabilities of the rig to capture the details and

textures of the plant. The image, obtained under controlled lighting conditions, ensures that all features of the wheat are distinctly visible. Capturing images from different viewpoints is essential for creating a hemispherical representation of the subject. Each camera involves photographing on both vertical and horizontal axes at every viewpoint. As shown in Figure 4.5, different perspectives on the vertical axis were captured by the four cameras on the photogrammetry rig.

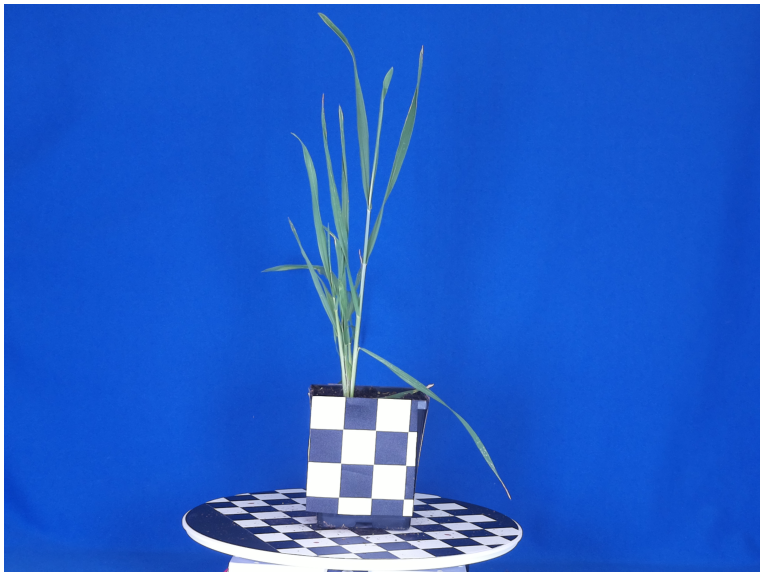

Figure 4.4: This image, captured by Camera D of the photogrammetry rig, illustrates a close-up of a wheat plant. The capture showcases the ability of the rig to accurately render the texture and features of the subject, while the blue backdrop and checkered pattern on the turntable and pot enhance feature extraction.

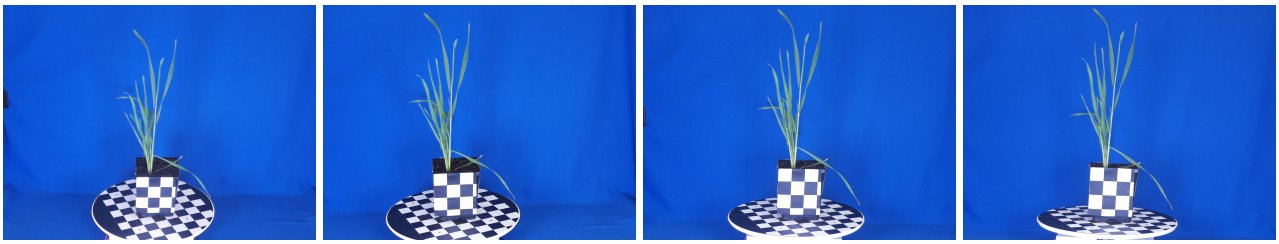

(a) Camera A (b) Camera B (c) Camera C (d) Camera D

Figure 4.5: An example of images captured from four distinct elevational perspectives by cameras A through D of the photogrammetry rig. Camera A represents the highest vantage point, with each subsequent camera (B to D) capturing from progressively lower perspectives, showcasing the vertical axis view of the plant.

Figure 4.6 shows a series of binary images corresponding to the same set initially shown in

Figure 4.5. These images, labeled from Camera A to Camera D, are processed into binary format, where the visual data is reduced to two distinct color values, typically black and white. In the context of these images, the black areas (with a pixel intensity value of 0 in grayscale) represent regions where no features will be extracted, effectively masking out irrelevant portions of the scene. This binary processing is essential in SfM for isolating the areas of interest and enhancing the efficiency of the feature extraction step. The distinction between the wheat plant and the background in these images exemplifies the effectiveness of this binary transformation in preparing data for subsequent photogrammetric analysis.

(a) Camera A (b) Camera B (c) Camera C (d) Camera D

Figure 4.6: An example of binary images taken by the photogrammetry system from all four cameras of different viewpoints of wheat where no features will be extracted in these regions, where the mask image is black (pixel intensity value 0 in grayscale).

Algorithm 2 processes images to create masks by first converting them from BGR to LAB color space, focusing on the a and b channels. Thresholding is applied to the b channel with a binary cutoff of 80, setting pixels ≥ 80 to 128 and the rest to 0, and to the a channel with an inverse threshold of 140, setting pixels < 140 to 127, while all others are set to 0. The combined channels form a composite mask with pixel values of 0, 127, 128, and 255, effectively differentiating between the background (0), features more prominent in the b channel (127), those in the a channel (128), and the essential features present in both channels (255). A cutoff of 128 simplifies this to a binary mask (0 for non-essential, 255 for crucial points). The algorithm then generates a filename for each mask, storing them in a designated folder. These mask images are placed in the mask image folders in the dataset. All image filenames must be identical, except for adding the .png extension, so that COLMAP can correctly match each image with its corresponding mask. We chose these threshold values to isolate the blue background in the images and highlight the plant,

pot, and turntable. By generating image masks, COLMAP can accurately differentiate the subject from its background, which is instrumental in the quality of the 3D models.

Algorithm 2 Image Masking for Background Removal

```
Function image_mask(image_dir, mask_folder):
    Input: image_dir, mask_folder
    Set current directory to image_dir.
    images ← Retrieve all .jpg files in directory.
    For each image in images:
        img ← Load image.
        lab ← Convert img from BGR to LAB color space.
        Extract 'a' and 'b' channels from lab.
        Apply binary threshold at 80 to 'b' channel, setting pixels
            ≥ 80 to 128, others to 0.
        Apply inverse binary threshold at 140 to 'a' channel, setting
            pixels < 140 to 127, others to 0.
        mask ← Combine a_mask and b_mask.
        Refine mask by setting values < 128 to 0, enhancing feature prominence.
        filename ← Generate mask filename.
        Save mask in mask_folder with generated filename.
```

4.3 3D reconstruction with COLMAP

The graphical interface of COLMAP allows users to visually inspect and interact with reconstructed models, whereas the command-line interface caters to advanced usage, offering scriptability for automated workflows and parameter variations. Users can input these arguments directly in the command line or through a file, where only the location of the file is used as an argument. Regarding data storage and processing, COLMAP uses an SQLite database to store image paths, features, feature matches, and camera information/parameters. The reconstruction process then utilizes this database to generate a 3D model, saving it in a specified output folder as three binary files: one each for cameras, images, and 3D points. These files can be subsequently accessed through the COLMAP GUI for viewing and analyzing the reconstruction. The 3D point cloud data are in PLY format (Polygon File Format), a data storage format that stores the information of the 3D structures.

We created a script that interfaces with COLMAP, as shown in Algorithm 3. This script automates the process of 3D reconstruction by sequentially executing various COLMAP commands, thus streamlining the workflow from image processing to the generation of 3D models. The initial feature extraction step uses the COLMAP feature extractor with set parameters to identify points in input images. This is followed by image matching, where the script utilizes the exhaustive matcher in COLMAP to find correspondences between the features across various images. The script executes the COLMAP mapper to construct a preliminary sparse 3D model based on the matched features from the earlier stages. Subsequently, the script moves to image undistortion and dense reconstruction preparation, where images undergo processing to correct distortions and align accurately, preparing them for the next step. The dense reconstruction step involves running the patch match stereo algorithm, a feature of COLMAP that refines the 3D model by densely matching points across the image collection. The procedure completes with stereo fusion, the final stage where the script integrates the depth maps into a 3D model, exporting it in PLY format.

Algorithm 3 COLMAP Interface Script

Input: WORK_SPACE, config
    Set feature extraction parameters from config
    Set matching parameters from config
    Set mapper parameters from config
    Set patch match stereo parameters from config
    Set stereo fusion parameters from config
Feature Extraction:
    Execute COLMAP feature extractor with parameters
Image Matching:
    Execute COLMAP exhaustive matcher
3D Mapping (Sparse Reconstruction):
    Execute COLMAP mapper for sparse 3D modeling
Image Undistortion and Dense Reconstruction Prep:
    Execute COLMAP image undistorter
Dense Reconstruction (Patch Match Stereo):
    Execute COLMAP patch match stereo
Stereo Fusion:
    Execute COLMAP stereo fusion to create 3D model
Output: 3D point cloud model in PLY format

Table 4.2 shows the hardware specifications of two distinct systems used for 3D reconstruction tasks in this work, utilizing the COLMAP interface script. It highlights key components such as CPUs, RAM, GPUs, GPU device memory, PCIe bus speeds, and compiler configurations. System 1, featuring an AMD 12-Core Processor and NVIDIA Geforce RTX 3090 GPU, contrasts with System 2, which is equipped with an Intel Xeon CPU and NVIDIA Tesla V100 GPU, making it more suited for data-intensive tasks due to its superior memory bandwidth and enhanced compute capability. The comparative analysis of reconstruction times reveals that System 1 completes the 3D reconstruction in approximately 120 minutes, while System 2 exhibits more efficient performance, accomplishing the task within 60-120 minutes. System 2, hosted on Digital Research Alliance of Canada (DRAC), served as the primary platform for the majority of the 3D reconstruction computation in this work.

	System 1	**System 2**
CPU	AMD 1920X 12-Core Processor @ 3.50 GHz	Intel Xeon(R) CPU @ 2.50GHz
RAM	32 GB	40 GB
GPU	NVIDIA Geforce RTX 3090 Compute capability 5.0 10496 CUDA cores Peak memory bandwidth 80 GB/s	NVIDIA Tesla V100 GPU Compute capability 6.0 5120 CUDA cores Peak memory bandwidth 549 GB/s
GPU device memory	24 GB	12 GB
PCIe bus	v3.0 x16 (8.0GT/s)	v3.0 x16 (8.0GT/s)
C++ compiler	Microsoft Visual Studio C++ 2015 compiler	GCC C++ compiler
CUDA compiler	nvcc	nvcc
Operating System	Windows 10	Ubuntu-22.04.3
Reconstruction Time	120 minutes	60-120 minutes

Table 4.2: Comparison of hardware specifications between system 1 and system 2, utilized for 3D reconstruction tasks in this work. The table outlines the differences in CPU, RAM, GPU, and other key hardware components, reflecting the distinct computational capabilities of each system. The full 3D reconstruction time took roughly 120 minutes for system 1 and 60-120 minutes for system 2

4.4 Preprocessing Point Cloud Data

A point cloud is defined as a set $\{ P_i \mid i = 1, \ldots, n\}$, where each point P_i represents a vector detailing its spatial location in (x, y, z) coordinates. The points within a point cloud are defined

by their spatial coordinates and carry additional information such as color, intensity, and normals. These correspond to RGB values, the light reflected to the sensor, and the orientation of the surface at each point. In our approach to process the point cloud data, we utilized the Open3D library, a toolset designed for the handling and analysis of 3D data [109]. Open3D offers many point cloud processing functionalities, including filtering, downsampling, and segmentation. In Open3D, when visualizing point clouds, meshes, or other 3D geometries, the three axes in 3D space represent the default coordinate system; each is colored red, green, and blue to indicate the X, Y, and Z axes respectively. Figure 4.7 shows a flowchart detailing the point cloud data pre-processing steps. The process includes centering the point cloud, segmenting the plane of the turntable to find the normal vector, rotating the point cloud to align with the z-axis, placing the base of the point cloud on the XY-plane, segmenting the outer ring points of the turntable to find the point cloud diameter, applying color thresholding to distinguish plant from non-plant elements, removing the pot, turntable, and any unnecessary points.

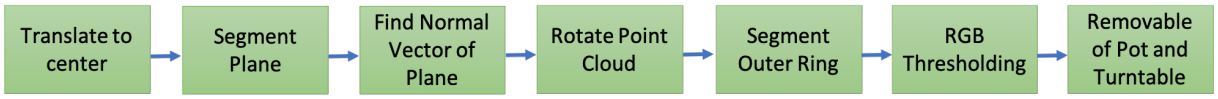

Figure 4.7: The point cloud is translated to center, followed by plane segmentation to identify the turntable points and find the normal vector. Subsequent steps involve rotating the point cloud to align with the positive z-axis and adjusting its position so that the bottom of the point cloud lies on the XY-plane. The next step is segmentation of the outer ring points of the turntable and a color thresholding step to exclude non-plant points, leading to the removal of the pot, turntable points, and any irrelevant points, such as those reflecting the blue backdrop. This is done to refine the dataset for further analysis.

Adjusting the points of a point cloud to center its orientation and ensure its base aligns with the positive XY plane is essential for preparing accurate and consistent 3D point cloud datasets. The process is done in three primary stages: centering the point cloud, adjusting its vertical position, and translating the points such that the plane of the bottom of the point cloud aligns with $Z = 0$. The first step, centering the point cloud, starts with the computation of the centroid, which is the average position of all points within the point cloud. This is accomplished by calculating the mean

of the X, Y, and Z points. The subsequent step involves translating every point in the cloud so that this centroid aligns with the origin of the coordinate system. This translation is done by subtracting the centroid to each point and reorienting the center of the point cloud to the origin.

Adjusting the vertical position of the 3D point cloud involves aligning the point such that its elevation extends along the Z-axis. The objective is to align the normal vector of the turntable with the positive Z-axis. This alignment is achieved with a rotational transformation applied to the points in the cloud, calculated to minimize the angular deviation between the normal vector of the plane and the Z-axis. Algorithm 4 uses a RANSAC-based approach to identify the most fitting plane within a point cloud by maximizing the number of inliers within a specified distance threshold. The process begins with the parameters: the point cloud, a distance threshold defining the inliers, and the maximum iterations to refine the search for the optimal plane. Three points are randomly selected from the point cloud to define a candidate plane.

Algorithm 4 Plane Segmentation in a Point Cloud

```
function SEGMENTPLANE(pointCloud, distanceThreshold, maxIterations)
    bestPlane ← null
    bestInliers ← empty set
    for i ← 1 to maxIterations do
        sampledPoints ← Randomly sample 3 points from pointCloud
        plane ← Fit a plane to sampledPoints
        inliers ← empty set
        for all point in pointCloud do
            if Distance from point to plane < distanceThreshold then
                Add point to inliers
            end if
        end for
        if Size of inliers > Size of bestInliers then
            bestPlane ← plane
            bestInliers ← inliers
        end if
    end for
    return bestPlane, bestInliers
end function
```

The evaluation of the plane includes calculating each distance of the points to the plane and identifying inliers within the distance threshold. The iteration yielding the largest set of inliers is

deemed to have found the best-fitting plane. Upon concluding the iterations, the algorithm returns the parameters of the identified plane alongside its inliers, signifying a successful segmentation of a significant planar surface from the point cloud. Given the plane equation $ax + by + cz + d = 0$, the normal vector $\vec{n}$ can be directly obtained as $\vec{n} = [a, b, c]$. As an example, Figure 4.8 shows the plane segmentation process applied to a point cloud of a wheat plant taken 35 days post-planting. As shown in Figure 4.8(b) the point cloud has been translated to the center, with the turntable highlighted in red to indicate that these points, representing a plane within the point cloud, have been successfully segmented. Additionally, the red arrow visually illustrates the direction of the normal vector relative to the segmented plane, showing the orientation of the turntable.

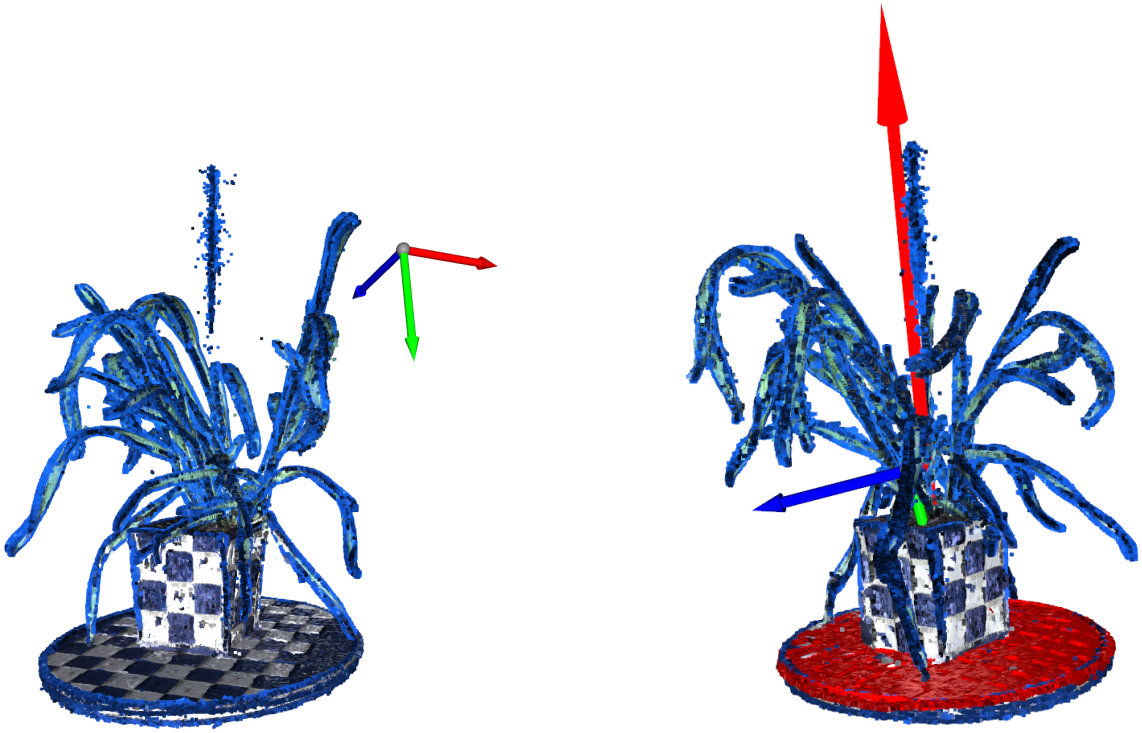

(a) Normal point cloud before segmentation.

(b) The point cloud after plane segmentation and translation to the origin of the coordinate system.

Figure 4.8: Visualization of the plane segmentation and repositioning of the point cloud to the center coordinate system. (a) Shows the unprocessed point cloud of a wheat plant 35 days post-planting. (b) Shows the point cloud after applying the plane segmentation, with the identified plane highlighted in red to indicate the segmented area. A red arrow indicates the direction of the normal vector of the plane, showing the orientation of the plane within the point cloud data.

The base of the point cloud is adjusted to sit on the positive XY plan by shifting upward by

the absolute value $|d|$ from the segmented plane equation. As shown in Figure 4.9, this adjustment ensures that the lowest point of the point cloud sits at $Z = 0$, aligning the base with the segmented plane. Also, the normal vector of the plane within the point cloud data was determined and used to rotate the point cloud. As detailed in Algorithm 5, the process begins by defining the Z-axis as the vector $[0,0,1]$ and calculate the rotation axis by taking the cross product of the normal vector with the positive Z-axis, resulting in a perpendicular vector to both. This rotation axis is then normalized to a unit vector to simplify calculations. The algorithm proceeds to determine the rotation angle required to align the normal vector with the Z-axis, which is achieved by calculating the $\arccos(\theta)$ of the dot product of the normal vector and the Z-axis. It then computes a rotation matrix using this angle and the normalized rotation axis. This matrix is crucial for transforming the points, as it rotates them by multiplying the points array with the transpose of the rotation matrix.

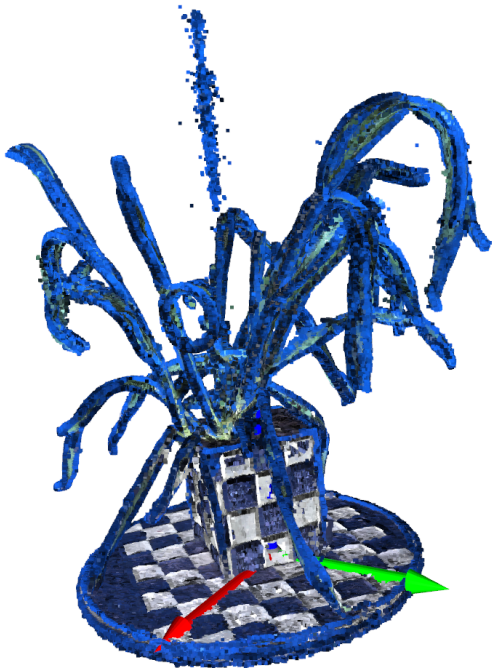

Figure 4.9: The process for orienting the point cloud data is to align the data with the positive Z-axis. The normal vector of the plane within the point cloud data was determined and used to rotate the point cloud. The point cloud is also shifted vertically by the absolute value $|d|$ of the plane equation such that the lowest point of the 3D model sits at Z=0.

The scale of the point cloud is established by dividing the real diameter of the turntable by the

Algorithm 5 Align points with Z-axis

Require: $points$: an array of points to rotate
Require: $normal\_vector$: the vector to align with the Z-axis
Ensure: $rotated\_points$: an array of rotated points

$z\_axis \leftarrow [0,0,1]$
$rotation\_axis \leftarrow cross(normal\_vector, z\_axis)$
$rotation\_axis \leftarrow normalize(rotation\_axis)$
$angle \leftarrow arccos(dot(normal\_vector, z\_axis))$
$rotation\_matrix \leftarrow R.from\_rotvec(angle \times rotation\_axis).as\_matrix()$
$rotated\_points \leftarrow dot(points, rotation\_matrix^T)$
return $rotated\_points$

diameter derived from the segmented outer points of the turntable in the point cloud data. Figure 4.10 shows the segmented outer ring of the turntable, where the segmented points are highlighted in red as shown in Figure 4.10(a). Figure 4.10(b) shows the point cloud alongside the segmented ring, showcasing the method used for ensuring the scale accuracy of the point cloud. Scaling is essential for measurements and analyses of point cloud data, ensuring they reflect true real-world dimensions.

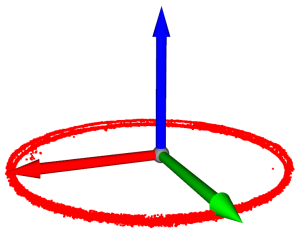

(a) Segmentation of the outer ring from the turntable.

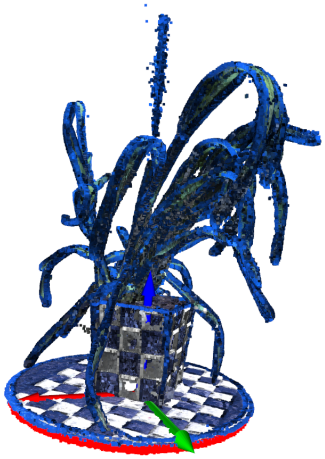

(b) The complete point cloud view post-segmentation, showing the position of the point cloud and segmented turntable ring highlighted in red.

Figure 4.10: Segmentation of the outer ring from the turntable, effectively highlighting the boundary that surrounds the base of the turntable where the plants are placed. This step is done to accurately determine the diameter of the turntable, ensuring the 3D model is precisely calibrated and scaled.

Segmenting the ring of the turntable within the point cloud, as outlined in Algorithm 6, involves calculating the radial distance of each point from the center of the point cloud, thereby determining the spatial distribution of points based on their proximity to the origin. The process begins by filtering the points within a specified Z-value range to isolate the turntable section. Subsequently, it calculates the radial distance of each filtered point relative to the center of the point cloud, facilitating an analysis of point distribution based on proximity to this central point. By constructing a histogram of these radial distances and organizing them into a specified number of bins, the algorithm identifies the most common radial distance indicative of the area where the turntable ring is most densely populated. This method, rooted in radial distance calculation and histogram analysis, allows for the accurate segmentation of the outer ring of the turntable.

Algorithm 6 Segment Ring Points

function SEGMENT_RING_POINTS(pts, num_bins, z_min, z_max, tolerance)
    filtered_pts ← pts[(pts[:, 2] > z_min) & (pts[:, 2] < z_max)]
    r ← sqrt(filtered_pts[:, 0]^2 + filtered_pts[:, 1]^2)
    hist, bin_edges ← histogram(r, bins=num_bins)
    max_bin_index ← argmax(hist)
    peak_radius ← (bin_edges[max_bin_index] + bin_edges[max_bin_index + 1]) / 2
    ring_indices ← where((r $\geq$ peak_radius - tolerance) & (r $\leq$ peak_radius + tolerance))
    return ring_indices
end function

While the blue Poly Pro matte fabric provides a uniform backdrop as shown in Figure 3.15, it also introduces an undesirable blue hue to the edges of objects in the 3D reconstructed model. An essential step in the post-processing stage is the application of RGB color thresholding, designed to eliminate these unwanted blue hues. By establishing specific thresholds within the RGB color space, it becomes possible to identify and remove pixels that match the color range of the blue background, thereby significantly improving the color of the final 3D model. Algorithm 7 selects and filters points based on these RGB color thresholds. This is done by creating new arrays: one for the spatial locations of the filtered-out points, referred to as filtered_points, and another for their corresponding color values, named filtered_colors. These arrays are populated with the data of points that did not satisfy the color criteria, effectively separating them from the rest of the

point cloud. This separation is vital for applications that require point clouds with specific color characteristics, as it allows for the exclusion of irrelevant or undesired data based on color. Figure 4.11 shows the RGB thresholding on a 3D point cloud. The unfiltered point cloud with visible blue hues along the edges of the object as shown in Figure 4.11(a). Figure 4.11(b) shows applying the RGB thresholding removing any blue hues from the point cloud data. .

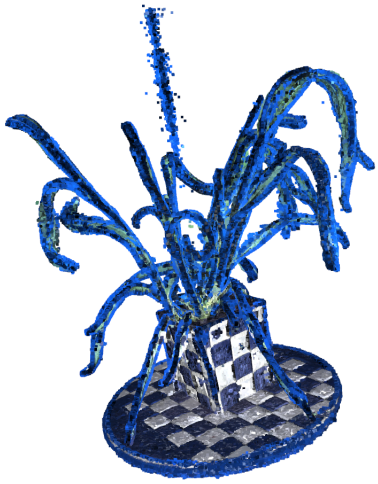

(a) Unprocessed point cloud showing the original state of the 3D model with visible blue hues along the edges of the object.

(b) Processed point cloud after applying RGB thresholding.

Figure 4.11: Techniques for RGB thresholding enhance the color fidelity of the 3D reconstructed models. (a) The 3D point cloud is shown before applying RGB thresholding, where the blue hue from the backdrop is visible along the edges the object. (b) Illustrates the model after processing, highlighting and removing the blue hues, and improving the overall color accuracy of the model. This process involves identifying and removing pixels within specific color thresholds and refining the point cloud data to exclude irrelevant or undesired color data.

Algorithm 7 Filter RGB Points

1: **function** FILTERNONPOINTS(*points*, *colors*, *lower_threshold*, *upper_threshold*)
2: $outside\_threshold\_indices \leftarrow \text{ALL}((colors < lower\_threshold) \text{ OR } (colors > upper\_threshold), axis = 1)$
3: $filtered_points \leftarrow points[outside_threshold_indices]$
4: $filtered_colors \leftarrow colors[outside_threshold_indices]$
5: **return** $(filtered_points, filtered_colors)$
6: **end function**

The final process involves using Meshlab to refine the point cloud data by manually removing the pot and turntable sections in the software and isolating the plant as the primary focus. Figure 4.12 shows a cleaned point cloud, illustrating the cleaning and alignment results, highlighting the enhanced structure and uniformity of the point clouds. The refined output is a detailed representation of the plant, achieved through a series of steps: reorienting the dataset to align the normal vector of the turntable to the positive Z-axis and position the points to be parallel to the XY plane, scaling the point cloud using the diameter of the turntable as a reference; employing color-based denoising to retain green and brown points; and filtering out all extraneous non-plant points.

Figure 4.12: A cleaned point cloud following refinement using Meshlab, highlighting the elimination of the pot and turntable to focus solely on the plant. The process encompasses reorienting to align the point cloud with the Z-axis, scaling based on the diameter of the turntable, color-based denoising to emphasize plant-relevant parts, and the removal of all non-plant elements.

In this chapter, we've outlined a comprehensive pipeline for operating the photogrammetry rig, from controlling the rig to capturing and processing images for 3D reconstruction. By incorporating COLMAP and implementing preprocessing algorithms to 3D point clouds, our method refines 3D plant data, establishing a framework for 3D plant phenotyping. These steps ensure the transformation of point clouds into a dataset that accurately depicts the plant and makes it suited for further analysis. In the next chapter, results from the wheat phenotyping analysis will be discussed, focusing on the evaluation and classification of wheat genotypes through height-to-radius

ratio measurements and canopy volume calculations. This work automates the characterization of wheat morphology, facilitating faster and more efficient plant breeding processes.

5. Wheat Phenotyping with the Photogrammetry Rig

This chapter presents an analysis of wheat canopy architecture through the classification and differentiation of planophile and erectophile traits. Section 5.1 explains the experiment of classification and differentiation of wheat based on the canopy architecture, identifying planophile and erectophile traits. In Section 5.2, we explain the methodologies for image acquisition and dataset creation with the photogrammetry rig, detailing the procedures used to develop the 3D point cloud datasets. Section 5.3 will discuss the results to assess and categorize the wheat cultivars based on the height-to-radius ratio measurements and canopy volume calculations, associating these phenotypic traits with specific genotypes.

5.1 Distinguishing Planophile and Erectophile Traits in Wheat

Focus towards optimizing canopy architecture to enhance light capture, particularly during the critical growth phases between stem elongation and flowering will likely lead to larger gains in grain yield [47]. Furthermore, the impact of genetic variations in leaf angle on grain yield has revealed that wheat with erect canopies outperforms planophile variants by achieving a 13% increase in grain yield, attributed to an 11% rise in biomass. Wheat exhibiting an upright leaf angle during vegetative growth phases exhibits significantly higher photosynthetic capacity, contributing to improved biomass accumulation [110]. This show that wheat varieties with an erect canopy architecture can potentially achieve superior grain yields compared to planophile types, highlighting the important role of leaf angle and canopy structure in enhancing agricultural productivity.

Given that the traits of erectophile and planophile canopies are genetically determined, early identification of these characteristics can substantially enhance a breeders' ability to select for erectophile types efficiently, utilizing larger populations and requiring less greenhouse space. Current selection methodologies, which rely on subjective rating scales ranging from 1 to 10, are inadequate for the precise and quantitative differentiation between erectophile and planophile types in extensive field trials. Adopting more objective and quantitative assessment methods is imperative for accurately identifying these traits. Understanding the fundamental mechanisms governing erectophile and planophile morphologies will empower breeders to incorporate critical genetic regulators into their breeding lines more effectively.

This study outlines the development of a quantitative trait index that leverages the ratio of plant height to its maximum radius as a potential metric for distinguishing between planophile and erectophile wheat phenotypes. Image data of wheat were imaged using the photogrammetry rig, and 3D datasets of each wheat genotype were generated. The metric was used to evaluate and compare the different wheat genotypes by identifying planophile or erectophile characteristics. Furthermore, the analysis also includes an assessment of canopy volume for these genotypes, utilizing the 3D data to calculate the convex hull.

5.2 Methodology Overview

5.2.1 Data Preparation

In this study, we cultivated ten plants, each containing five seedlings from six distinct wheat genotypes, all under controlled environmental conditions to guarantee uniform growth. The growth chamber accommodated all 60 pots, with a watering schedule set for every second day to maintain adequate moisture levels for seedling development. The plants were grown under controlled environmental conditions lighting, temperature, and watering schedules were uniform to ensure minimal variability in growth. They were housed in the Conviron growth chamber at the Univer-

sity of Winnipeg, with temperatures set at 25 °C during the day and 18 °C at night, and relative humidity kept at 60%, providing an ideal growth environment. Figure 5.1 captures the initial growth stages of the wheat plants from day 1 to day 7 within the growth chamber.

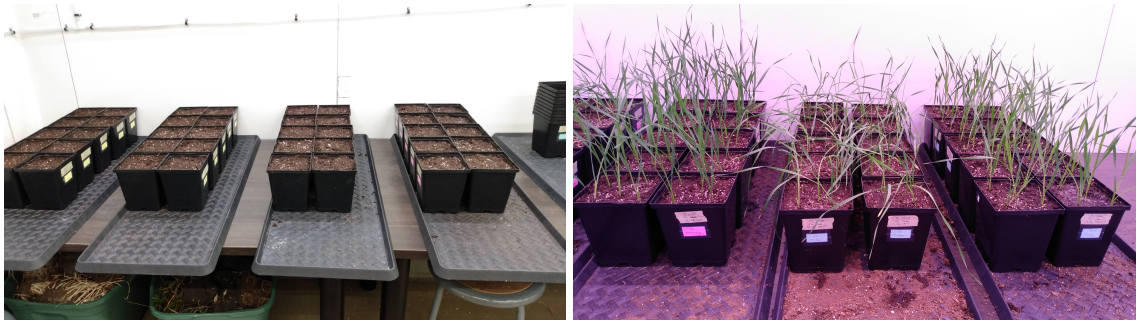

(a) Day 1 of wheat plants for the experiment (b) Day 7 of wheat plants for the experiment

Figure 5.1: The early growth stages of wheat plants involved in the experiment. (a) The initial stage of the seedlings on day 1, illustrating their condition at the beginning of the experiment. (b) Shows the development of these seedlings by day 7, highlighting the noticeable changes and growth patterns that have occurred.

Table 5.1 shows the planting and imaging schedule of the six wheat genotypes, indicating when each pot was planted and imaged. The imaging process was staggered throughout the week, initiating with the imaging of the Chara and Gladius genotype on Tuesday, proceeding with Brandon and Kukri on Wednesday, and concluding with Teal and Alsen on Friday. For this study, we focus exclusively on the data from days 14 and 35 to analyze critical growth phases for the canopy volume and the height-to-radius (H/R) ratio measurements. The naming convention for the dataset follows the format of WheatGenotype_PotNumber_CaptureDate, where 'PotNumber' consists of a letter indicating the wheat genotype followed by a numerical digit, denoting the specific pot.

Genotype	**Pot Number**	**Planting Date**	**Day 14 Image Capture**	**Day 35 Image Capture**
Chara	A0-A9	2023/06/13	2023/06/20	2023/07/18
Gladius	B0-B9	2023/06/13	2023/06/20	2023/07/18
Brandon	C0-C9	2023/06/14	2023/06/21	2023/07/19
Kukri	D0-D9	2023/06/14	2023/06/21	2023/07/19
Teal	E0-E9	2023/06/16	2023/06/23	2023/07/21
Alsen	F0-F9	2023/06/16	2023/06/23	2023/07/21

Table 5.1: This table chronologically outlines the planting and imaging schedule for this study.

5.2.2 Data Acquisition

The photogrammetry rig, equipped with an Arducam 64MP Autofocus Quad-Camera kit, was used to photograph the wheat plants. Plants were taken out of the growth chamber and imaged for an estimated 25 minutes, and returned to the chamber. The setup facilitated automatic image acquisition from each camera, automating movement of the rotary table after every four sets of images were captured. The autofocus on the camera kit eliminates the need for any manual focus adjustments on the cameras. Image sessions were scheduled for days 14 and 35 post-planting. After the day 14 imaging session, plants were selectively thinned, leaving only the most robust specimen in each pot for measurements on day 35. Table 5.2 outlines the configuration of the photogrammetry rig used in this experiment, highlighting the crucial settings for optimal image capture of the plants. The turntable was set to rotate at 10° to guarantee substantial overlap among the 148 total images captured, facilitating thorough data collection. The resolution of the cameras was set at 4084 x 3051, with specific settings including a 16 mm focal length, an aperture of f/5.6, and an ISO level of 143. To capture the entirety of each plant while maintaining a consistent background, the distance between the plant and the rig was kept within 1-2 meters. Completing a full 360-degree imaging of each plant required a total of 25 minutes.

Setting	**Value**
Turntable Angle	10°
Total Images	148
Camera Resolution	4084 x 3051
Focal Length	16 mm
Aperture Setting	f/5.6
ISO Setting	ISO-143
Distance to Subject	1-2 m
Total Imaging Time	25 Minutes
Total Size on Disk	297 MB
Pause Before Image Capture	6 seconds

Table 5.2: Imaging parameters used for the photogrammetry rig for capturing wheat images, including turntable angle, total number of images, camera resolution, focal length, aperture setting, ISO setting, distance to subject, total imaging time, total size on disk, and image capture delay.

For this study, 120 3D point clouds were reconstructed and refined, with image data offloaded to a remote server on DRAC for processing, requiring an estimated 60-120 minutes per pot for completion. Point clouds were generated using the COLMAP interface script as outline in the last chapter. Figure 5.2 illustrates the growth stages of the Alsen wheat genotype at days 14 and 35 post-planting, showing both images and point cloud data. Figure 5.2(a) shows an image of the Alsen genotype on day 14 and Figure 5.2(b) shows an image of the Alsen genotype on day 35. Additionally, Figures 5.2(c) and 5.2(d) show the generated point clouds of the Alsen genotype on days 14 and 35 day, respectively. Each point cloud dataset underwent a pre-processing stage as detailed in the previous chapter. Point clouds were scaled (using the diameter of the turntable), denoised based on color (removing all but the green/brown points), aligned to the positive z-axis, and translated to the origin such that the ground of the point cloud is parallel to the X–Y plane. The scale for each point cloud was calculated by dividing the diameter observed in the point cloud by the actual diameter of the turntable. Any manually adjustments and removable of noise were done using Meshlab such as the pot and turntable.

(a) Image of the Alsen genotype on day 14.

(b) Image of the Alsen genotype on day 35.

(c) Point cloud of the Alsen genotype on day 14.

(d) Point cloud of the Alsen genotype on day 35.

Figure 5.2: Illustration of the Alsen genotype at days 14 and 35 post-planting, depicted through 2D images and point cloud visualizations. These representations underscore the significant growth phases and structural transformations observed, offering a comprehensive view of the developmental dynamics in this study. Note that images are not to scale.

5.3 Results and Discussion

5.3.1 Canopy Volume

Day 14 Wheat Dataset

The convex hull method was used to determine the canopy volume, providing a quantitative assessment of the spatial configuration and structural intricacy of each wheat genotype by encasing the canopy of the plant within the smallest possible convex shape. In erectophile plants, the upright orientation of leaves and stems leads to a compact, streamlined canopy at the top. Figure 5.3 shows the Gladius cultivar on day 14 with an erectophile leaf orientation in the dataset. Specifically, Figure 5.3(a) shows the reconstructed point cloud data, centralized on the XY plane and elevated to the height of the pot, with both the pot and turntable removed. Figure 5.3(b) shows the application of the convex hull algorithm on the point cloud assessing the canopy volume.

(a) Visual of Gladius pot B6.

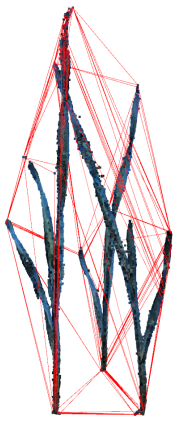

(b) Convex hull method applied to Gladius pot B6.

Figure 5.3: Visualization of the 3D point clouds of the Gladius genotype, imaged on day 14 post-planting. (a) Shows the erectophile leaf orientation of the Gladius genotype, showing the structural arrangement of the plant. (b) The application of the convex hull method to assess the canopy volume where the plant is envelope in the smallest possible convex shape.

For planophile plants the volume is larger because the horizontal orientation of leaves and

stems would spread out more, occupying more space. Figure 5.4 shows the Brandon genotype and its planophile leaf orientation. Figure 5.4(a) shows the fully reconstructed point cloud data, centralized on the XY plane and elevated to the height of the pot, with the pot and turntable points removed. Figure 5.4(b) illustrates the application of the convex hull algorithm to assess the canopy volume, highlighting its accuracy in detailing the structural composition of the plant.

(a) Visual of Brandon pot C4.

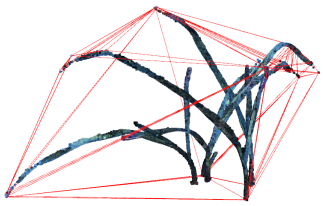

(b) Convex hull method applied to Brandon pot C4.

Figure 5.4: Visualization of the 3D point clouds for the Brandon genotype, captured on day 14 post-planting. (a) Shows the planophile leaf orientation of the Brandon genotype, giving a view of the plant's structural arrangement. (b) Demonstrates the effective application of the convex hull method to determine the canopy volume where the plant is envelope in the smallest possible convex shape.

In this study, we also determined the canopy volume of the top 60% by excluding the bottom 40% of points along the Z-axis. This approach, aimed at isolating and examining the upper portion of the canopy, allows for a targeted analysis of the most light-exposed regions of the plant. In erectophile plants, the canopy segment is often less voluminous due to the vertical orientation of leaves and stems, which limits the horizontal spread of the canopy. On the other hand, the upper 60% of planophile plants is likely to exhibit greater volume because of the leaves and stem horizontal arrangement. As an example, Figure 5.5 shows the Kukri and Alsen wheat genotypes at 60% canopy height, illustrating their erectophile and planophile leaf orientations, respectively. Figure 5.5(a) illustrates the Kukri genotype and Figure 5.5(b) shows the convex hull method to determine the canopy at volume 60% canopy. Additionally, Figure 5.5(c) illustrates the canopy height at 60% for the Alsen genotype and Figure 5.5(d) shows the canopy volume.

The canopy volume was calculated for all plants showing the structural variations within the six

(a) Canopy at 60% of Kukri pot D7.

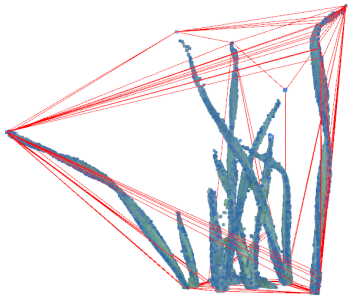

(b) Convex hull method applied to Kukri pot D7.

(c) Canopy at 60% of Alsen pot F4.

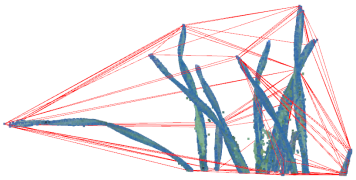

(d) Convex hull method applied to Alsen pot F4.

Figure 5.5: The canopy volume at 60% height for both the Kukri and Alsen wheat genotypes, highlighting the distinct leaf orientations. The convex hull method is applied to quantify the canopy volume of each genotype. In erectophile plants, the upper 60% of the canopy tends to be more compact due to the vertical arrangement of leaves and stems. Conversely, the corresponding segment of a planophile plant's canopy is generally more expansive, attributed to the horizontal orientation of its leaves and stems.

wheat genotypes as illustrated in Figure 5.6. For each wheat genotype, the average was calculated across 10 pots and visually graded on a scale from 1 to 10, where 1 indicates a more erectophile trait and 10 indicates a more planophile trait. Using this grading system, the wheat genotypes were plotted from left to right, ranging from erectophile to planophile. This visual grading system for the wheat genotypes was conducted by Kalhari Manawasinghe at the University of Saskatchewan. As show in Figure 5.6(a), the data suggests that Teal and to a lesser extent Brandon and Alsen exhibit more planophile traits, indicated by their larger and more variable canopy volumes. On the other hand, Chara, Kukri, and Gladius tend to exhibit more erectophile traits, as seen in their generally lower and less variable canopy volumes. Figure 5.6(b) shows the canopy volume of the genotypes at 60% of the height, the data show that Brandon, Teal, and Alsen possess more pronounced planophile characteristics in their upper canopy structures, likely benefiting from a

growth pattern that emphasizes broad leaf and branch distribution to enhance light capture. In contrast, Chara, Kukri, and Gladius seem to adhere more closely to erectophile traits, with their canopy volumes at 60% height reflecting a growth orientation that prioritizes vertical development over horizontal spread.

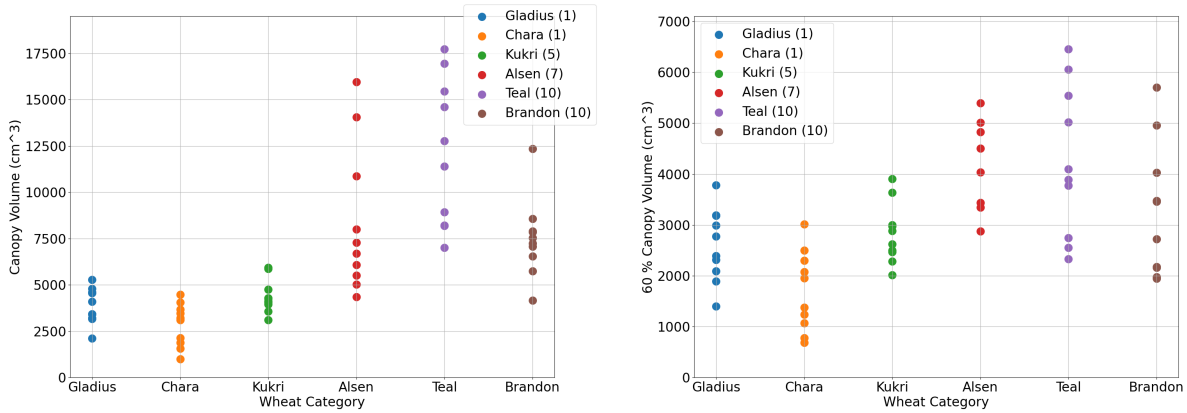

(a) Results of day 14 canopy volume.

(b) Results of day 14 canopy volume at 60 % height.

Figure 5.6: Visuals of canopy volumes on day 14, utilizing the convex hull method on 3D point cloud data, demonstrating the structural diversity among the different wheat genotypes. Each data point is a measurement taken from the reconstructed 3D point clouds for each of the wheat genotypes. The analysis highlights the canopy volume variations at full height and at the 60% of the height. Each wheat genotype, averaged over 10 pots, was visually scored from 1 (more erectophile) to 10 (more planophile).

Day 35 Wheat Dataset

Following a selective thinning process after day 14 to retain only the most robust plant in each pot, canopy volume measurements were performed on the day 35 point cloud data. Figure 5.7 shows an example of the Gladius cultivar on day 35 with an erectophile leaf orientation in the dataset. Figure 5.7(a) shows the point cloud data, aligned with the XY plane at a height matching the position of the pot within the coordinate system, with unwanted points removed such as the pot and turntable. Figure 5.7(b) shows the application of the convex hull algorithm on the point cloud determining the canopy volume. The day 35 dataset showed a significant increase in plant size, reflected quantitatively by the enlarged canopy volume.

(a) Visual of Gladius pot B6.

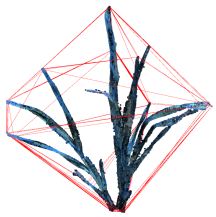

(b) Convex hull method applied to Gladius pot B6.

Figure 5.7: Visualization of the 3D point clouds of the Gladius genotype, captured on day 35 post-planting. (a) Displays the erectophile leaf orientation of the Gladius genotype, illustrating the plant's structural configuration. (b) Demonstrates the use of the convex hull method for canopy volume assessment, enveloping the plant in the minimal convex shape.

Emphasizing more planophile leaf orientation, Figure 5.8 features the Brandon genotype as an example. Furthermore, Figure 5.8(a) shows the point cloud data, aligned with the XY plane at the elevation of the pot, with all the pot and turntable points removed. Figure 5.8(b) highlights the application of the convex hull algorithm to evaluate canopy volume, effectively illustrating its accuracy in mapping the architectural structure of the plant.

(a) Visual of Brandon pot C9.

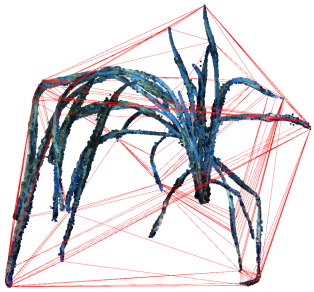

(b) Convex hull method applied to Brandon pot C9.

Figure 5.8: Visualization of the 3D point clouds for the Brandon genotype, captured on day 35 post-planting. (a) Shows the planophile leaf orientation of the Brandon genotype, giving a view of the plant's structural arrangement. (b) Showing the effective application of the convex hull method to assess the canopy volume.

Figure 5.9 shows the Kukri and Alsen wheat genotypes at 60% canopy height, illustrating their erectophile and planophile leaf orientations, respectively. Figure 5.9(a) illustrates the Kukri genotype and Figure 5.9(b) shows the convex hull method to determine the canopy at volume 60% canopy. Conversely, planophile plants such as the Alsen genotype exhibit a wider lateral spread,

maximizing the surface area exposed, as shown in Figures 5.9(c) and 5.9(d), highlighting a growth strategy to optimize light absorption across a broader canopy.

(a) Canopy at 60% of Kukri pot D7.

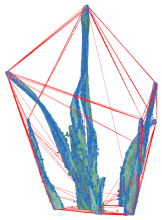

(b) Convex hull method applied to Kukri pot D7.

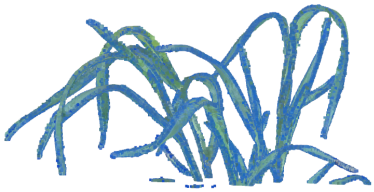

(c) Canopy at 60% of Alsen pot F4.

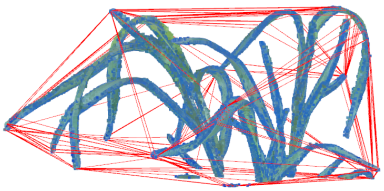

(d) Convex hull method applied to Alsen pot F4.

Figure 5.9: The canopy volume at 60% height for both the Kukri and Alsen wheat genotypes highlights distinct leaf orientations. By employing the convex hull method, the canopy volume for each genotype is accurately quantified. In erectophile plants, the canopy upper 60% exhibits a denser structure, a result of the leaves and vertical alignment of the stems. On the other hand, canopy volume at 60% height of the planophile appears broader, a characteristic stemming from the horizontal spread of the leaves and stem.

Calculations of canopy volume among six wheat genotypes demonstrate structural differences, illustrated in Figures 5.10 and 5.10(a). For day 35, data points were arranged and plotted accordingly, with each wheat genotype visually scored on a scale from 1 to 10. Brandon and Teal exhibit the most significant variation in canopy volumes, indicative of a planophile orientation characterized by a wider leaf distribution. Alsen presents considerable volumes with reduced variability, hinting at a planophile characteristics. Conversely, Chara, Kukri, and Gladius exhibit smaller canopy volumes, with Gladius particularly compact, suggesting erectophile characteristics due to a more vertical leaf arrangement. At 60% height, as shown in Figure 5.10(b), the variability of canopy volume in Brandon and Teal is notable, with Teal achieving some of the largest volumes in the dataset, reflecting a pronounced planophile orientation. Alsen displays a broad range, including high volumes, indicative of a substantial horizontal leaf spread in the upper canopy. Meanwhile,

Chara, Kukri, and Gladius present lower volumes, consistent with an erectophile orientation.

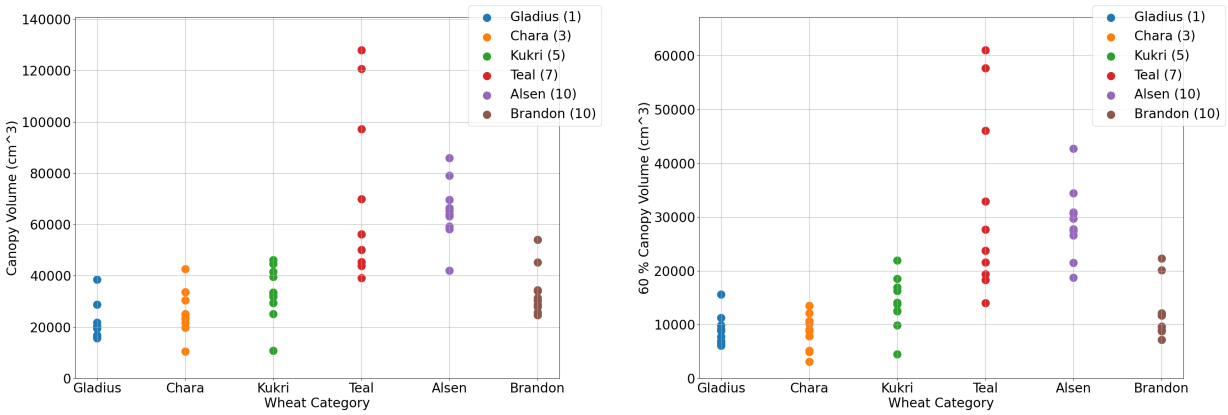

(a) Results of day 35 of canopy volume.

(b) Results of day 35 of canopy volume at 60 % height.

Figure 5.10: Visuals of canopy volumes on day 35, utilizing the convex hull method on 3D point cloud data to demonstrating the structural diversity among the different wheat genotypes. The analysis highlights the canopy volume variations at full height and at the 60% of the height. Manual grading of erectophile and planophile is also shown.

5.3.2 Height and Maximum Radius Ratio

Day 14 Wheat Dataset

The H/R ratio measures the vertical growth of a plant against its horizontal spread, determined by converting point cloud datasets to cylindrical coordinates to find the maximum radius. This process isolates a horizontal slice of the whole point cloud to identify the maximum radius, which is the distance from the center of the point cloud to the max R value. A higher H/R ratio indicates an erectophile, characterizing genotypes prioritizing vertical growth and exhibiting a taller stature relative to the horizontal spread. For example, Figure 5.11(a) illustrates the height of the Gladius genotype on day 14, where the height of the Gladius is quantified by the difference between its maximum and minimum Z-axis values. Additionally, a polar plot, derived from cylindrical coordinates, is shown in Figure 5.11(b) to determine the maximum radius.

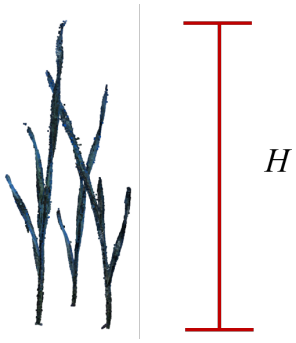

(a) Visual of height of Gladius pot B6.

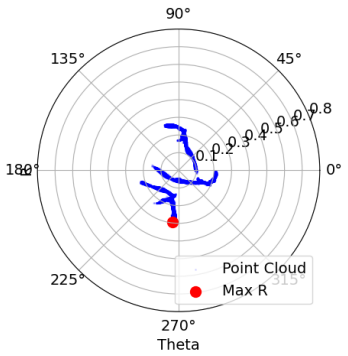

(b) Polar plot of Gladius pot B6.

Figure 5.11: Plots of the Gladius wheat genotype on day 14, emphasizing its structural traits through direct visualization and polar coordinate representation. (a) Captures the vertical height of the Gladius genotype, illustrating its height characteristic. (b) Shows the polar plot of the Gladius wheat, offering a visual of its canopy spread.

A lower H/R ratio suggests a planophile orientation, indicative of genotypes exhibiting a more expansive lateral spread relative to their height. Figure 5.15 shows the Brandon genotype, the smaller height value combined with a larger radius is indicative of its planophile characteristics. This trait is visually represented in Figure 5.12(a) where the 3D visualization emphasizes the relatively lower vertical growth, while the polar plot in Figure 5.12(b) show the lateral spread of the canopy, as evidenced by the larger radius.

(a) Visual of height of Brandon pot C4.

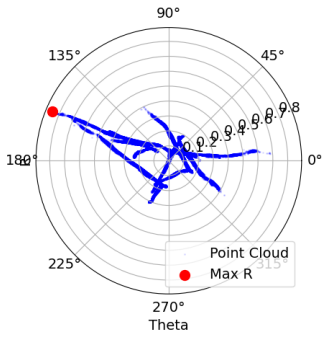

(b) Polar plot of Brandon wheat pot C4.

Figure 5.12: Visual of the Brandon wheat genotype at day 14 post-planting, offering insights into its planophile growth orientation through both 3D and polar plots. (a) Illustrates the plant height of Brandon, a factor in computing the H/R ratio. (b) The polar plot provides a graphical depiction of the canopy spread of Brandon.

Figure 5.13 shows the H/R ratio analysis for six wheat genotypes at day 14, revealing their

growth orientations. The visual grading system among the wheat genotypes reveals a trend where distinguishing features are evident, indicating variations in growth patterns. The ratio variation underscores the balance between vertical growth and horizontal spread, with distinct peaks for certain genotypes hinting at their adaptability and specific growth patterns. The H/R ratio values of Brandon and Teal suggest planophile traits, with Brandon maintaining a near 1 ratio and Teal showing significant variability. Alsen and Kukri, with H/R ratios over 1.5 indicates erectophile traits, though to a slightly lesser extent. Gladius and Chara, with the highest ratios, display pronounced erectophile growth, emphasizing vertical over horizontal development. The 14-day dataset contains 4-5 seedlings per pot, which may lead to inaccuracies in H/R values due to calculations encompassing the entire point cloud rather than individual plants. However, it is important to consider that while the H/R ratio provides useful insights, it still offers a somewhat simplified view of plant architecture.

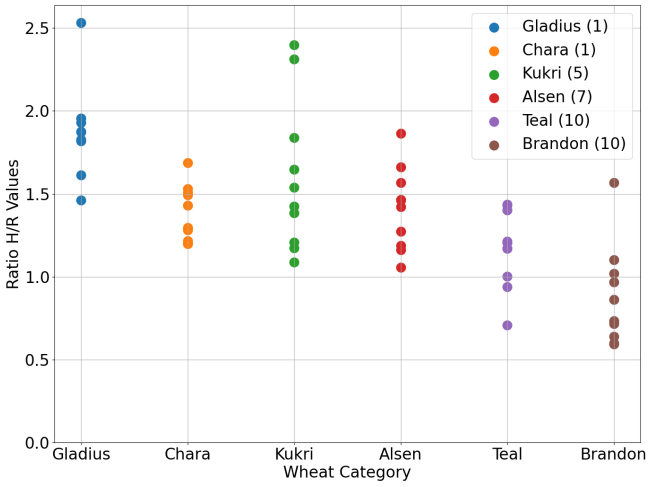

Figure 5.13: The H/R ratio variation among the six wheat genotypes on day 14. The visual grading system highlights a trend in wheat genotypes, showing clear variations from erectophile to planophile traits. Brandon and Teal show a moderate range of H/R ratios, suggesting they both have planophile traits, with Teal displaying notable peaks that indicate flexibility and instances of erectophile orientation. Alsen and Kukri exhibit higher H/R ratios, strongly suggesting an erectophile growth. Gladius and Chara demonstrate more erectophile traits based on the highest H/R ratios.

Day 35 Wheat Dataset

For the day 35 dataset, as an example, Figure 5.14(a) shows the visualizations of the Gladius wheat genotype. The 3D plot illustrates the vertical growth of the plant by calculating its height through the range of Z-axis values. Additionally, Figure 5.14(b) shows a polar plot that maps the radial distance R against the angle θ as well, and notably marks the position of the maximum R value. This plot further emphasizes the erectophile characteristics of the plant by offering a different perspective on its structural form, focusing on the vertical rather than horizontal expansion. At day 35 post-planting, these visualizations illustrate the significant growth of the wheat plants and specifically the Gladius genotype and its characteristic erectile orientation, marked by a strong emphasis on upward rather than expanding outward.

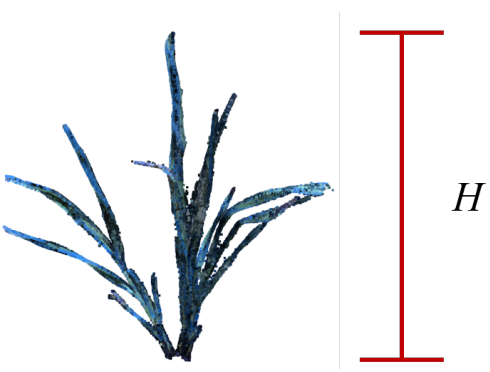

(a) Visual of height of Gladius pot B6.

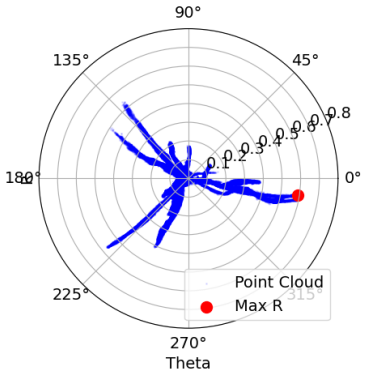

(b) Polar plot of Gladius pot B6.

Figure 5.14: Plots of the Gladius wheat genotype on day 35, emphasizing its structural traits through direct visualization and polar coordinate representation. (a) Captures the vertical height of the Gladius genotype, which is used to determine the H/R ratio. (b) Shows the polar plot of the Gladius wheat, marking the position of the maximum R value.

In another example, Figure 5.15 depicts the Brandon genotype point cloud from the dataset, illustrating the growth pattern and highlighting the planophile characteristics through a distinctly shorter height and wider radius. Furthermore, the 3D visualization in Figure 5.15(a) shows the limited vertical development of the plant, a defining feature of planophile orientation, and illustrates how this growth strategy optimizes horizontal space. The polar plot in Figure 5.15(b) illustrates the lateral expansion of the canopy, as indicated by the extended radius.

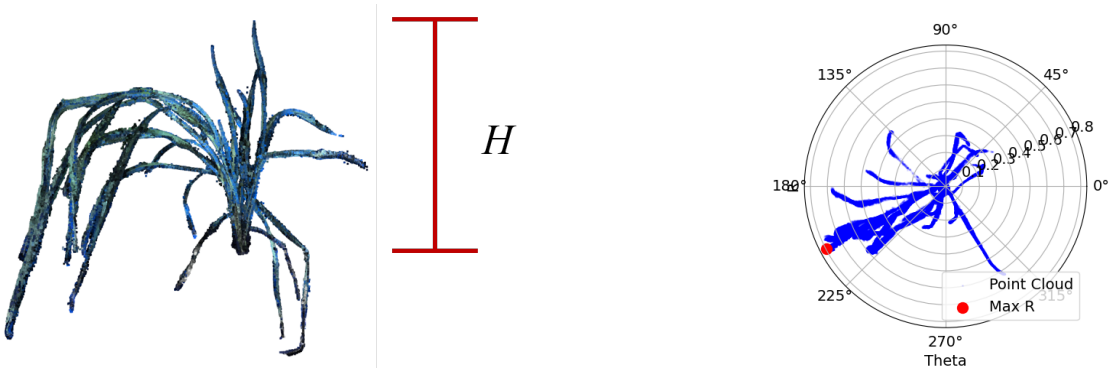

(a) Visual of height of Brandon pot C9.

(b) Polar plot of Brandon wheat pot C9.

Figure 5.15: Visual of the Brandon wheat genotype at day 35 post-planting, offering insights into its planophile growth orientation through both 3D and polar plots. (a) Illustrates the plant height of Brandon, a factor in computing the H/R ratio, which indicates the growth pattern of the plant. (b) The polar plot shows a graphical depiction of the canopy spread of the Brandon genotype.

Figure 5.16 analyzes the H/R ratios among the six wheat genotypes at day 35. Manual grading for these genotypes is performed alongside H/R ratio analysis, providing a more nuanced understanding of the architectural tendencies of each genotype. Brandon exhibits a relatively moderate range of H/R ratios, mostly hovering around 1 where as Alsen shows a trend towards higher H/R ratios. This suggests a balance between height and spread. For Teal, the H/R ratios display variability, interspersed with values closer to 1. This is underscored by values exceeding 1.5, suggesting a growth pattern that favors height overspread. With H/R ratios frequently surpassing 1.5, Chara demonstrates a clear erectophile growth pattern. Gladius and Kukri presents some of the highest H/R ratios among the genotypes, strongly indicating an erectophile growth. This differentiation in growth patterns underscores the genetic diversity within wheat cultivars and its potential implications for optimizing crop yields and resource efficiency.

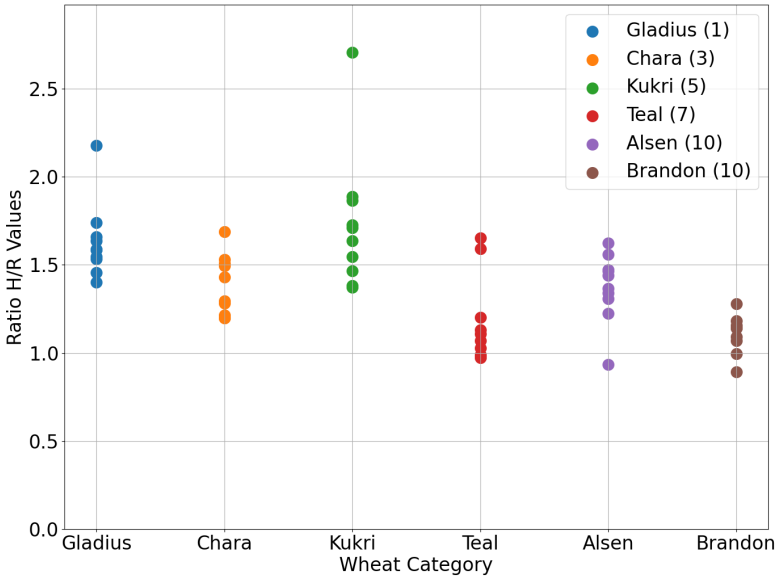

Figure 5.16: The H/R ratio variation among the six wheat genotypes on day 35 reflects their erectophile or planophile growth. Manual grading complements the H/R ratio analysis, showing the growth tendencies of each genotype. Brandon and Alsen show a moderate range of H/R ratios, suggesting they both have planophile traits, with Teal displaying notable peaks that indicate flexibility and instances of erectophile orientation. Chara exhibit higher H/R ratios, strongly suggesting an erectophile growth. Gladius and Kukri demonstrate more erectophile traits based on the highest H/R ratios.

6. Conclusion

6.1 Summary

In this thesis, we developed an all-in-one, low-cost photogrammetry rig to advance 3D plant phenotyping by incorporating novel techniques and methodologies to analysis plant development. Conventional phenotyping methods, characterized by invasive sampling, labor-intensive measurements, and inconsistent results, pose significant limitations to large-scale genetic studies by hindering the understanding of plant genotype-environment interactions. Moreover, 2D imaging techniques fall short in capturing the 3D complexity of plant morphology, often resulting in partial or misleading data. Utilizing low-cost photogrammetry for 3D plant phenotyping enables researchers to efficiently gather comprehensive data on plant growth, structure, and interactions with environmental variables. Our imaging system, engineered for simplicity and high functionality, equips researchers, plant scientists, and breeders with a robust and accessible means to perform 3D plant scanning and phenotyping. Such advancements are expected to lead to more efficient and effective plant breeding and crop management methods.

We detail the complete pipeline, covering the hardware setup, the software processing specifics, and the capabilities of the system. We demonstrated the utility of the photogrammetry rig through initial testing by validating 3D reconstruction measurements of soybean height. The analysis revealed a strong correlation, evidenced by an R^2 value of 0.99 and an RMSE of 0.81 and a MAPE of 10.63% further quantify the precision and average percentage error, respectively, indicating a highly accurate representation of plant growth. Additionally, we evaluated canopy volume measurements of lettuce and soybean using the convex hull method, observing exponential growth over five weeks.

Building on our initial experiments, we further applied the photogrammetry rig to focus on wheat phenotyping, explicitly aiming to develop a quantitative method to distinguish between planophile and erectophile traits across various wheat genotypes. In addition to developing a quantitative trait index leveraging the ratio of plant height to its maximum radius, canopy volume assessment was used to achieve to differentiate between planophile and erectophile traits. This targeted analysis enables a more nuanced understanding of wheat growth patterns and structural characteristics, providing valuable insights for agricultural research and breeding strategies. In our assessment, we identified that Brandon and Teal exhibit planophile characteristics, while Alsen and Chara, display erectophile traits, albeit to a slightly lesser degree. Gladius and Kukri, on the other hand, demonstrated the most pronounced erectophile characteristics among the genotypes evaluated. Through these assessments, the photogrammetry rig emerges not just as a tool, but as a vital resource for innovative research, providing a versatile instrument for researchers.

6.2 Future Work

Future research will investigate additional plant traits, automate and develop more robust methods to identify planophile and erectophile characteristics, develop algorithms for denoising and segmenting plant organs. We aim to conduct further experiments to explore quicker 3D reconstruction techniques and validate the accuracy of point cloud data measurements. Moreover, there is a need to upgrade the hardware components of the rig and refine the image acquisition processes to achieve faster and more efficient 3D reconstructions. Efforts will be made to foster a more autonomous pipeline, reducing the need for user intervention. These improvements will reduce the time required for data collection and increase the precision and accuracy of the 3D models generated. Also, there is a need to enhance and refine the GUI of the system, focusing on improving user interaction through the introduction of more intuitive controls and a wider range of options, enabling users to efficiently configure and customize their imaging sessions according to specific research needs. Integrating motors into the system to automate rotational and positional

adjustments of the cameras will eliminate the necessity for manual camera repositioning during imaging sessions. Finally, constructing an expanded backdrop will facilitate imaging larger plant specimens.

In conclusion, this thesis presents a new tool for agricultural research and practice, laying the groundwork for future innovations in 3D plant phenotyping. By lowering the barriers to entry for accessing sophisticated 3D modeling tools, this work empowers researchers, agronomists, plant scientists, and breeders to conduct more detailed, accurate, and efficient analyses of plant phenotypes, ultimately fostering informed decision-making and advancements in crop science and agriculture.

References

[1] C. Godfray, J. Beddington, I. Crute, L. Haddad, D. Lawrence, J. Muir, J. Pretty, S. Robinson, and C. Toulmin. Food security: The challenge of feeding 9 billion people. *Science (New York, N.Y.)*, 327:812–8, 02 2010.

[2] N. Alexandratos and J. Bruinsma. *World Agriculture Towards 2030/2050: The 2012 Revision*. 10 2012.

[3] B. Miflin. Crop improvement in the 21st century. *Journal of Experimental Botany*, 51(342):1–8, 01 2000.

[4] J. Bailey-Serres, J. Parker, E. Ainsworth, G. Oldroyd, and J. Schroeder. Genetic strategies for improving crop yields. *Nature*, 575:109–118, 11 2019.

[5] V. Kakani, V. H. Nguyen, B. P. Kumar, H. Kim, and V. R. Pasupuleti. A critical review on computer vision and artificial intelligence in food industry. *Journal of Agriculture and Food Research*, 2:100033, 2020.

[6] A. Walter, F. Liebisch, and A. Hund. Plant phenotyping: From bean weighing to image analysis. *Plant Methods*, 11:14, 03 2015.

[7] W. Salter, A. Shrestha, and M. Barbour. Open source 3d phenotyping of chickpea plant architecture across plant development. *Plant Methods*, 17, 09 2021.

[8] L. Li, Q. Zhang, and D. Huang. A review of imaging techniques for plant phenotyping. *Sensors*, 14(11):20078–20111, 2014.

[9] F. Fiorani and U. Schurr. Future scenarios for plant phenotyping. *Annual Review of Plant Biology*, 64(1):267–291, 2013. PMID: 23451789.

[10] D. Houle, D. Govindaraju, and S. Omholt. Phenomics: The next challenge. *Nature reviews. Genetics*, 11:855–66, 12 2010.

[11] A. Singh, B. Ganapathysubramanian, A. K. Singh, and S. Sarkar. Machine learning for high-throughput stress phenotyping in plants. *Trends in plant science*, 21(2):110—124, February 2016.

[12] N. Fahlgren, M. Feldman, M. A. Gehan, M. S. Wilson, C. Shyu, D. W. Bryant, S. T. Hill, C. J. McEntee, S. N. Warnasooriya, I. Kumar, and et al. A versatile phenotyping system and analytics platform reveals diverse temporal responses to water availability in setaria. *Molecular Plant*, 8(10):1520–1535, 2015.

[13] A. Razzaq, P. Kaur, N. Akhter, S. H. Wani, and F. Saleem. Next-generation breeding strategies for climate-ready crops. *Frontiers in Plant Science*, 12, 2021.

[14] F. Fiorani and U. Schurr. Future scenarios for plant phenotyping. *Annual review of plant biology*, 64:267–91, 2013.

[15] A. Atefi, Y. Ge, S. Pitla, and J. Schnable. Robotic technologies for high-throughput plant phenotyping: Contemporary reviews and future perspectives. *Frontiers in Plant Science*, 12.

[16] R. T. Furbank and M. Tester. Phenomics – technologies to relieve the phenotyping bottleneck. *Trends in Plant Science*, 16(12):635–644, 2011.

[17] J. Cobb, G. Declerck, A. Greenberg, R. Clark, and S. Mccouch. Next-generation phenotyping: Requirements and strategies for enhancing our understanding of genotype-phenotype relationships and its relevance to crop improvement. *TAG. Theoretical and applied genetics. Theoretische und angewandte Genetik*, 03 2013.

[18] M. Minervini, A. Fischbach, H. Scharr, and S. Tsaftaris. Finely-grained annotated datasets for image-based plant phenotyping. *Pattern Recognition Letters*, 81, 11 2015.

[19] J. De Vylder, F. Vandenbussche, Y. Hu, W. Philips, and D. Van Der Straeten. Rosette tracker: An open source image analysis tool for automatic quantification of genotype effects. *Plant Physiology*, 160(3):1149–1159, 08 2012.

[20] E. P. Spalding and N. D. Miller. Image analysis is driving a renaissance in growth measurement. *Current Opinion in Plant Biology*, 16(1):100–104, 2013.

[21] S. Paulus, J. Dupuis, A.-K. Mahlein, and H. Kuhlmann. Surface feature based classification of plant organs from 3d laserscanned point clouds for plant phenotyping. *BMC Bioinformatics*, 14:238, 2014.

[22] J.R. Rosell and R. Sanz. A review of methods and applications of the geometric characterization of tree crops in agricultural activities. *Computers and Electronics in Agriculture*, 81:124–141, 2012.

[23] B. Biskup, H. Scharr, U. Schurr, and U. Rascher. A stereo imaging system for measuring structural parameters of plant canopies. *Plant, Cell & Environment*, 30(10):1299–1308, 2007.

[24] R. Al-Tameemi, S. Hamandi, and A. Al-Mahdi. Creating a digital 3d model of the dental cast using structure-from-motion photogrammetry technique. *International Journal of Online and Biomedical Engineering (iJOE)*, 19:4–17, 03 2023.

[25] W. Johannsen. The genotype conception of heredity1. *International Journal of Epidemiology*, 43(4):989–1000, 03 2014.

[26] F. Breseghello and A. Siqueira G. Coelho. Traditional and modern plant breeding methods with examples in rice (oryza sativa l.). *Journal of Agricultural and Food Chemistry*, 61(35):8277–8286, 2013. PMID: 23551250.

[27] R. Meyer and M. Purugganan. Evolution of crop species: Genetics of domestication and diversification. *Nature reviews. Genetics*, 14:840–52, 12 2013.

[28] P. L. Pingali. Green revolution: impacts, limits, and the path ahead. *Proceedings of the National Academy of Sciences*, 109(31):12302–12308, 2012.

[29] N. Shakoor, S. Lee, and T. C. Mockler. High throughput phenotyping to accelerate crop breeding and monitoring of diseases in the field. *Current Opinion in Plant Biology*, 38:184–192, 2017. 38 Biotic interactions 2017.

[30] K. H. von Mogel. Taking the phenomics revolution into the field. *CSA News*, 58(3):4–10, 2013.

[31] J. W. White, P. Andrade-Sanchez, M. A. Gore, K. F. Bronson, T. A. Coffelt, M. M. Conley, K. A. Feldmann, A. N. French, J. T. Heun, D. J. Hunsaker, and et al. Field-based phenomics for plant genetics research. *Field Crops Research*, 133:101–112, 2012.

[32] N. Fahlgren, M. A. Gehan, and I. Baxter. Lights, camera, action: high-throughput plant phenotyping is ready for a close-up. *Current Opinion in Plant Biology*, 24:93–99, 2015.

[33] A. L. Casto, H. Schuhl, J. C. Tovar, Q. Wang, R. S. Bart, N. Fahlgren, and M. A. Gehan. Picturing the future of food. *The Plant Phenome Journal*, 4(1):e20014, 2021.

[34] E. Aklilu. Review on forward and reverse genetics in plant breeding. *All Life*, 14(1):127–135, 2021.

[35] S. Atwell, Y.S. Huang, B.J. Vilhjalmsson, G. Willems, M. Horton, Y. Li, D. Meng, A. Platt, A.M. Tarone, T.T. Hu, and et al. Genome-wide association study of 107 phenotypes in arabidopsis thaliana inbred lines. *Nature*, 465(7298):627–631, 2010.

[36] P. M. P. Correia, J. C. Westergaard, A. Bernardes da Silva, T. Roitsch, E. Carmo-Silva, and J. Marques da Silva. High-throughput phenotyping of physiological traits for wheat resilience to high temperature and drought stress. *Journal of Experimental Botany*, 73(15):5235–5251, 04 2022.

[37] A. Hairmansis, B. Berger, M. Tester, et al. Image-based phenotyping for non-destructive screening of different salinity tolerance traits in rice. *Rice*, 7(1):16, 2014.

[38] F. Tardieu, L. Cabrera-Bosquet, T. Pridmore, and M. Bennett. Plant phenomics, from sensors to knowledge. *Current Biology*, 27(15):R770–R783, 2017.

[39] M. M. Hasan, J. P. Chopin, H. Laga, et al. Detection and analysis of wheat spikes using convolutional neural networks. *Plant Methods*, 14:100, 2018.

[40] M. C. Westhues, G. S. Mahone, S. da Silva, R. Meyer, O. K. Oyebamiji, F. M. Pogoda, J. C. Schnable, M. C. Romay, and K. Guan. Prediction of maize phenotypic traits with genomic and environmental predictors using gradient boosting frameworks. *Frontiers in Plant Science*, 12(699589), 2021.

[41] M. Yoosefzadeh-Najafabadi, H. J. Earl, D. Tulpan, J. Sulik, and M. Eskandari. Application of machine learning algorithms in plant breeding: Predicting yield from hyperspectral reflectance in soybean. *Frontiers in Plant Science*, 11, 2021.

[42] Y. Kim, R. G. Evans, and W. M. Iversen. Remote sensing and control of an irrigation system using a distributed wireless sensor network. *IEEE Transactions on Instrumentation and Measurement*, 57(7):1379–1387, 2008.

[43] Y. Zhao, A. B Potgieter, M. Zhang, B. Wu, and G. L. Hammer. Predicting wheat yield at the field scale by combining high-resolution sentinel-2 satellite imagery and crop modelling. *Remote Sensing*, 12(6), 2020.

[44] A. Wasson, R. Richards, R. Chatrath, S. Misra, S. Sakuru, G. Rebetzke, J. Kirkegaard, J. Christopher, and M. Watt. Traits and selection strategies to improve root systems and water uptake in water-limited wheat crops. *Journal of experimental botany*, 63:3485–98, 05 2012.

[45] J. L. Araus and J. E. Cairns. Field high-throughput phenotyping: the new crop breeding frontier. *Trends in Plant Science*, 19(1):52–61, 2014.

[46] X. Wang, D. Singh, S. Marla, G. Morris, and J. Poland. Field-based high-throughput phenotyping of plant height in sorghum using different sensing technologies. *Plant Methods*, 14(53), 2018.

[47] R. A. Richards, C. R. Cavanagh, and P. Riffkin. Selection for erect canopy architecture can increase yield and biomass of spring wheat. *Field Crops Research*, 244:107649, 2019.

[48] M.R. Golzarian, R.A. Frick, K. Rajendran, et al. Accurate inference of shoot biomass from high-throughput images of cereal plants. *Plant Methods*, 7(2), 2011.

[49] M. I. Menzel, S. Tittmann, J. Bühler, S. Preis, N. Wolters, S. Jahnke, A. Walter, A. Chlubek, A. Leon, N. Hermes, and et al. Non-invasive determination of plant biomass with microwave resonators. *Plant, Cell & Environment*, 32(4):368–379, 2009.

[50] S. Arvidsson, P. Pérez-Rodríguez, and B. Mueller-Roeber. A growth phenotyping pipeline for arabidopsis thaliana integrating image analysis and rosette area modeling for robust quantification of genotype effects. *New Phytologist*, 191(3):895–907, 2011.

[51] M. Jansen, F. Gilmer, B. Biskup, K. Nagel, A. Fischbach, S. Briem, G. Dreissen, S. Tittmann, S. Braun, I. Jaeger, and et al. Simultaneous phenotyping of leaf growth and chlorophyll fluorescence via growscreenfluoro allows detection of stress tolerance in. *Functional Plant Biology*, 36:902–914, 11 2009.

[52] L. Duan, W. Yang, C. Huang, et al. A novel machine-vision-based facility for the automatic evaluation of yield-related traits in rice. *Plant Methods*, 7:44, 2011.

[53] S. Balachandran, V. M. Hurry, S. E. Kelley, C. B. Osmond, S. A. Robinson, J. Rohozinski, G. G. R. Seaton, and D. A. Sims. Concepts of plant biotic stress. some insights into the stress physiology of virus-infected plants, from the perspective of photosynthesis. *Physiologia Plantarum*, 100(2):203–213, 1997.

[54] J. A. Gibbs, M. P. Pound, A. P. French, D. M. Wells, E. H. Murchie, and T. Pridmore. Approaches to three-dimensional reconstruction of plant shoot topology and geometry. *Functional Plant Biology*, 44(1):62–75, 2016.

[55] S. Paulus. Measuring crops in 3d: using geometry for plant phenotyping. *Plant Methods*, 15:103, 2019.

[56] A. King. Technology: The Future of Agriculture. *Nature*, 544(7651):21–23, April 2017.

[57] A. Kumar, R. K. Pathak, S. M. Gupta, V. S. Gaur, and D. Pandey. Systems biology for smart crops and agricultural innovation: Filling the gaps between genotype and phenotype for complex traits linked with robust agricultural productivity and sustainability. *OMICS: A Journal of Integrative Biology*, 19(10):581–601, 2015. PMID: 26484978.

[58] K. E. Keightley and G. W. Bawden. 3d volumetric modeling of grapevine biomass using tripod lidar. *Computers and Electronics in Agriculture*, 74(2):305–312, 2010.

[59] S. Paulus, J. Dupuis, A.K. Mahlein, et al. Surface feature based classification of plant organs from 3d laserscanned point clouds for plant phenotyping. *BMC Bioinformatics*, 14:238, 2013.

[60] K. Nagasubramanian, S. Jones, A.K. Singh, et al. Plant disease identification using explainable 3d deep learning on hyperspectral images. *Plant Methods*, 15:98, 2019.

[61] S. Paulus, J. Dupuis, S. Riedel, and H. Kuhlmann. Automated analysis of barley organs using 3d laser scanning: An approach for high throughput phenotyping. *Sensors*, 14(7):12670–12686, 2014.

[62] R. Khanna, L. Schmid, A. Walter, and J. Nieto. A spatio temporal spectral framework for plant stress phenotyping. *Plant Methods*, 15(1):13, 2019.

[63] F. Hosoi and K. Omasa. Estimating vertical plant area density profile and growth parameters of a wheat canopy at different growth stages using three-dimensional portable lidar imaging. *ISPRS Journal of Photogrammetry and Remote Sensing*, 64(2):151–158, 2009.

[64] R. Gebbers, D. Ehlert, and R. Adamek. Rapid mapping of the leaf area index in agricultural crops. *Agronomy Journal*, 103:1532–1541, 09 2011.

[65] T. Nguyen, D. Slaughter, N. Max, J. Maloof, and N. Sinha. Structured light-based 3d reconstruction system for plants. *Sensors (Basel, Switzerland)*, 15:18587–612, 08 2015.

[66] S. Paulus, H. Schumann, H. Kuhlmann, and J. Léon. High-precision laser scanning system for capturing 3d plant architecture and analysing growth of cereal plants. *Biosystems Engineering*, 121:1–11, 05 2014.

[67] X. Lu, E. Ono, S. lu, Y. Zhang, P. Teng, M. Aono, Y. Shimizu, F. Hosoi, and K. Omasa. Reconstruction method and optimum range of camera-shooting angle for 3d plant modeling using a multi-camera photography system. *Plant Methods*, 16, 08 2020.

[68] A. Paproki, X. Sirault, S. Berry, et al. A novel mesh processing based technique for 3d plant analysis. *BMC Plant Biology*, 12(63), 2012.

[69] T. Moeckel, S. Dayananda, R. R. Nidamanuri, S. Nautiyal, N. Hanumaiah, A. Buerkert, and M. Wachendorf. Estimation of vegetable crop parameter by multi-temporal uav-borne images. *Remote Sensing*, 10(5), 2018.

[70] Y. Shi, J. A. Thomasson, S. C. Murray, N. A. Pugh, W. L. Rooney, S. Shafian, N. Rajan, G. Rouze, C. L. S. Morgan, H. L. Neely, and et al. Unmanned aerial vehicles for high-throughput phenotyping and agronomic research. *PLOS ONE*, 11(7):1–26, 07 2016.

[71] J. He, R. Harrison, and B. Li. A novel 3d imaging system for strawberry phenotyping. *Plant Methods*, 13, 11 2017.

[72] G. van der Heijden, Y. Song, G. Horgan, G. Polder, J. Dieleman, M. Brink, A. Palloix, F. Eeuwijk, and C. Glasbey. Spicy: towards automated phenotyping of large pepper plants in the greenhouse (online first). *Functional Plant Biology*, 39, 11 2012.

[73] B. Biskup, H. Scharr, U. Schurr, and U. Rascher. A stereo imaging system for measuring structural parameters of plant canopies. *Plant, Cell & Environment*, 30(10):1299–1308, 2007.

[74] A. Shafiekhani, S. Kadam, F. B. Fritschi, and G. N. DeSouza. Vinobot and vinoculer: Two robotic platforms for high-throughput field phenotyping. *Sensors*, 17(1), 2017.

[75] A. Milella, R. Marani, A. Petitti, and G. Reina. In-field high throughput grapevine phenotyping with a consumer-grade depth camera. *Computers and Electronics in Agriculture*, 156:293–306, 2019.

[76] R. C. Bolles, H. H. Baker, and D. H. Marimont. Epipolar-plane image analysis: An approach to determining structure from motion. *International Journal of Computer Vision*, 1:7–55, 1987.

[77] S. Ullman. The interpretation of structure from motion. *Proceedings of the Royal Society of London. Series B, Biological Sciences*, 203:405–426, 1979.

[78] M. N. Helfrick, C. Niezrecki, P. Avitabile, and T. Schmidt. 3d digital image correlation methods for full-field vibration measurement. *Mechanical Systems and Signal Processing*, 25(3):917–927, 2011.

[79] J. Iglhaut, C. Cabo, S. Puliti, L. Piermattei, J. O'Connor, and J. Rosette. Structure from motion photogrammetry in forestry: a review. *Current Forestry Reports*, 5, 09 2019.

[80] F. Plum and D. Labonte. scant —an open-source platform for the creation of 3d models of arthropods (and other small objects). *PeerJ*, 9:e11155, 04 2021.

[81] J. J. Medina, J. M. Maley, S. Sannapareddy, N. N. Medina, C. M. Gilman, and J. E. McCormack. A rapid and cost-effective pipeline for digitization of museum specimens with 3d photogrammetry. *PLoS ONE*, 15(8):e0236417, 2020.

[82] C. Nicolae, E. Nocerino, F. Menna, and F. Remondino. Photogrammetry applied to problematic artefacts. volume XL-5, 06 2014.

[83] E. M. Farella, L. Morelli, S. Rigon, E. Grilli, and F. Remondino. Analysing key steps of the photogrammetric pipeline for museum artefacts 3d digitisation. *Sustainability*, 14(9), 2022.

[84] M. Fau, R. Cornette, and A. Houssaye. Photogrammetry for 3d digitizing bones of mounted skeletons: Potential and limits. *Comptes Rendus Palevol*, 15(8):968–977, 2016.

[85] F. I. Apollonio, F. Fantini, S. Garagnani, and M. Gaiani. A photogrammetry-based workflow for the accurate 3d construction and visualization of museums assets. *Remote Sensing*, 13(3), 2021.

[86] M. Lo Brutto and P. Meli. Computer vision tools for 3d modeling in archaeology. *International Journal of Heritage in the Digital Era*, 1:1–6, 01 2012.

[87] J. D. Reu, P. De Smedt, D. Herremans, M. Van Meirvenne, P. Laloo, and W. De Clercq. On introducing an image-based 3d reconstruction method in archaeological excavation practice. *Journal of Archaeological Science*, 41:251–262, 2014.

[88] M. Doneus, G. Verhoeven, M. Fera, C. Briese, M. Kucera, and W. Neubauer. From deposit to point cloud – a study of low-cost computer vision approaches for the straightforward documentation of archaeological excavations. *Geoinformatics*, 6 (XXIIIrd International CIPA Symposium):81–88, 12 2011.

[89] B. Ducke, D. Score, and J. Reeves. Multiview 3d reconstruction of the archaeological site at weymouth from image series. *Computers Graphics*, 35(2):375–382, 2011. Virtual Reality in Brazil Visual Computing in Biology and Medicine Semantic 3D media and content Cultural Heritage.

[90] T. Liu, A. W. Burner, T. W. Jones, and D. A. Barrows. Photogrammetric techniques for aerospace applications. *Progress in Aerospace Sciences*, 54:1–58, 2012.

[91] X. Su and Q. Zhang. Dynamic 3-d shape measurement method: A review. *Optics and Lasers in Engineering*, 48(2):191–204, 2010. Fringe Projection Techniques.

[92] R. Jiang, D. V. Jáuregui, and K. R. White. Close-range photogrammetry applications in bridge measurement: Literature review. *Measurement*, 41(8):823–834, 2008.

[93] R. Hartley and A. Zisserman. *Multiple View Geometry in Computer Vision*. Cambridge University Press, 2 edition, 2004.

[94] J. L. Schönberger and J. Frahm. Structure-from-motion revisited. In *Conference on Computer Vision and Pattern Recognition (CVPR)*, 2016.

[95] D. G. Lowe. Distinctive image features from scale-invariant keypoints. *International Journal of Computer Vision*, 60:91–110, 2004.

[96] M. A. Fischler and R. C. Bolles. Random sample consensus: a paradigm for model fitting with applications to image analysis and automated cartography. *Commun. ACM*, 24(6):381–395, jun 1981.

[97] S. Bianco, G. Ciocca, and D. Marelli. Evaluating the performance of structure from motion pipelines. *Journal of Imaging*, 4(8), 2018.

[98] B. Triggs, P. F. McLauchlan, R. I. Hartley, and A. W. Fitzgibbon. Bundle adjustment - a modern synthesis. In *Workshop on Vision Algorithms*, 1999.

[99] O. Ozyesil, V. Voroninski, R. Basri, and A. Singer. A survey of structure from motion, 2017.

[100] Raspberry Pi Foundation. Raspberry pi 4 model b 4gb. `https://www.raspberrypi.org/products/raspberry-pi-4-model-b/`, 2023. Accessed: 2023-02-26.

[101] Arducam. Multi camera adapter module v2.2. `https://www.arducam.com/product/multi-camera-v2-1-adapter-raspberry-pi/`, 2023. Accessed: 2024-03-01.

[102] Arducam Technology Co., Limited. Getting Started with 64MP-AF Quad Camera Kit. 2022. [Online; accessed 21-March-2023].

[103] Ortery Technologies, Inc. Photocapture 360m - motorized turntable. `https://www.ortery.com/photocapture-360-product-photography-turntables/`, 2023. Accessed: 2023-02-26.

[104] Adafruit Industries. Dc and stepper motor hat for raspberry pi. `https://www.adafruit.com/product/2348`, 2023. Accessed: 2024-02-24.

[105] P. Cignoni, M. Callieri, M. Corsini, M. Dellepiane, F. Ganovelli, and G. Ranzuglia. MeshLab: an Open-Source Mesh Processing Tool. 2008.

[106] P. Virtanen, R. Gommers, T. E. Oliphant, M. Haberland, T. Reddy, D. Cournapeau, E. Burovski, P. Peterson, W. Weckesser, J. Bright, and et al. SciPy 1.0: Fundamental Algorithms for Scientific Computing in Python. *Nature Methods*, 17:261–272, 2020.

[107] C. B. Barber, D. P. Dobkin, and H. Huhdanpaa. The quickhull algorithm for convex hulls. *ACM Trans. Math. Softw.*, 22(4):469–483, dec 1996.

[108] D. Avis, D. Bremner, and R. Seidel. How good are convex hull algorithms? *Computational Geometry*, 7(5):265–301, 1997. 11th ACM Symposium on Computational Geometry.

[109] Q. Zhou, J. Park, and V. Koltun. Open3d: A modern library for 3d data processing. *arXiv:1801.09847*, 2018.

[110] M. A. J. Parry, M. Reynolds, M. E. Salvucci, C. Raines, P. J. Andralojc, X. Zhu, G. D. Price, A. G. Condon, and R. T. Furbank. Raising yield potential of wheat. II. Increasing photosynthetic capacity and efficiency. *Journal of Experimental Botany*, 62(2):453–467, 10 2010.